

The 2003 Outburst of the X-ray Nova H1743–322: Comparisons with the Black Hole Binary XTE J1550–564¹

Jeffrey E. McClintock², Ronald A. Remillard³, Michael P. Rupen⁴, M. A. P. Torres²,
D. Steeghs², Alan M. Levine³, Jerome A. Orosz⁵

ABSTRACT

We provide a comprehensive report on the X-ray and radio evolution of H1743–322 during its 2003 outburst. Our X-ray spectral and timing results (3–200 keV) are derived from 170 *RXTE* observations that span the complete 8-month outburst cycle. Our 6-frequency VLA light curves provide quite complete coverage of the entire outburst cycle at 4.860 GHz and 8.460 GHz. We also present photometric data and finding charts for the optical/NIR counterpart in both outburst and quiescence. The X-ray behavior of H1743–322 is shown to be remarkably similar to that of XTE J1550–564. We feature the striking behavior of the intermediate state that lies between the hard and the steep power-law states. This intermediate state shows a strong and linear correlation between the QPO frequency and the flux in the accretion-disk component. Furthermore, this state corresponds to maximal values of QPO amplitude and intensity of the Fe K line. As reported elsewhere, H1743–322 is the fourth black hole candidate to exhibit a pair of high-frequency QPO oscillations (240 Hz and 165 Hz) with a 3:2 frequency ratio. This fact and the evidence presented herein argue strongly that H1743–322 is a black hole binary, although presently no dynamical data exist to support this conclusion.

Subject headings: X-ray: stars — binaries: close — accretion, accretion disks — black hole physics — stars: individual (H1743–322, XTE J1550–564)

¹This paper includes data gathered with the 6.5 meter Magellan Telescopes located at Las Campanas Observatory, Chile.

²Harvard-Smithsonian Center for Astrophysics, 60 Garden Street, Cambridge, MA 02138

³MIT Kavli Center for Astrophysics and Space Research, Massachusetts Institute of Technology, Cambridge, MA 02139

⁴National Radio Astronomy Observatory, New Mexico Array Operations Center (VLA, VLBA), Socorro, NM 87801

⁵Department of Astronomy, San Diego State University, 5500 Campanile Drive, San Diego, CA 82182

1. Introduction

The X-ray nova H1743–322 displayed major outbursts in 1977 and in 2003. The 2003 outburst was followed by successively weaker outbursts in 2004 July and 2005 August. The source was initially discovered with the *Ariel* *Vall-sky* monitor by Kaluzienski & Holt (1977), who provided a $\sim 1^\circ$ position. Further definitive X-ray studies were carried out using the instruments aboard *HEAO-1*. The modulation collimator pinpointed the source location to one of two equally probable X-ray positions (Doxsey et al. 1977; Gursky et al. 1978). The high-energy LED detectors observed the spectrum upward to ≈ 100 keV (Cooke et al. 1984), and the A-2 detectors (1.5–30 keV) were used to measure the medium energy spectrum. An analysis of these latter data led White and Marshall (1984) to classify the source as a black hole candidate based on its very soft spectrum. During its 1977–1978 outburst, the source reached at least 70% of the intensity of the Crab (1–10 keV; Doxsey et al. 1977; Kaluzienski and Holt 1977), and the duration of the outburst was at least seven months (Kaluzienski & Holt 1977; Cooke et al. 1984).

The 2003 outburst was discovered by Revnivtsev et al. (2003) on March 21 using *INTEGRAL* and rediscovered a few days later by Markwardt & Swank (2003a), who initiated the first pointed *RXTE* observations of the source on March 28. Following some early confusion over the identity of the source (initially dubbed IGR/XTE J17464-3213), the X-ray nova was correctly identified with the earlier *HEAO-1* source based on its X-ray position (Markwardt & Swank 2003b). Shortly thereafter, a radio counterpart was discovered. The precise position of the radio source agrees with the *HEAO-1* X-ray position to $8''$ (Rupen, Mioduszewski, & Dhawan 2003), which left no doubt that the new transient and H1743–322 are one and the same. Shortly thereafter, a variable optical counterpart was identified, which is coincident with the radio counterpart (Steeghs et al. 2003; §3.6). The source has been closely monitored at radio wavelengths (e.g., Rupen et al. 2003; §3.5) and observed at optical wavelengths, despite the large interstellar extinction, $A_V \sim 12$ mags (§3.6). Light curves in the *I*- and *K*-band covering most of the outburst cycle and a pair of spectral energy distributions are presented by Buxton & Bailyn (2007).

The discovery of a pair of high-frequency QPOs at 240 Hz and 165 Hz is an especially important result, which was obtained using *RXTE* timing data (Homan et al. 2005; Remillard et al. 2006). Very similar pairs of high-frequency QPOs with a commensurate frequency ratio of 3:2 are seen for three other dynamical black-holes: XTE J1550–564, GRO J1650-40, and GRS 1915+105 (McClintock & Remillard 2006). Thus, the presence of this distinctive harmonic pair of frequencies further strengthens the black hole candidacy of H1743–322, and at the same time opens wider the possibility of obtaining fundamental information about black holes (e.g., Abramowicz & Kluzniak 2001; Remillard et al. 2002a; Wagoner

1999). Other recent work on H1743–322 includes a report on three high-energy *INTEGRAL* observations (Parmar et al. 2003), an investigation of the low-frequency QPOs (Homan et al. 2005), and a simultaneous *Chandra* and *RXTE* spectroscopic study (Miller et al. 2006).

Even more recently, several additional studies of H1743–322 have been published. They are not as comprehensive as the present work; however, they provide complementary and very valuable information on state transitions, timing behavior and the high-energy spectrum. For a thorough and independent spectral/temporal analysis of the *RXTE* data obtained during the last several weeks of the outburst, with an emphasis on state transitions, see Kalemci et al. (2006). For a further analysis of state transitions for selected *INTEGRAL/RXTE* observations, see Joinet et al. (2005). For additional analyses of *INTEGRAL/RXTE* spectra made at a number of epochs, see Capitanio et al. (2005, 2006) and Lutovinov et al. (2005).

Herein, we present spectral and timing results for 170 pointed X-ray observations, as well as extensive VLA radio observations. These observations span almost 8 months. Also presented are optical/NIR data and images for both the outburst and quiescent states. This work is a continuation of our program to study the spectral and timing behavior of Galactic black holes. Some comparable studies include, e.g., Ebisawa et al. (1994) on Nova Mus 1991, Sobczak et al. (1999) on GRO J1655–40, Sobczak (2000b) and Remillard et al. (2002b) on XTE J1550–564, Park et al. (2004) on 4U 1543–47, Belloni et al. (2005) on GX 339–4, and Tomsick et al. (2005) on 4U 1630–47.

This paper is organized as follows. In §2 we discuss the instrumentation and the X-ray, radio and optical/NIR observations, while emphasizing the very different X-ray spectral models used for analyzing the X-ray data during the two observing epochs. In §3, the spectral and timing parameters, the source fluxes and the VLA data are presented in plots and tables, and significant aspects of the data are discussed. In §4, we highlight some of the more interesting behavior exhibited by the source, and compare our results for H1743–322 to those obtained for XTE J1550–564 and other black hole sources. Finally, we offer our conclusions in §5.

2. X-ray Observations and Analysis

In Figure 1, we show the X-ray light curve of H1743–322 obtained in 2003 with the All-Sky Monitor (ASM) aboard *RXTE*. The intensity and hardness ratio are plotted versus “day number” which is referenced to 2003 March 21 (modified Julian date 52719), the day of discovery of the outburst (Revnivtsev et al. 2003). We use the day number for plots and refer to it throughout this work. We also make extensive use of the “observation number”

(obs. no.), which is tabulated along with the day number, the modified Julian date (MJD) and the calendar date for all 170 observations (see Appendix, Table A2).

In this work we present spectral and timing results for 170 observations of H1743–322 that were obtained over an 8-month period using the PCA and HEXTE instruments onboard RXTE. The times of the observations are indicated by the tick marks at the top of Figure 1. We report on the entire outburst cycle shown in Figure 1. The observations occurred on an essentially daily basis during the first 3.5 months when the source was most active. During the next 3 months the source was relatively stable and observations were made every 3–4 days. During the several weeks of hard-state activity that occurred during the end of the outburst cycle the source was again monitored on an almost daily basis. The 170 observations considered in this work include all of those obtained in our *RXTE* guest observer program (P80146) plus additional public observations of this source (P80138, P80144, P80135 and P80137).

2.1. Spectral Fitting

In this work we fitted simultaneously the pulse-height spectra obtained using only the best-calibrated detector modules. For the PCA this is PCU-2 and for the HEXTE we used only the data from cluster A. PCU-2 is a xenon-filled detector with an effective area of $\approx 1250 \text{ cm}^2$, an energy range of 3–60 keV, and an energy resolution of $\approx 18\%$ at 6 keV (Swank 1998). HEXTE-A is a cluster of 4 NaI/CsI detectors with an effective area of 800 cm^2 , which covers the energy range 15–250 keV (Rothschild et al. 1998).

The PCU-2 data were taken in the “standard 2” format, which consists of a series of 16-s accumulations of counts that were individually recorded in 129 pulse-height channels. The spectra were corrected for background and a systematic error of 1% was added to the count rates, which is required for bright sources in order to allow for uncertainties in the detector response. In like manner, the standard HEXTE reduction software was used to extract the HEXTE archive mode data. The HEXTE modules were alternately pointed every 32 s at source and background positions, allowing good background subtraction. All of the 170 pairs of PCA and HEXTE pulse-height spectra were fitted jointly over the energy ranges 2.8–25 keV (PCU-2; PHA channels 4–53) and 24–200 keV (HEXTE-A; PHA channels 13–56), respectively. The energy range used for PCU-2 is the current standard choice used to insure reliable calibration. For HEXTE-A, using the final spectral model (see below), we tried several different low-energy limits before selecting 24 keV as most suitable. The upper limit of 200 keV allowed us in every case to capture all of the detected counts without significantly degrading the signal-to-noise ratio relative to a 100 keV limit.

All the spectra were analyzed using XSPEC version 11.2.0 (Arnaud & Dorman 2003); the errors on both the spectral parameters (Table A2) and the fluxes (Table A3) are consistently given at the 68%/1- σ level of confidence. The basic model is comprised of the following three components: (1) the widely used model of a multitemperature blackbody accretion disk (Mitsuda et al. 1984; Makishima et al. 1986); (2) a broken power law or a simple power law (see below); and (3) an interstellar absorption component (Balucinska-Church & McCammon 1992; Yan, Sadeghpour, & Dalgarno 1998) with the hydrogen column fixed at $N_{\text{H}} = 2.2 \times 10^{22} \text{ cm}^{-2}$ (see below). In addition, a fourth component consisting of a Gaussian Fe K emission line was added when its inclusion improved the fit. The Gaussian line width was fixed at 1.2 keV (FWHM), and the central line energy was allowed to float from 6.4–7.0 keV. Interestingly, none of the fits were improved by the inclusion of a smeared Fe absorption edge (e.g., Ebisawa et al. 1994), which has been widely used in similar studies (e.g., Sobczak et al. 2000b; Park et al. 2004), and this component was not used at all.

A broken power-law component was essential in fitting many of the spectra obtained during the first half of the outburst cycle, i.e., obs. nos. 1–100 (see Tables A2 & A3). The parameters of this model are a pair of photon indices, a break energy E_b , and the normalization (photon flux at 1 keV). In a first pass through the data, the break energy was allowed to float. Approximately 75% of the fits returned the value $E_b \approx 15$ keV, and we obtained very satisfactory fits by fixing E_b at 15 keV for obs. nos. 2–100. The one exceptional case was obs. no. 1, for which we fixed E_b at 25 keV (Table A2). For the broken power-law model, the photon index of the high-energy power-law component (i.e., $E > 15$ keV) was allowed to vary independently for the PCU-2 (15–25 keV) and HEXTE-A (24–200 keV) detectors, although the normalization was fitted in common. This allows for continuous curvature in the source spectrum, which is being approximated here by a broken power law. As indicated in Figure 2, apart from the first two observations, the photon indices generally tracked each other very well over the course of the observations compared to the differences determined for the high- and low-energy photon indices (see §3.1). The high-energy photon index (Γ_{HI} ; 15–200 keV) that we report in §3 and Table A2 is a Gaussian-weighted average of the indices determined independently by the PCU-2 and HEXTE-A detectors.

In brief, the complete model has eight free parameters: two power-law photon indices and normalization plus a separate power-law index for HEXTE-A (see below); the accretion disk temperature and normalization; and the Fe line central energy (6.4–7.0 keV) and normalization. The two additional parameters, N_{H} and E_b , were fixed for all the fits at the values mentioned above.

For the remaining observations, obs. nos. 101–170, we simplified our spectral model by replacing the broken power-law component by a simple power-law component, and thereby

good fits were obtained to all of these spectra over the entire 2.8–200 keV interval. Consequently, the total number of free fitting parameters was at most six, a pair each for the power-law, disk, and Fe-line components. Again, the Fe line was included only when it improved the fit. The solid line in Tables A2 & A3 at obs. no. 100 indicates the transition from the broken power-law model to the simple power-law model.

For six singular observations, which are scattered throughout the outburst cycle (nos. 1–2, 46, 164, 167, and 170), the spectral fits returned nearly zero values for both the disk temperature and normalization. In these cases the thermal component is presumably too cool to be detected by RXTE. Because the disk component is irrelevant in fitting these spectra, we removed the disk blackbody component from the model, but otherwise fitted the spectra as described above. The first three of the six spectra named above (for obs. no. < 100) were fitted with the broken power-law model (six free parameters, including the Fe line), and the latter three were fitted with the simple power-law model (four free parameters, including the Fe line).

The value of N_{H} was determined in a preliminary analysis of a number of thermal-state spectra (obs. nos. 101–134) using a model composed of the three components described above: a disk blackbody, a simple power-law and interstellar absorption with variable N_{H} . In this way, we determined a Gaussian-weighted mean value of $N_{\text{H}} = 2.2 \times 10^{22} \text{ cm}^{-2}$, which we fixed in computing all of the results reported herein. This value is very similar to the values reported by others for this source (Doxsey et al. 1977; Parmar et al. 2003; Markwardt & Swank 2003a; Miller et al. 2004), and it agrees with the value determined from optical/NIR observations, $N_{\text{H}} = 2.1 \times 10^{22} \text{ cm}^{-2}$ (§3.6).

2.2. X-ray Timing Analysis

The computation of the X-ray power density spectra (PDS) and the search for QPOs follow the descriptions given by McClintock & Remillard (2006), and references therein. PDSs in the frequency range 4 mHz to 4 kHz were computed for data in the energy range 2–30 keV for all 170 observations. Low-frequency QPOs were detected in 87 of the 170 data sets, and the QPO parameters (central frequency, amplitude, and quality factor Q) are reported in Table A3. Also given in Table A3, in this case for all 170 observations, is the total rms power (r) integrated over 0.1–10 Hz (2–30 keV).

2.3. X-ray States of Black Hole Binaries

Extensive observations of many black hole binaries with RXTE have shown that luminosity is a poor criterion to use in defining the outburst states of these sources since each of the commonly identified states have been observed to span a range of two or more decades in X-ray luminosity. We thus use the state names introduced by McClintock and Remillard (2006) for the three principal states: namely, thermal dominant (TD; cf., high soft), hard (H; cf., low hard), and steep power law (SPL; cf., very high). Note that herein and in Remillard & McClintock 2006, we generally refer to the thermal dominant state as simply the thermal state. Because these revised state names are relatively unfamiliar, we list and define them in Table 1 in terms of the parameters that specify the energy spectra and the power density spectra. The state definitions in the table are identical to those given by Remillard & McClintock et al. (2006), and as indicated in footnotes *e* and *f*, they differ slightly from the original definition given by McClintock & Remillard (2006). We also recognize intermediate or hybrid states that lie between these three principal states. In these cases, we specify the admixture of the pair of principal states that describes the intermediate state in question (e.g., H:SPL) when possible.

Table 1. Outburst States of Black Holes: Nomenclature and Definitions

New State Name (Old State Name)	Definition of X-ray State ^a
Thermal (High/Soft)	Disk fraction ^b > 75% QPOs absent or very weak: $a^c < 0.005$ Weak power continuum: $r^d < 0.075^e$
Hard (Low/Hard)	Disk fraction ^b < 20% (i.e., Power-law fraction ^b > 80%) $1.4^f < \Gamma < 2.1$ Strong power continuum: $r^d > 0.1$
Steep Power Law (SPL) (Very high)	Presence of power-law component with $\Gamma > 2.4$ Power continuum: $r^d < 0.15$ Either disk fraction ^b < 80% and 0.1-30 Hz QPOs present with $a^c > 0.01$ or disk fraction ^b < 50% with no QPOs present.

^a2–20 keV band.

^bFraction of the total 2–20 keV unabsorbed flux.

^cQPO amplitude (rms).

^dTotal rms power integrated over 0.1–10 Hz.

^eFormerly $r < 0.06$ in McClintock & Remillard 2006.

^fFormerly $1.5 < \Gamma$ in McClintock & Remillard 2006.

2.4. VLA Radio Observations

We observed H1743–322 a total of about 50 times throughout the course of the outburst at 8.460 GHz and 4.860 GHz and about half that many times at 1.425 GHz. The radio data were reduced using the Astronomical Image Processing System (AIPS). During the first month of the outburst, about a dozen observations were made at each of three higher frequencies: 14.94 GHz, 22.46 GHz and 43.34 GHz. All of the radio data are summarized in Table A4–A6. The source was observed most frequently at 8.460 GHz and was reliably detected through day 114. The peak flux observed at this frequency was 68 mJy on day 18.5. Thereafter, our observations yielded only upper limits on the source flux ($S_\nu \lesssim 0.3$ mJy).

2.5. Optical and Near-infrared Observations

Optical images were obtained using the MagIC CCD camera mounted on the Magellan-Clay telescope at Las Campanas Observatory. This imager provides a 2.35' field of view sampled at $0.069''$ pixel $^{-1}$. On 2003 April 5.4 UT (day 15.4 of the outburst), 300 s Johnson R - and I -band images were obtained under seeing conditions of $0.48''$. We also secured 5x300 s i' -band exposures of the quiescent state on 2006 June 23.1 UT under photometric conditions and with a seeing of $0.43''$. The frames were de-biased and flatfielded and an astrometric frame in the ICRS J2000.0 system was calculated using a large number of 2MASS and UCAC2 reference stars.

Dithered K_s -band images, also of the quiescent state, were obtained during a total of 3 hours using the PANIC camera on the Magellan-Baade telescope on the nights of 2006 May 7–8 UT. PANIC (Persson's Auxiliary Nasmyth Infrared Camera: Martini et al. 2004) is a near-infrared camera with a pixel scale of $0.125''$ pixel $^{-1}$ that projects a 2' field of view onto a Rockwell 1024x1024 HgCdTe detector. Observations consisted of a 5-point dither pattern with a 25 s exposure that was repeated three times at each dither position, yielding a total of 6.25 min on source. The field of H1743–322 is crowded, and therefore each pair of 6-min dither sequences on the object was followed by a dithered observation of a relatively blank region of sky. These sky-blank frames were used to subtract the sky background from the target frames. We also observed the standard star S279-F (Persson et al. 1998), which we used for the absolute flux calibration. The reductions were done using PANIC/IRAF software. Seeing was typically $0.5''$. In addition to these quiescent images, K_s -band images of H1743–322 were obtained with the PANIC camera near the end of the 2003 outburst on day 175.1 (2003 September 12.1 UT). The same dither pattern was used with exposures of 10 s, giving 2.5 min on source in seeing of $0.5''$.

3. Results

The ASM light curve shown in Figure 1 provides a global view of the outburst. It reveals that during the first three months H1743–322 flared violently and exhibited a generally hard spectrum. Thereafter, the flaring subsided, and for several months the intensity of the source decayed smoothly and the spectrum was dominated by thermal emission from the accretion disk. During the final few weeks of decay, the source spectrum hardened and was dominated by the power-law component. The times of the 170 PCA/HEXTE pointed observations of the source are indicated by the tick marks at the top of Figure 1.

For an in-depth look at the outburst, we turn now to discuss the pointed observations. The results of all of the X-ray spectral and timing analyses performed on the 170 data sets are presented in two tables that are located in Appendix A: The spectral parameters are given in Table A2 and the fluxes and timing data in Table A3. We used these results and the state definitions given in Table 1 to determine objectively the state of the source during each of the 170 observations. Our state classifications are listed in the far-right column in Table A2, and they are displayed as color-coded symbols in Figure 3b, which is a plot of the 2–20 keV model flux computed using the spectral parameters given in Table A2.

Figure 3b provides a summary view of how the state of the source evolved during the course of the outburst. The source started and ended the outburst in the hard state (blue squares). Furthermore, on one other occasion during the outburst, namely day 58, the source returned briefly to the hard state. During the most intense period of flaring, the source was generally in the SPL state (green triangles), the period when high-frequency QPOs were detected (Homan et al. 2004; Remillard et al. 2006). Interestingly, in the middle of the flaring period (days 39–44), the source entered a thermal-state lull for five days. Commencing on day 87, the source again transitioned into the thermal state (red crosses). Thereafter it underwent a gradual and steady 4-month decay before subsiding into the hard state via the H:SPL intermediate state. The occurrence of intermediate states (magenta circles), which were common during the flaring phase and again near the end of the outburst, are all hybrids of the hard and SPL states (H:SPL) with two exceptions: On days 64 and 95 the source was found in a state intermediate between the thermal and SPL states (thermal:SPL; see Table A2).

This section is organized as follows. In §3.1 we present and discuss a pair of figures that illustrate the principal spectral and timing data contained in Tables A2 and A3. In §3.2 we show representative energy spectra for several of the observations. The thermal state is the subject of §3.3. In §3.4 we examine correlative relationships between the spectral and temporal data and also discuss an impulsive power-law flare observed on day 47. In §3.5, we present the radio data and discuss their connections with the X-ray data, and finally in §3.6

we present the optical/NIR results for both the outburst and quiescent states.

3.1. Spectral and Temporal Evolution of the Outburst

Figure 4 offers a detailed look at the full spectral evolution of the source (see also Tables A2 & A3). Panel *a* indicates the state of the source (see above). The spectral parameters are presented in panels *b*–*d*: the disk blackbody temperature (*b*), the inner disk radius (*c*), and the low- and high-energy photon indices (*d*). Flux data are shown in the five panels in the lower portion of the figure: the Fe K emission line flux (*e*); the disk, power-law, and total fluxes in the 2–20 keV band (*f*–*h*); and the hard flux in the 20–100 keV band (*i*). The complex behavior of the source during the first few months and its stable nature thereafter is as apparent in this record as it is in the ASM light curve (Fig. 1).

Figure 5 presents a companion view of the outburst cycle that reveals its temporal evolution. Shown are (*a*) the X-ray state, (*b*) the rms power, r , integrated over 0.1–10 Hz in the 2–30 keV band, (*c*) the central frequency of the dominant QPO, (*d*) its amplitude, and (*e*) its quality factor $Q = \nu/\Delta\nu$. For comparison, the Fe K line and disk fluxes are repeated from Figure 3 in (*f*) and (*g*), respectively. In this record, low-frequency QPOs and a strong power continuum are much in evidence throughout most of the first few months. They then disappear for the next few months, while the source remains fixed in its thermal state, before reappearing near the end of the outburst.

The outburst cycle can be divided into three main intervals. the first of these is the initial 87 days, which is marked by strong flaring activity and a generally dominant power-law component. During the second interval, the source remained locked in the thermal state for 125 days as its intensity gradually and monotonically decayed. During the last interval of 22 days, the spectrum hardened as the source made its return to the quiescent state. We now briefly discuss these time intervals in turn in relation to Figures 4 & 5.

Flaring Period – the first 87 days: As indicated in Figure 4, during days 8–22, the source transitioned from the initial hard state to the SPL state through a succession of intermediate (H:SPL) states. During this period the disk flux is very low, the power-law flux rises steadily, the Fe line flux reaches its outburst maximum, there is a large difference between the two spectral indices, and QPOs are present throughout (Fig. 5). Days 22–38 mark the period of most intense flaring. During this period the source is predominately in the SPL state, the disk flux and temperature is high, the power-law indices become less discordant, and the Fe line fades; the QPO frequency is high and the amplitude is low. Throughout days 38–44, the source remains in a thermal-state lull. Then, during days 44–64, the disk flux plummets and

remains low. The source alternates between the SPL and the hard:SPL states and briefly visits the hard state on day 57.7. This period is heralded by an impulsive flare that triples the power-law flux on day 46.9 (Figs. 4*g* & *i*). The power-law flux remains high, the two photon indices diverge strongly, the Fe line is intense, and the QPO amplitude is high. Days 64–87 mark the second flaring phase, which is dominated by the SPL state. Three additional power-law flares are seen on days 67.3, 75.6 and 79.5 (Figs. 4*g* & *i*), the disk temperature steadily falls, and the inner disk radius increases. QPOs of high frequency and low amplitude are present, and the power continuum plummets to a low value (Fig. 5).

Thermal period – days 87–212: With the exception of day 94.8, the source remains in its thermal state, QPOs are absent, and the power continuum is at its rock bottom level. During the entire interval, the disk temperature falls gradually and monotonically, and the inner disk radius is fairly constant, increasing smoothly by only $\approx 14\%$. The Fe line flux is undetectable or faint but strengthens near the end. The 2–20 keV power-law flux undergoes an initial rapid decay and then remains consistently low (Fig. 4*g*). Prior to day 170, the 20–100 keV power-law flux is extremely low, contributing only an average of 0.3% of the total flux (Table A3; Fig. 4*i*). However, thereafter the intensity of the hard flux increases suddenly by an order of magnitude and remains at this level of intensity on average through to the end of the interval on day 212. Prior to day 102, the 3–15 keV power-law index is relatively hard: $\langle \Gamma \rangle = 2.30$. However, on day 102, the index steepens dramatically from 2.6 to 3.5 in a single day (Fig. 5; Table A2). This steep power-law slope is maintained for about two weeks, and then a period of erratic variability sets in for almost ten weeks, during which the index varies from $\approx 2.3 – 3.8$. In the final few weeks, the index again achieves a stable value, although it has now again become quite hard: $\Gamma \approx 2.2$.

Transition to the Hard State – days 212–233: During the first two weeks of this period, the source is in the H:SPL intermediate state, QPOs reappear, and the power continuum climbs steadily to a local maximum of $r \approx 0.18$ on day 224 (Fig. 5*b*). During this same period, the QPO frequency declines steadily from an initial maximum of 7.9 Hz to a minimum of 2.5 Hz, and the amplitude increases to a maximum of 7.6% (Table A3). The power-law flux, which reemerged at the end of the previous period, strengthens further, reaching a maximum on day 219. During the final week of this period, the source enters its hard state and its intensity declines steadily, falling to a level of ≈ 7 mCrab (2–20 keV; Table A3) on the final day. The QPOs shift to lower frequencies, becoming undetectable on day 226. The Fe line flux declines steadily (Table A3), although its *EW* remains high (Table A2). The temperature of the disk falls rapidly, reaching undetectable levels ($\lesssim 0.45$ keV) on three occasions during the final week. There is a large apparent decrease in the inner radius of the disk; however, this is probably attributable to the effects of spectral hardening and the breakdown of the disk model, rather than a physical shrinking of the inner radius (e.g.,

Sobczak et al. 2000b).

3.2. Notable Behavior of the Intermediate State

Figure 6 shows enlarged plots of the Fe, disk and power-law fluxes and the QPO amplitude during the active period. Here the states are identified directly via our standard plotting symbols. At a glance, one sees that the intermediate H:SPL state is characterized by maximal values of both the Fe flux and the amplitude of the low-frequency QPO, and also by very low values of the disk flux. Furthermore, it is especially interesting to note that the very high level of Fe-line flux in the intermediate state is not accompanied by an especially strong component of power-law flux, as one might expect if the former is powered by the latter via fluorescence in the disk.

3.3. Representative Energy Spectra

Eight energy spectra are shown in Figures 7 that illustrate the range of spectra observed for H1743–322. Initially, on day 18.6, a strong power-law dominated the spectrum and a significant Fe-line component is present ($EW \approx 220$ eV). On day 41.8, the thermal component is ascendent for $E < 10$ keV, although a hard and intense power-law tail is also present. The SPL spectrum for day 46.9 shows the dominant power-law component that corresponds to the intense flare observed on that day (see §3.4.2). On day 57.7, the disk temperature falls below the threshold for detection ($T_{\text{in}} < 0.51$ keV), and a hard-state spectrum extending to ≈ 170 keV is observed. The SPL spectrum obtained on day 71.1 corresponds to the second epoch of flaring activity. The thermal spectrum for day 110.3 was obtained three weeks after the onset of the decay of the disk emission; note the faint and steep power-law component ($\Gamma = 5.4 \pm 1.8$). The spectrum for day 193.5 shows another example of thermal-state behavior that was observed late in the decay of the disk; note the similar thermal-state spectrum for day 41.8 and the dissimilar one for day 110.3. During the last 10 days of the outburst (day numbers > 223), the spectrum is in the hard state. However, the final observation shown here for day 233.3 is classified as H:SPL because the power-law index was slightly too soft ($\Gamma = 2.14 \pm 0.02$) to permit a hard-state classification (see Table A2).

3.4. Thermal State: Comparison with XTE J1550–564

For many years, the thermal state has been modeled successfully using a simple multitemperature accretion disk model (e.g., Shakura & Sunyaev 1973; Mitsuda et al. 1984; Makishima et al. 1986). The significant successes of this approach derive from the relative simplicity of this state for which the power-law component is weak, QPOs are absent or very weak, and the power continuum is faint (§2.3). Following Kubota, Makishima & Ebisawa (2001), the simplicity of the thermal state is well illustrated by plotting the bolometric luminosity of the disk component versus the disk temperature. Figure 8 shows such plots for H1743–322 and XTE J1550–564; the latter plot is based on the tabulated results in Sobczak et al. (2000b).

The approximately $L_{\text{disk}} \propto T_{\text{in}}^4$ correlation shown in Figure 8 strongly supports a simple accretion disk model, and it shows that there exists an inner disk radius that is relatively constant in the thermal state. This fact, which is also apparent in Figure 4c, has been well known for about 20 years; e.g., see Fig. 3.14 in Tanaka & Lewin (1995). As Tanaka & Lewin commented over a decade ago, the constancy of this inner radius suggests that it is related to the innermost stable circular orbit predicted by general relativity.

For both sources, the bolometric disk luminosity rises with temperature somewhat more slowly than T_{in}^4 (Fig. 8), or, equivalently, R_{in} decreases somewhat with increasing temperature. For example, during the 4-month decay in the thermal state (day numbers 88–211) the radius increases by $\approx 20\%$ (Fig. 4c; Table A2).

3.5. SPL, Hard and Intermediate States

In §3.5.1, we present results for phenomena that are relatively unimportant in the thermal state, namely, QPOs, the 0.1–10 Hz power continuum and the power-law component. As we show for the H:SPL intermediate state in particular, there are strong correlations between the 2–20 keV disk flux, the QPO parameters, the continuum power and the photon power-law index. Furthermore, these correlations are strikingly similar for the two sources. In §3.5.2, we compare the strongest of the impulsive power-law flares observed for H1743–322 to the extraordinary 7-Crab flare that was observed during the 1998–1999 outburst of XTE J1550–564.

3.5.1. Spectral/Temporal Correlations: Transitions between Hard and SPL States

QPOs were detected for 87 of the 170 observations (Table A3). For these observations, in Figures 9–13 we present selected correlation plots relating the QPO frequency, disk flux, 3–15 keV photon index, QPO amplitude and continuum power density for both H1743–322 and XTE J1550–564. For the latter source, the spectral and QPO data were obtained from Sobczak et al. (2000b) and Remillard et al. (2002b), respectively, except for the rms continuum power data, which we computed for this work. A wider assortment of such correlation plots have been presented previously for the black hole X-ray novae XTE J1550–564 and GRO J1655–40 by Sobczak et al. (2000a) and Remillard et al. (2002b), and we refer the reader to these works for further detail.

Figure 9 shows the QPO frequency plotted versus the disk luminosity for H1743–322 and XTE J1550–564. The striking feature of these plots are the very similar and apparently linear correlations that exist at relatively low values of the disk luminosity as the source transitions between the hard and SPL states via the intermediate H:SPL state. Note that the tight correlations for both sources extend over approximately the same ranges of frequency and luminosity. We refer to the data in Figure 9 that are identified by a nearby black dot and that are replotted in isolation in Figure 10 as the “strongly correlated” data. For H1743–322, these observations have disk fluxes $f_D \leq 0.3 \times 10^{-8}$ ergs cm $^{-2}$ s $^{-1}$ and are plotted in red in Figure 4f. They correspond in Table A3 to obs. nos. 1–11 (excluding 8) and 36–53. For XTE J1550–564, the strongly correlated data correspond to the first 38 days of data (i.e., through MJD 51102) that are plotted in Figure 4e in Sobczak et al. (2000b), with the exception of the one observation that occurred during the 7 Crab flare on MJD 51075.99; these data correspond to $f_D \leq 1.2 \times 10^{-8}$ ergs cm $^{-2}$ s $^{-1}$. For both sources, one significant feature of the strongly correlated data is that the power-law flux is typically about an order of magnitude greater than the disk flux.

Figure 11 shows the QPO frequency plotted versus the 3–15 keV photon index Γ . The strongly correlated data (again identified by small black dots) are well isolated from the other data for $\nu_{\text{QPO}} \lesssim 5$ Hz; however, they blend into the poorly correlated data at higher QPO frequencies. As expected for the strongly correlated data, which link the hard state and the SPL state, Figure 11 shows that the power-law index sweeps smoothly from $\Gamma_{\text{LO}} \approx 1.5$ to ≈ 2.7 as the QPO frequency (disk flux) increases, and as the source makes the transition from the hard state to the SPL state.

Figure 12 shows that the continuum power density is strongly anticorrelated with QPO frequency. Furthermore, the strongly correlated data (marked by black dots) are shown here very sharply separated from the poorly correlated data. Figure 13 shows a weaker anticorrelation between QPO amplitude and QPO frequency. The amplitude generally de-

creases as the frequency increases. The amplitudes are quite high at low frequencies and very comparable for the two sources.

We conclude that in state transitions between the hard and SPL states, approximately linear, strong and repeatable correlations can exist between the disk flux, QPO frequency, and continuum power. These three quantities also correlate, although more weakly, with the low-energy power-law index and the QPO amplitude. Finally, the correlations observed for H1743–322 and XTE J1550–564 are very similar, particularly for the strongly correlated data. For these correlated data it is especially interesting to note that the absolute ranges of the correlations are very nearly the same for the two sources, namely, $\nu \lesssim 7$ Hz, $L_x \lesssim 4 \times 10^{37}$ erg s^{−1}, and $r \lesssim 0.22$.

3.5.2. Impulsive Power-Law Flares

Brief flares in the power-law flux were observed in single PCA observations on days 32.3, 46.9, 67.3, 75.6 and 79.5 (Fig. 4*g* & 4*i*). All of these flare events occurred in the SPL state. During the strongest of these events, which occurred on day 46.9, the 2–20 keV flux increased by a factor of 2.5, and the 20–100 keV flux increased by a factor of 3.5 (Fig. 4*g* & 4*i*; Table A3). The increases in power-law flux are accompanied by corresponding apparent decreases in the inner disk radius (Fig. 4*c*) and increases in the disk temperature (Fig. 4*b*).

It is of interest to compare the giant flare observed for XTE J1550–564 on 1998 September 19–20 (Sobczak et al. 2000b) with the most intense flare observed for H1743–322, which occurred on day 46.9. For both sources, the flares occurred in the SPL state (Remillard & McClintock 2006). Superficially, these flares appear quite similar. For example, for both flares the power-law flux increased by the same factor of 2.5 (Table A3; Sobczak et al. 2000b). More importantly, the total peak 2–20 keV X-ray luminosities were quite comparable: $L_{\text{max}}(\text{H1743–322}) = 0.9 \times 10^{39}$ erg s^{−1} and $L_{\text{max}}(\text{XTE J1550–564}) = 1.1 \times 10^{39}$ erg s^{−1}. The luminosity for the disk component is an isotropic average for the distance estimates given in §4.3, where we have assumed $i = 70^\circ$ for both sources. We assume that the source of the power-law emission is isotropic. Finally, we note that both flares were observed only during a single, daily PCA observation.

As shown in Figure 14, in the case of XTE J1550–564 the impact of the giant flare on the spectrum of the thermal component was far greater than that observed for H1743–322. For example, in the former system the apparent inner radius of the disk decreased by a factor of 16 during the flare and the apparent disk temperature quadrupled, reaching $kT = 3.3$ keV. The variations in the case of H1743–322 are much smaller: The fitted values of the inner

disk radius decreased by a factor of ≈ 2 , and the disk temperature rose by only $\approx 50\%$. The behavior of the disk and Fe-line fluxes, which are quite different for the two sources, are also compared in Figure 14.

We placed limits on the durations of these flares by examining the ASM count rate data within 10 days of the flare events. The ASM detected the giant flare of XTE J1550–564 during eight dwells, which bracket the time of the PCA observation, these data establish that the flare’s duration was at least 0.87 days, but not more than 2.0 days. The H1743–322 flare event was not captured by the ASM, but it was recorded throughout the 3.4 ks PCA observation. We thus conclude that its duration was at least 0.04 days, but not more than 1.55 days.

Obviously, the snapshot character of both the ASM and pointed PCA observations provide an unsatisfactory glimpse of these powerful and infrequent flares. The capabilities of future missions will be required to time-resolve such events.

3.6. VLA Radio Results: Comparisons with X-ray Data

Measurements of the radio flux densities at 1.425, 4,860 and 8.460 GHz, which span the entire outburst cycle, are shown in Figure 15*b*, and the state of the X-ray source is indicated above in panel *a*. Strong radio flares approaching a flux of 100 mJy were observed during the first half of the outburst, whereas only upper limits were obtained during the second half. Observations at 14.940 GHz and two higher frequencies were made during the first 37 days of the outburst. These data, which are shown in Figure 15*c*, also exhibit strong flaring behavior. For comparison, the 2–20 keV power-law component of the X-ray flux is shown in Figure 15*d*. The radio flux fades to ~ 1 mJy on day 80, while the X-ray source is still in the SPL state. The radio flux further decays to the detection limit (see Table A4) on day 114, which is well into the period of slow thermal-state decay of the source and follows by 27 days the transition from the SPL state into the thermal state.

A closer comparison between the radio flux and certain X-ray quantities is displayed in Figure 16, which covers only the first 120 days of the outburst when the radio/X-ray source was most active. As usual, the state of the X-ray source is indicated in panel *a*. The X-ray quantities shown are (*b*) the 2–20 keV power-law flux, (*c*) the difference between the high-energy and low-energy photon indices ($\Gamma_{HI} - \Gamma$), and (*d*) the Fe K line flux. These X-ray quantities were selected because they correlate best with the behavior of the contemporaneous radio data, which are shown superimposed and arbitrarily scaled in each of the three panels *b*–*c*. For clarity, only the 8.460 GHz radio data, which was the most frequently

sampled band, are overplotted on the X-ray data. The radio spectral index α , which is based on the 4.860 and 8.460 GHz data, is plotted in panel *e*. All of the radio data plotted in Figures 15 & 16 are given in Tables A4–A6. Further discussion of the VLA results are given in §4.6.

3.7. The Optical and Near-infrared Counterpart

In Figure 17, we compare optical observations of the field in quiescence (*a*) and in outburst (*b*). The latter observations were made early in the 2003 outburst cycle on day 15.4 and show a counterpart consistent with the VLA radio position at a brightness level of $I = 19.3$ and $R = 21.9$ (Steeghs et al. 2003). These magnitudes plus the K -band magnitude of $K_s = 13.9 \pm 0.2$ obtained on the same night (Baba et al. 2003) suggest a reddening that is consistent with the Schlegel et al. (1998) estimate of $E_{B-V} = 3.5$ mag, which implies $N_H = 2.1 \times 10^{22} \text{ cm}^{-2}$ for $A_V = 11.6$ mag (Schlegel et al. 1998; Prehdel & Schmitt 1995). This is almost precisely the same value we obtained by analyzing the *RXTE* data: $N_H = 2.2 \times 10^{22} \text{ cm}^{-2}$ (§2.1). Using the extinction law of Schlegel et al., this reddening estimate suggests de-reddened magnitudes of $I_0 = 12.5$ and $R_0 = 12.6$ on day 15.4 (April 5.4 UT). The position of the source in the ICRS frame is $\alpha(\text{J2000}) = 17^h 46^m 15^s.6$ and $\delta(\text{J2000}) = -32^\circ 14' 00''.9$, whose accuracy is limited by the $0.25''$ rms of the astrometric solution. We were unable to detect the source in quiescence during deep i' -band exposures on 2006 June 23 (Fig. 17*a*), implying a quiescent magnitude limit of $i' > 24$. This in turn implies an outburst amplitude in the optical of over 4.5 magnitudes. At the same time, our dereddened magnitudes above, our distance estimate of 10 kpc (§4.3), and an assumed value of $(V - R)_0 = -0.1$ imply a quite luminous counterpart with $M_V = -2.5$ (e.g., see van Paradijs & McClintock 1994).

Figure 18*a* shows the best K_s image ($0.43''$ seeing), which was obtained on 2006 May 7.4 UT. The location of the quiescent counterpart is consistent with the optical and radio positions (Rupen et al. 2003). PSF photometry (Stetson 1987) was performed to derive a quiescent magnitude of $K_s = 17.1 \pm 0.1$. The comparison K_s -band image in Figure 18*b* shows the counterpart as it appeared near the end of the outburst on day 175.1 (2005 September 12.1 UT).

4. Discussion

4.1. The Evolution of H1743–322 and other X-ray Novae

The spectral and temporal evolution of H1743–322 (Figs. 1, 3–5) are markedly similar to those observed for XTE J1550–564 in 1998–1999 (Sobczak et al. 2000b; Remillard & McClintock 2006) and for GRO J1655–40 in 1996–1997 (Sobczak et al. 1999; Remillard et al. 2002b; Remillard & McClintock 2006). The outburst cycles of all three sources show a double-peaked profile. During the first maximum, each source primarily exhibited strong flaring behavior and intense nonthermal emission, whereas during the second maximum the source spectrum was generally soft and thermal (Remillard & McClintock 2006). H1743–322 deviated somewhat from this pattern because the second maximum begins in a strongly nonthermal state. Nevertheless, the outburst cycles of all three sources followed the same general sequence of events: (1) a rapid rise to maximum, (2) several months of strong flaring activity, (3) several months of slow decay in the thermal state, and (4) a final stage of rapid decay into quiescence.

An even more complex evolution was observed for the recent outburst of the recurrent X-ray nova 4U1630–47. This source flared strongly throughout its long outburst and did not display a lengthy period of decay in the thermal state (Tomsick et al. 2005). As is well known, a significant number of other X-ray novae display simple light curves that rise rapidly, decay exponentially, and are relatively devoid of flaring behavior. These include such sources as A0620–00, Nova Mus 1991, GS2000+25, and 4U 1543–47 (Tanaka & Lewin 1995; Park et al. 2004). It has recently been suggested that the relative complexity of the light curves of X-ray novae may in part be caused by inclination effects (Narayan & McClintock 2005).

Figure 3 shows the evolution of the X-ray states for H1743–322 throughout its outburst cycle. The light curve is divided into an initial period of flaring behavior followed by a subsequent passive period of comparable duration (a few to several months). The epoch of flaring begins upon discovery with the source intensity rising in the hard state. This rise is followed by months of violent X-ray and radio flaring and the production of high-and low-frequency QPOs (Remillard et al. 2002b). During this period, all of the X-ray states (except for the quiescent state) are seen, although the SPL and H:SPL intermediate states are ascendent during these periods of strong flaring and high luminosity.

During the second and passive epoch, the source spectrum is predominately thermal, except near the time of the final decay when the hard and intermediate states reappear (e.g., see Fig. 3). During the thermal phase, the disk temperature falls slowly and monotonically, and the inner disk radius remains quite stable with a value comparable to the estimated radius of the last stable orbit (Tanaka & Lewin 1995; McClintock & Remillard 2006). The

power-law component is generally weak during the second epoch, and there is a near-absence of QPO and flaring activity. In the case of XTE J1550–564 and GRO J1655–40, there is a lull in intensity that separates the two epochs. H1743–322 exhibits a similar lull near day 55; however, it occurs well before the termination of the flaring phase (Fig. 3).

For a thorough discussion of physical models of the three active emission states that considers emission mechanisms, geometry, results from multiwavelength studies, etc., see §7 in Remillard & McClintock (2006).

4.2. The Intermediate State: Fe K line and Spectral/Temporal Correlations

Figure 6 shows that the H:SPL intermediate state is characterized by maximal values of the QPO amplitude ($\approx 12\%$) and Fe line intensity. The extreme flux in the Fe line is remarkable given the moderate strength of the power-law flux (Fig. 6c), since the widely accepted view is that the Fe line is fluoresced in the cold accretion disk by the hard power-law flux. Note that the relatively high power-law flux that is often present in the SPL state (Fig. 6c) yields relatively much lower Fe line fluxes (Fig. 6a). Perhaps the higher efficiency of the intermediate state for producing the Fe line is due to a favorable geometry or is related in some way to the large amplitude of the QPOs.

Below ≈ 7 Hz, H1743–322 and XTE J1550–564 exhibit very similar and nearly linear correlations between the QPO frequency and disk flux (Fig. 9 & 10) that extend over more than a decade in both frequency and flux. Similar quasi-linear relations between these two quantities have been observed for other sources, such as for the 1–15 Hz QPOs in GRS 1915+105 (Markwardt, Swank, & Taam 1999; Munoz, Morgan, & Remillard 1999) and the 20–30 Hz QPOs in XTE J1748-288 (Revnivtsev, Trudolyubov, & Borozdin 2000). In addition, correlations between the photon index and QPO frequency (Fig. 11) have been extensively studied by Titarchuk & Fiorito (2004) and Titarchuk & Shaposhnikov (2005). The ubiquity of such correlations for black hole binaries and the striking similarities in the behaviors of H1743–322 and XTE J1550–564 (Figs. 9–13) motivate us to examine closely these strongly correlated data (which are identified in the figures by an adjacent, small black dot; §3.5.1).

As stressed by Sobczak et al. (2000a) and others, the tight correlation between QPO frequency and disk flux suggests that the accretion disk regulates the frequency of the QPO oscillations, and that the QPO frequency is slaved to the rate of mass accretion through the inner disk. However, as Sobczak et al. and others also stress, the QPO phenomenon is closely related to the presence of the power-law component, which must reach a threshold of $\sim 20\%$

of the total (2–20 keV) flux to trigger the variable low-frequency QPOs. For H1743–322 we find a similar but higher threshold of $\sim 40\%$ (Table A3). However, the power-law component is more than simply a trigger: It must also participate directly in the oscillations because when the QPO amplitude is large ($\sim 10–15\%$), the rms amplitude often exceeds the fraction of the total flux supplied by the disk alone (Table A3). Also, the energy spectrum of the QPOs is generally hard, indicating that the bulk of the flux is derived from the power-law component (Muno et al. 1999; Sobczak et al. 2000b).

For the strongly correlated data (§3.5.1), it is important to note that the power-law component is totally dominant: The power-law flux is $\gtrsim 80\%$ of the total flux when the QPO frequency and disk flux are strongly correlated. This is true for both H1743–322 and XTE J1550–564. Thus, although it is the disk flux that figures in the tight correlations shown in Figures 9 & 10, nevertheless, the bulk of the total flux is supplied by the power-law component.

One might attempt to account roughly for the behavior of the two sources in the strongly-correlated regime as follows. As shown in Figure 11, at the lowest level of disk flux the spectral index is 1.5, the QPO frequency is very low, and the source is in the hard state. This condition is in reasonable accord with our independent view of the hard state: namely, an inner disk radius that has receded to a few hundred (e.g., 300) Schwarzschild radii, which corresponds to a Keplerian frequency of ~ 0.2 Hz ($M = 10 M_\odot$; e.g., Yuan, Cui & Narayan 2005), and a disk so cool that it does not contribute to the flux above ~ 1 keV. As the disk flux (and temperature) increases, the QPO frequency is seen to rise to ≈ 7 Hz, and the power-law spectrum softens monotonically to $\Gamma \sim 2.7$ (Fig. 11). These results are consistent with the conventional picture of a disk edge moving smoothly inward to a radius of ≈ 30 Schwarzschild radii (corresponding to a Keplerian frequency of ≈ 7 Hz). One might expect that the increased presence of the disk in the inner region could soften the hard spectrum and also account for the strong Fe line, which could be fluoresced by the dominant power-law component.

This simple picture is, however, quite inadequate. For example, the observed disk temperature of $\lesssim 0.8$ keV is much too high to be explained by a standard model of disk accretion for an inner disk radius of $\gtrsim 30R_S$. Furthermore, the mechanism required to generate the large-amplitude QPOs in both the disk and power-law components is unclear. Nevertheless, there is good reason to focus on these strongly correlated data for H1743–322 and XTE J1550–564 because they showcase the very orderly transition that occurs between the hard and SPL states and may provide a toehold in attempts to understand the SPL state in particular.

4.3. Speculations on Mass, Inclination and Distance

The optical counterpart is heavily reddened, faint and lies in a crowded field (§3.7). Thus, dynamical optical data, which are often available to determine the mass, inclination and distance of a black hole binary (Charles & Coe 2005), will probably not be forthcoming soon. Consequently, we briefly discuss some alternative and quite uncertain estimates of these quantities.

The 240 Hz and 160 Hz high frequency QPOs (Homan et al. 2005; Remillard et al. 2006) in conjunction with a preliminary relationship between QPO frequency and black hole mass (McClintock & Remillard 2006), suggest a mass of about $11 M_{\odot}$. The complex X-ray light curve of H1743–322 suggests that the orbital inclination of the system is quite high, $i \sim 70^{\circ}$ (Narayan and McClintock 2005). Indeed, the two systems with very similar X-ray light curves that we referred to earlier, XTE J1550–564 and GRO J1655–40 (§4.1), do have high inclinations of $\approx 70^{\circ}$ (Orosz 2003). Concerning distance, in this work we have assigned a nominal value of 10 kpc. This value allowed for very reasonable comparisons to be made between the properties of H1743–322 and XTE J1550–564 (with an estimated distance of 5.5 kpc) that are discussed in §3.4 & §3.4.1 and illustrated in Figures 8 & 9–13. Furthermore, H1743–322 is located near the Galactic center ($l = 357.3$, $b = -1.8$), which also suggests a distance of this magnitude.

Thus, we suggest that H1743–322 is located at a distance of about 10 kpc, the binary system has a high inclination, $i \sim 70^{\circ}$, and the mass of the black hole is about $10\text{--}12 M_{\odot}$.

4.4. Thermal State and the Inner Disk Radius

In Figure 8, the bolometric disk luminosity is seen to deviate from the simple T^4 dependence for both XTE J1550–564 and H1743–322; most notably, it increases less rapidly than T^4 . At least in part, this is likely due to an increase in the spectral hardening factor with temperature/luminosity (Shimura & Takahara 1995; Davis et al. 2005). As an aside, it is informative to plot the disk component observed in the SPL and intermediate states in the $\log T:\log L$ plane, although we have not done so in Figure 8. An analysis of extensive *RXTE* spectral observations of GRO J1655–40 and XTE J1550–564 has shown that as the power-law component becomes stronger and steeper, the disk luminosity and radius appear to decrease while the temperature remains high. These results can be interpreted as an observational confirmation of strong Comptonization of disk photons in the SPL state (Kubota, Makishima, & Ebisawa 2001; Kubota & Makishima 2004; Kubota & Done 2004).

4.5. Impulsive Power Law Flares

This response of the disk parameters to intense flares has been observed for several black hole binaries (e.g., Sobczak et al. 1999, 2000b) and has been attributed to increased spectral hardening or Compton upscattering of soft disk photons; the actual physical radius may remain fairly constant. For a thorough discussion see Sobczak et al. (2000b).

The most remarkable power-law flare ever observed for a black hole binary occurred early in the outburst cycle of XTE J1550–564. The flare reached a peak intensity of 6.8 Crab (2–10 keV) on 1998 September 19–20 (Sobczak et al. 2000b). Soon after this strong flare, superluminal radio jets ($> 2c$) were observed (Hannikainen et al. 2001). A few years later, large-scale (~ 20 arcsec) radio and X-ray jets were discovered, which were most likely ejected during the September 1998 event (Corbel et al. 2002; Tomsick et al. 2003; Kaaret et al. 2003). Recently, a similar pair of large-scale, synchrotron-emitting jets have been reported for H1743–322 (Corbel et al. 2005). By analogy with the behavior of XTE J1550–564, it is reasonable to suppose that these jets are connected with the impulsive flare events described in §3.4.2.

4.6. Radio/X-ray Connections

It is unreasonable to expect a point-by-point correlation between the X-ray and radio data shown in Figure 16 because the ASM light curve (dwell by dwell) shows strong X-ray variability on a time scale as short as minutes, and the X-ray and radio observations were typically separated by \gtrsim hours (compare Tables A3 & A4). For example, for the tripling of the radio flux that occurred on day 18.5 (Fig. 15; Table A4), the proximate X-ray observation did not commence for over 2 hours (Table A3). Similarly, the radio observation nearest the intense power-law X-ray flare that occurred on day 46.9 (Table A3) occurred 10.7 hours earlier.

Nevertheless, all three of the X-ray quantities shown in Figure 16b–d appear to be generally correlated with the radio data. Arguably it is the break in the power-law spectrum at 15 keV ($\Gamma_{\text{HI}} - \Gamma$) that best correlates with the radio data.

5. Conclusions

We have performed a spectral and timing analysis of 170 *RXTE* observations that cover the complete 2003 outburst cycle. The spectra were decomposed into disk-blackbody and

power-law components. A power law broken at 15 keV was adopted for the first half of the outburst cycle, and a simple power law was used for the second half. Additionally, a Gaussian Fe-K emission line component was included whenever it improved the fit. Power density spectra were computed and the level of the power continuum was determined for all 170 data sets. QPOs in the range 1–15 Hz were detected for 87 of the data sets, and the frequency, intensity and quality factor Q of the dominant QPO were obtained. All of the products of these spectral and timing analyses are contained in Tables A2 & A3, and most of the results are summarized in Figures 4 & 5, which present a detailed look at the spectral and temporal evolution of the 2003 outburst.

Using the results contained in Tables A2 & A3, we classified the state of the source according to the criteria summarized in Table 1 (McClintock & Remillard 2006), which are based on the power-law spectral index, the relative strengths of the power-law and disk components, the presence or absence of QPOs, and the strength of the power density continuum. These objective state classifications, which are a key ingredient of this work, are displayed in Figures 3–6, 9–13, & 15–16, listed in Table A2, and referred to throughout the text.

The X-ray properties of H1743–322 and XTE J1550–564 are very similar, including the general character of their X-ray light curves, the occasional appearance of impulsive power-law flares (Fig. 14), and their long and slow decline in the thermal state with $L_{\text{disk}} \propto T_{\text{in}}^4$ (Figs. 3, 4 & 8). Most notable, however, are the nearly identical and tight correlations that exist between the low-luminosity disk flux, the QPO frequency, and the 0.1–1 Hz continuum power. These results, which are displayed in Figures 9–13, illustrate that the transition between the hard and SPL states can be remarkably orderly and stereotypical. The strong and linear correlations exist only when the source is in the H:SPL intermediate state and break down when the source reaches either the hard or the SPL state (Figs. 9 & 10). Furthermore, as shown for H1743–322 in Figure 6, this intermediate state is also distinguished by its very strong QPOs and by its high efficiency for producing Fe-line flux. These and other results presented herein illustrate the power of the state classification system summarized in Table 1.

We present VLA data at six frequencies that extend throughout the entire outburst cycle at 4.860 GHz and 8.460 GHz. The radio source was observed to be active only during the first ≈ 100 days (Fig. 15). Finally, we present optical/NIR data and finding charts (Figs. 17 & 18) for the optical counterpart in both outburst and quiescence.

This work was supported in part by NASA grant NNG05GB31G. MAPT was supported by NASA LTSA grant NAG-5-10889 and DS acknowledges the support of a Smithsonian Astrophysical Observatory Clay fellowship. We thank Jean Swank and her staff for support

and for the execution of the *RXTE* observations and David Kaplan for obtaining the 2003 Magellan/MagIC images.

A. Results of X-ray and Radio Analyses in Tabular Form

Tables A2 & A3 contain all of the X-ray spectral parameters and fluxes that are displayed in Figures 4 & 5 for the 170 observations. The tables also relate the day number (used in Figs. 1–6 and Figs. 15 & 16) to the UT date and MJD, and they assign an index number to each observation. For each observation, Table A2 also provides the following additional information that is not presented in the figures: the value of χ^2_ν and the central energy, photon flux and equivalent width of the Fe K line. Likewise, Table A3 contains two quantities that are not included in the figures: the exposure time for each observation and the ratio of the disk flux to the total flux (2–20 keV).

All of the flux density data plotted in Figures 15b & c versus day number are contained in Tables A4 & A5, respectively. The tables also give the correspondence between day number and the UT date and MJD. Table A6 gives 25 values of the radio spectral index that were determined during the first 115 days of the outburst cycle.

Table A2. Spectral Parameters for H1743-322

Obs. No.	UT 2003 (mmdd)	Day ^a	MJD ^b	T_{in} (keV)	$R_{\text{in}}^*{}^c$ (km)	Γ^d	$\Gamma_{\text{HI}}{}^e$	Power-Law Norm. ^f	$E_{\text{line}}{}^g$ (keV)	$N_{\text{line}} \times 100^h$	EW ⁱ (eV)	$\chi_{\nu}^2{}^j$	State ^k
1	0328	7.8	52726.850	< 0.444	(25.0)	1.49 ± 0.01	1.79 ± 0.02	0.16 ± 0.01	6.40 ± 1.01	0.08 ± 0.03	75	2.52	H ^l
2	0331	10.8	52729.809	< 0.462	(25.0)	1.56 ± 0.01	2.22 ± 0.01	0.46 ± 0.01	6.40 ± 0.44	0.38 ± 0.06	147	2.05	H ^{l,m}
3	0404	14.8	52733.762	0.729 ± 0.098	16.93 ± 6.23	2.19 ± 0.02	2.78 ± 0.01	3.00 ± 0.17	6.40 ± 0.32	1.37 ± 0.19	257	1.16	H:SPL
4	0406	16.7	52735.734	1.264 ± 0.021	8.38 ± 0.36	2.22 ± 0.03	2.99 ± 0.02	3.46 ± 0.27	0.92	H:SPL
5	0408	18.6	52737.580	0.450 ± 0.039	79.66 ± 21.55	2.24 ± 0.01	2.96 ± 0.01	6.31 ± 0.21	6.40 ± 0.26	2.22 ± 0.36	223	1.05	H:SPL
6	0410	20.7	52739.678	0.814 ± 0.091	19.10 ± 5.55	2.43 ± 0.02	3.12 ± 0.01	9.40 ± 0.53	6.40 ± 0.38	2.23 ± 0.38	206	0.95	H:SPL
7	0412	22.8	52741.854	1.149 ± 0.032	13.83 ± 0.97	2.62 ± 0.04	3.02 ± 0.02	10.36 ± 0.96	6.40 ± 0.90	0.82 ± 0.43	81	0.90	SPL
8	0414	24.2	52743.240	1.268 ± 0.012	15.36 ± 0.61	2.62 ± 0.03	3.05 ± 0.01	16.01 ± 1.13	1.13	SPL
9	0415	25.2	52744.220	1.112 ± 0.046	14.47 ± 1.45	2.62 ± 0.03	3.14 ± 0.01	14.81 ± 1.22	6.40 ± 0.98	1.01 ± 0.56	75	1.11	SPL
10	0417	27.2	52746.195	1.104 ± 0.037	12.04 ± 0.86	2.38 ± 0.04	3.12 ± 0.02	4.07 ± 0.40	6.40 ± 0.83	0.59 ± 0.28	95	1.02	H:SPL
11	0418	28.6	52747.633	1.113 ± 0.034	13.67 ± 1.04	2.64 ± 0.03	3.03 ± 0.02	9.54 ± 0.85	6.40 ± 1.33	0.49 ± 0.37	55	1.15	SPL
12	0421	31.3	52750.313	1.587 ± 0.015	10.65 ± 0.44	2.50 ± 0.03	3.02 ± 0.01	13.95 ± 0.98	0.88	SPL
13	0421	31.8	52750.810	1.441 ± 0.011	12.57 ± 0.46	2.61 ± 0.03	2.97 ± 0.01	15.34 ± 1.04	0.80	SPL
14	0422	32.1	52751.089	1.380 ± 0.009	13.47 ± 0.40	2.57 ± 0.03	2.97 ± 0.01	10.66 ± 0.83	0.88	SPL
15	0422	32.3	52751.316	1.526 ± 0.014	14.01 ± 0.57	2.55 ± 0.03	3.29 ± 0.01	23.55 ± 1.59	1.92	SPL ^o
16	0422	32.7	52751.714	1.339 ± 0.008	15.45 ± 0.46	2.74 ± 0.03	2.89 ± 0.02	14.47 ± 1.13	0.83	SPL ^o
17	0422	33.0	52751.987	1.319 ± 0.007	16.79 ± 0.41	2.78 ± 0.03	2.92 ± 0.02	13.39 ± 1.12	0.75	SPL
18	0423	34.0	52752.972	1.518 ± 0.013	11.58 ± 0.46	2.56 ± 0.03	2.98 ± 0.01	15.45 ± 1.05	0.72	SPL
19	0424	34.2	52753.167	1.585 ± 0.017	10.11 ± 0.47	2.51 ± 0.03	3.00 ± 0.01	14.43 ± 0.99	0.83	SPL
20	0425	35.6	52754.575	1.332 ± 0.009	15.09 ± 0.45	2.65 ± 0.03	2.91 ± 0.01	12.80 ± 1.01	0.89	SPL
21	0426	37.0	52755.960	1.249 ± 0.004	27.37 ± 0.43	2.89 ± 0.04	3.28 ± 0.02	18.68 ± 1.89	2.01	SPL ^o
22	0427	37.2	52756.219	1.250 ± 0.005	25.31 ± 0.45	2.90 ± 0.04	3.17 ± 0.02	16.90 ± 1.76	1.92	SPL
23	0427	37.7	52756.714	1.242 ± 0.005	18.26 ± 0.36	2.86 ± 0.04	2.98 ± 0.03	9.26 ± 0.95	0.55	SPL
24	0428	38.8	52757.803	1.182 ± 0.004	23.64 ± 0.19	2.67 ± 0.07	2.41 ± 0.02	2.69 ± 0.47	0.86	TD
25	0429	40.0	52758.996	1.168 ± 0.002	34.12 ± 0.34	3.25 ± 0.09	3.48 ± 0.08	9.34 ± 2.19	1.30	TD
26	0501	41.1	52760.081	1.191 ± 0.004	23.56 ± 0.19	2.48 ± 0.08	2.41 ± 0.03	1.86 ± 0.37	0.93	TD
27	0501	41.6	52760.558	1.170 ± 0.008	24.61 ± 0.32	2.64 ± 0.09	2.44 ± 0.03	2.78 ± 0.69	6.96 ± 0.74	0.37 ± 0.25	59	1.16	TD
28	0501	41.8	52760.854	1.194 ± 0.004	28.55 ± 0.20	2.53 ± 0.06	2.51 ± 0.01	2.75 ± 0.45	1.13	TD
29	0502	42.0	52761.039	1.183 ± 0.003	29.64 ± 0.25	2.92 ± 0.07	2.60 ± 0.03	5.42 ± 1.06	0.91	TD
30	0502	42.6	52761.612	1.188 ± 0.004	29.01 ± 0.22	2.53 ± 0.06	2.48 ± 0.02	3.08 ± 0.53	0.98	TD
31	0503	43.7	52762.746	1.200 ± 0.005	27.83 ± 0.23	2.32 ± 0.05	2.48 ± 0.01	2.71 ± 0.38	0.76	TD
32	0504	44.1	52763.095	1.221 ± 0.004	26.59 ± 0.31	2.72 ± 0.05	2.80 ± 0.02	8.78 ± 1.08	1.16	SPL
33	0504	44.6	52763.617	1.269 ± 0.005	22.84 ± 0.43	2.79 ± 0.04	2.93 ± 0.03	15.22 ± 1.45	0.74	SPL
34	0505	45.9	52764.907	1.265 ± 0.005	23.06 ± 0.39	2.77 ± 0.03	2.94 ± 0.01	15.05 ± 1.35	1.32	SPL
35	0506	46.9	52765.867	1.626 ± 0.021	11.26 ± 0.62	2.42 ± 0.02	2.99 ± 0.01	22.04 ± 1.45	0.80	SPL

Table A2—Continued

Obs. No.	UT 2003 (mmdd)	Day ^a	MJD ^b	T_{in} (keV)	$R_{\text{in}}^{* \text{ c}}$ (km)	Γ^{d}	$\Gamma_{\text{HI}}^{\text{e}}$	Power-Law Norm. ^f	$E_{\text{line}}^{\text{g}}$ (keV)	$N_{\text{line}} \times 100^{\text{h}}$	EW ⁱ (eV)	$\chi_{\nu}^{2 \text{j}}$	State ^k
36	0507	47.6	52766.575	0.924 ± 0.039	25.73 ± 2.71	2.61 ± 0.03	2.97 ± 0.02	14.38 ± 1.00	6.40 ± 0.49	2.10 ± 0.56	162	0.98	SPL
37	0508	48.9	52767.865	0.841 ± 0.039	28.22 ± 3.45	2.50 ± 0.02	3.06 ± 0.01	9.97 ± 0.56	6.40 ± 0.36	2.36 ± 0.41	222	0.80	H:SPL
38	0509	49.5	52768.547	0.983 ± 0.040	20.03 ± 1.93	2.56 ± 0.03	3.03 ± 0.02	10.91 ± 0.85	6.40 ± 0.74	1.18 ± 0.48	108	0.76	SPL
39	0510	50.7	52769.746	0.926 ± 0.039	22.36 ± 2.31	2.51 ± 0.03	3.02 ± 0.02	9.49 ± 0.68	6.40 ± 0.53	1.58 ± 0.43	155	1.04	H:SPL
40	0511	51.5	52770.535	1.016 ± 0.039	19.65 ± 1.77	2.61 ± 0.03	3.02 ± 0.01	13.88 ± 1.03	6.40 ± 0.61	1.57 ± 0.54	122	0.95	SPL
41	0512	52.9	52771.868	0.701 ± 0.059	32.81 ± 8.05	2.29 ± 0.02	2.98 ± 0.01	6.15 ± 0.30	6.40 ± 0.34	2.23 ± 0.30	246	0.99	H:SPL
42	0513	53.7	52772.739	0.599 ± 0.070	37.13 ± 13.7	2.13 ± 0.02	2.87 ± 0.01	4.47 ± 0.19	6.40 ± 0.26	2.28 ± 0.29	260	1.49	H:SPL
43	0514	54.7	52773.725	0.570 ± 0.067	40.34 ± 17.5	2.15 ± 0.01	2.89 ± 0.01	4.63 ± 0.16	6.40 ± 0.24	2.12 ± 0.29	242	1.81	H:SPL
44	0515	55.6	52774.582	0.838 ± 0.056	20.98 ± 3.65	2.29 ± 0.02	2.96 ± 0.01	5.83 ± 0.32	6.40 ± 0.34	2.12 ± 0.33	240	1.25	H:SPL
45	0516	56.6	52775.634	0.763 ± 0.078	20.68 ± 5.92	2.16 ± 0.02	2.89 ± 0.01	4.38 ± 0.22	6.40 ± 0.30	2.13 ± 0.29	257	1.60	H:SPL
46	0517	57.7	52776.684	< 0.513	(25.0)	2.06 ± 0.01	2.73 ± 0.01	2.95 ± 0.03	6.40 ± 0.55	0.65 ± 0.14	100	1.93	H ¹
47	0518	58.7	52777.667	0.740 ± 0.063	24.65 ± 5.72	2.23 ± 0.02	2.90 ± 0.01	5.08 ± 0.26	6.40 ± 0.29	2.22 ± 0.27	263	1.19	H:SPL
48	0519	59.5	52778.526	0.818 ± 0.053	22.44 ± 3.78	2.31 ± 0.02	2.94 ± 0.01	5.90 ± 0.32	6.40 ± 0.34	2.09 ± 0.30	243	1.23	H:SPL
49	0520	60.6	52779.584	0.851 ± 0.048	23.00 ± 3.31	2.40 ± 0.02	2.99 ± 0.01	7.09 ± 0.42	6.40 ± 0.39	1.89 ± 0.35	209	1.00	H:SPL
50	0521	61.6	52780.598	0.834 ± 0.048	24.57 ± 3.65	2.40 ± 0.02	2.95 ± 0.01	7.15 ± 0.44	6.40 ± 0.39	2.01 ± 0.36	222	0.96	H:SPL
51	0522	62.6	52781.616	0.799 ± 0.044	26.13 ± 3.71	2.38 ± 0.02	2.95 ± 0.01	6.83 ± 0.37	6.40 ± 0.36	1.97 ± 0.30	225	0.97	H:SPL
52	0523	63.7	52782.697	0.933 ± 0.038	21.59 ± 2.13	2.43 ± 0.03	2.95 ± 0.01	7.14 ± 0.50	6.40 ± 0.49	1.51 ± 0.38	166	1.04	TD:SPL
53	0524	64.5	52783.510	1.071 ± 0.032	18.73 ± 1.21	2.55 ± 0.03	2.94 ± 0.01	11.01 ± 0.87	6.40 ± 0.79	1.10 ± 0.51	90	1.00	SPL
54	0525	65.6	52784.568	1.245 ± 0.006	21.88 ± 0.39	2.64 ± 0.03	2.81 ± 0.01	12.63 ± 1.07	1.36	SPL
55	0526	66.5	52785.483	1.242 ± 0.007	21.96 ± 0.41	2.64 ± 0.03	2.82 ± 0.01	13.63 ± 1.12	1.07	SPL
56	0527	67.3	52786.350	1.350 ± 0.010	16.47 ± 0.53	2.58 ± 0.03	2.88 ± 0.01	17.57 ± 1.29	0.80	SPL
57	0527	67.8	52786.846	1.237 ± 0.007	21.19 ± 0.50	2.66 ± 0.03	2.82 ± 0.01	14.91 ± 1.27	0.89	SPL
58	0528	68.0	52787.044	1.221 ± 0.006	23.72 ± 0.44	2.69 ± 0.04	2.80 ± 0.02	12.06 ± 1.23	1.13	SPL
59	0528	68.2	52787.237	1.193 ± 0.005	25.08 ± 0.41	2.75 ± 0.04	2.72 ± 0.02	10.35 ± 1.19	0.91	SPL
60	0528	68.5	52787.492	1.226 ± 0.005	23.60 ± 0.34	2.68 ± 0.03	2.78 ± 0.01	12.22 ± 1.04	1.80	SPL
61	0529	69.0	52788.025	1.227 ± 0.007	22.31 ± 0.49	2.68 ± 0.03	2.74 ± 0.02	14.25 ± 1.29	0.94	SPL
62	0529	69.5	52788.506	1.144 ± 0.009	27.88 ± 0.46	2.70 ± 0.05	2.72 ± 0.01	7.27 ± 1.01	7.00 ± 1.11	0.51 ± 0.33	57	0.86	SPL
63	0529	69.9	52788.878	1.148 ± 0.010	31.57 ± 0.51	2.35 ± 0.08	2.39 ± 0.02	2.93 ± 0.65	6.48 ± 0.40	1.01 ± 0.56	74	0.82	TD
64	0530	70.3	52789.264	1.210 ± 0.005	24.77 ± 0.35	2.67 ± 0.04	2.79 ± 0.02	10.03 ± 1.02	0.99	SPL
65	0530	70.9	52789.930	1.203 ± 0.006	24.13 ± 0.39	2.70 ± 0.04	2.74 ± 0.02	10.68 ± 1.10	1.10	SPL
66	0531	71.1	52790.129	1.177 ± 0.011	24.69 ± 0.55	2.69 ± 0.05	2.76 ± 0.02	10.00 ± 1.32	6.69 ± 0.66	0.58 ± 0.48	49	0.76	SPL
67	0531	71.2	52790.236	1.198 ± 0.005	24.95 ± 0.32	2.67 ± 0.04	2.75 ± 0.01	8.93 ± 0.92	0.99	SPL
68	0531	71.9	52790.916	1.137 ± 0.009	30.71 ± 0.50	2.52 ± 0.07	2.52 ± 0.02	4.44 ± 0.82	7.00 ± 1.09	0.57 ± 0.37	62	0.74	SPL
69	0601	72.6	52791.632	1.157 ± 0.010	27.18 ± 0.50	2.69 ± 0.05	2.71 ± 0.01	8.54 ± 1.13	7.00 ± 1.32	0.47 ± 0.37	49	1.10	SPL
70	0602	73.0	52792.036	1.130 ± 0.009	28.99 ± 0.54	2.66 ± 0.07	2.63 ± 0.03	5.86 ± 1.02	7.00 ± 1.29	0.45 ± 0.34	54	0.85	SPL

Table A2—Continued

Obs. No.	UT 2003 (mmdd)	Day ^a	MJD ^b	T_{in} (keV)	$R_{\text{in}}^*{}^c$ (km)	Γ^d	Γ_{HI}^e	Power-Law Norm. ^f	$E_{\text{line}}{}^g$ (keV)	$N_{\text{line}} \times 100^h$	EW ⁱ (eV)	$\chi_{\nu}^2{}^j$	State ^k
71	0602	73.4	52792.390	1.184 ± 0.005	24.79 ± 0.34	2.71 ± 0.04	2.74 ± 0.01	10.18 ± 0.94	1.29	SPL
72	0603	74.0	52793.024	1.133 ± 0.005	28.28 ± 0.32	2.68 ± 0.05	2.64 ± 0.03	5.95 ± 0.79	1.22	SPL
73	0603	74.6	52793.607	1.163 ± 0.010	27.03 ± 0.54	2.71 ± 0.05	2.72 ± 0.02	9.47 ± 1.31	6.93 ± 0.84	0.49 ± 0.40	45	1.03	SPL
74	0604	75.6	52794.559	1.377 ± 0.010	15.79 ± 0.50	2.50 ± 0.03	2.87 ± 0.01	15.53 ± 1.17	1.01	SPL
75	0605	76.4	52795.381	1.120 ± 0.009	29.23 ± 0.54	2.68 ± 0.05	2.69 ± 0.02	7.11 ± 1.00	7.00 ± 1.02	0.56 ± 0.34	65	0.94	SPL
76	0606	77.3	52796.265	1.172 ± 0.006	25.45 ± 0.34	2.68 ± 0.03	2.74 ± 0.01	10.12 ± 0.90	1.29	SPL
77	0607	78.6	52797.583	1.155 ± 0.012	25.47 ± 0.60	2.69 ± 0.04	2.72 ± 0.01	11.31 ± 1.24	6.81 ± 0.51	0.72 ± 0.45	61	1.37	SPL
78	0609	79.5	52798.535	1.358 ± 0.011	16.00 ± 0.56	2.48 ± 0.03	2.84 ± 0.01	16.09 ± 1.21	0.86	SPL
79	0609	80.5	52799.455	1.120 ± 0.010	28.64 ± 0.57	2.72 ± 0.05	2.65 ± 0.02	7.81 ± 1.10	6.99 ± 1.00	0.54 ± 0.34	64	0.96	SPL
80	0610	81.7	52800.732	1.111 ± 0.009	31.38 ± 0.50	2.41 ± 0.05	2.48 ± 0.01	3.18 ± 0.46	7.00 ± 0.88	0.56 ± 0.32	69	1.14	SPL
81	0611	82.9	52801.915	1.152 ± 0.005	26.54 ± 0.31	2.66 ± 0.04	2.73 ± 0.01	7.84 ± 0.78	1.20	SPL
82	0612	84.0	52802.963	1.129 ± 0.011	27.07 ± 0.58	2.65 ± 0.05	2.72 ± 0.01	8.33 ± 1.01	6.99 ± 0.84	0.65 ± 0.36	71	1.26	SPL
83	0613	84.6	52803.568	1.122 ± 0.011	26.78 ± 0.59	2.64 ± 0.04	2.68 ± 0.01	7.99 ± 0.93	7.00 ± 1.39	0.42 ± 0.34	48	1.03	SPL
84	0614	85.6	52804.623	1.117 ± 0.014	25.71 ± 0.69	2.64 ± 0.04	2.66 ± 0.01	9.71 ± 1.01	6.76 ± 0.47	0.72 ± 0.43	70	0.93	SPL
85	0615	86.5	52805.472	1.110 ± 0.012	26.74 ± 0.66	2.66 ± 0.04	2.70 ± 0.01	9.31 ± 1.03	6.84 ± 0.38	0.83 ± 0.38	84	1.17	SPL
86	0616	87.6	52806.627	1.074 ± 0.010	32.80 ± 0.65	2.31 ± 0.06	2.39 ± 0.02	2.22 ± 0.36	6.89 ± 0.28	0.84 ± 0.32	115	0.88	TD
87	0617	88.6	52807.619	1.091 ± 0.009	32.80 ± 0.58	2.23 ± 0.08	2.31 ± 0.03	1.46 ± 0.31	6.84 ± 0.38	0.62 ± 0.33	81	0.87	TD
88	0618	89.6	52808.636	1.078 ± 0.009	33.19 ± 0.61	2.19 ± 0.07	2.34 ± 0.02	1.29 ± 0.23	6.93 ± 0.36	0.65 ± 0.28	95	0.99	TD
89	0619	90.6	52809.620	1.070 ± 0.008	33.61 ± 0.58	2.24 ± 0.07	2.36 ± 0.02	1.24 ± 0.24	6.95 ± 0.45	0.57 ± 0.26	94	0.86	TD
90	0620	91.5	52810.540	1.061 ± 0.007	34.11 ± 0.55	2.29 ± 0.11	2.37 ± 0.04	0.68 ± 0.20	7.00 ± 0.89	0.32 ± 0.21	63	0.94	TD
91	0621	92.5	52811.461	1.058 ± 0.008	33.54 ± 0.61	2.22 ± 0.08	2.22 ± 0.02	0.99 ± 0.21	7.00 ± 0.58	0.59 ± 0.24	110	0.89	TD
92	0622	93.7	52812.667	1.052 ± 0.008	33.71 ± 0.63	2.27 ± 0.08	2.31 ± 0.02	1.05 ± 0.22	6.85 ± 0.30	0.54 ± 0.25	98	0.70	TD
93	0623	94.8	52813.828	1.057 ± 0.007	33.78 ± 0.55	2.22 ± 0.08	2.29 ± 0.02	0.70 ± 0.15	7.00 ± 0.71	0.38 ± 0.20	75	0.80	TD:SPL
94	0624	95.5	52814.475	1.050 ± 0.008	34.67 ± 0.61	2.19 ± 0.11	2.22 ± 0.03	0.58 ± 0.17	7.00 ± 0.63	0.47 ± 0.22	97	0.87	TD
95	0625	96.8	52815.836	1.036 ± 0.007	34.76 ± 0.53	2.43 ± 0.16	2.30 ± 0.06	0.59 ± 0.25	7.00 ± 0.65	0.39 ± 0.18	95	0.69	TD
96	0626	97.6	52816.581	1.049 ± 0.003	33.29 ± 0.28	2.28 ± 0.11	2.39 ± 0.06	0.39 ± 0.11	0.94	TD
97	0627	98.5	52817.509	1.038 ± 0.006	34.56 ± 0.49	2.34 ± 0.13	2.35 ± 0.05	0.52 ± 0.17	7.00 ± 0.87	0.27 ± 0.17	64	0.82	TD
98	0628	99.5	52818.548	1.050 ± 0.003	33.66 ± 0.27	2.28 ± 0.12	2.54 ± 0.07	0.35 ± 0.11	0.98	TD
99	0629	100.3	52819.343	1.028 ± 0.007	34.96 ± 0.56	2.38 ± 0.17	2.40 ± 0.08	0.50 ± 0.22	6.99 ± 0.78	0.31 ± 0.18	78	0.69	TD
100	0630	101.4	52820.431	1.031 ± 0.003	34.49 ± 0.27	2.64 ± 0.19	2.53 ± 0.15	0.59 ± 0.30	0.66	TD
101	0701	102.4	52821.416	1.023 ± 0.005	34.56 ± 0.44	3.50 ± 0.20	...	3.27 ± 1.66	6.40 ± 1.06	0.29 ± 0.21	48	0.73	TD
102	0702	103.5	52822.531	1.026 ± 0.004	34.35 ± 0.40	3.54 ± 0.17	...	3.31 ± 1.45	6.98 ± 1.07	0.15 ± 0.13	42	0.77	TD
103	0703	104.5	52823.482	1.028 ± 0.002	33.27 ± 0.26	3.57 ± 0.15	...	3.21 ± 1.20	1.19	TD
104	0704	105.5	52824.453	1.029 ± 0.002	33.22 ± 0.38	3.95 ± 0.16	...	6.42 ± 2.54	0.80	TD
105	0705	106.4	52825.366	1.024 ± 0.003	33.32 ± 0.44	3.96 ± 0.16	...	7.11 ± 2.27	0.97	TD

Table A2—Continued

Obs. No.	UT 2003 (mmdd)	Day ^a	MJD ^b	T_{in} (keV)	$R_{\text{in}}^*{}^c$ (km)	Γ^d	Γ_{HI}^e	Power-Law Norm. ^f	E_{line}^g (keV)	$N_{\text{line}} \times 100^h$	EW ⁱ (eV)	$\chi_{\nu}^2{}^j$	State ^k
106	0706	107.4	52826.425	1.032 ± 0.002	33.01 ± 0.33	3.77 ± 0.14	...	5.29 ± 1.90	0.80	TD
107	0707	108.4	52827.411	1.030 ± 0.002	32.75 ± 0.33	3.73 ± 0.16	...	4.57 ± 1.78	0.84	TD
108	0708	109.4	52828.369	1.021 ± 0.002	33.96 ± 0.23	3.53 ± 0.14	...	2.73 ± 0.98	0.97	TD
109	0709	110.3	52829.277	1.018 ± 0.002	33.23 ± 0.32	3.82 ± 0.13	...	5.44 ± 1.83	1.03	TD
110	0710	111.2	52830.186	1.027 ± 0.003	33.13 ± 0.43	3.58 ± 0.24	...	3.15 ± 1.88	1.07	TD
111	0711	112.5	52831.483	1.016 ± 0.002	33.98 ± 0.30	3.62 ± 0.15	...	3.82 ± 1.43	0.74	TD
112	0714	115.2	52834.213	1.017 ± 0.002	33.37 ± 0.32	3.77 ± 0.14	...	4.95 ± 1.74	0.96	TD
113	0717	118.2	52837.201	1.017 ± 0.002	33.55 ± 0.36	3.88 ± 0.18	...	4.93 ± 2.17	1.35	TD
114	0720	121.6	52840.561	1.010 ± 0.003	34.68 ± 0.26	2.95 ± 0.17	...	0.76 ± 0.33	0.99	TD
115	0723	124.5	52843.513	0.995 ± 0.005	35.36 ± 0.51	2.60 ± 0.09	...	0.55 ± 0.14	7.00 ± 0.95	0.18 ± 0.13	59	1.11	TD
116	0726	127.2	52846.166	0.999 ± 0.002	34.58 ± 0.24	3.34 ± 0.15	...	1.72 ± 0.65	0.96	TD
117	0729	130.9	52849.911	0.988 ± 0.002	34.52 ± 0.29	3.66 ± 0.17	...	2.99 ± 1.27	1.06	TD
118	0730	131.9	52850.926	0.988 ± 0.003	34.23 ± 0.44	3.85 ± 0.16	...	5.45 ± 2.19	1.21	TD
119	0801	134.0	52852.991	0.976 ± 0.005	36.04 ± 0.52	3.11 ± 0.23	...	0.98 ± 0.58	6.98 ± 0.97	0.16 ± 0.13	60	0.87	TD
120	0804	136.5	52855.543	0.979 ± 0.002	34.65 ± 0.35	3.80 ± 0.17	...	4.06 ± 1.73	0.92	TD
121	0811	143.4	52862.382	0.953 ± 0.006	36.23 ± 0.60	3.18 ± 0.24	...	1.16 ± 0.71	6.46 ± 0.61	0.24 ± 0.16	66	0.87	TD
122	0814	146.4	52865.407	0.956 ± 0.002	34.38 ± 0.43	3.73 ± 0.18	...	3.84 ± 1.67	0.83	TD
123	0818	150.4	52869.351	0.952 ± 0.003	34.13 ± 0.38	3.47 ± 0.19	...	2.36 ± 1.08	0.70	TD
124	0824	156.1	52875.121	0.932 ± 0.006	35.64 ± 0.66	3.26 ± 0.26	...	1.23 ± 0.79	6.55 ± 0.60	0.16 ± 0.14	59	0.68	TD
125	0826	158.7	52877.700	0.925 ± 0.006	36.25 ± 0.77	3.19 ± 0.40	...	0.94 ± 0.94	7.00 ± 1.39	0.15 ± 0.12	88	1.10	TD
126	0901	164.3	52883.292	0.915 ± 0.005	35.44 ± 0.55	3.28 ± 0.19	...	1.35 ± 0.66	6.87 ± 0.53	0.12 ± 0.08	71	0.72	TD
127	0904	167.6	52886.574	0.924 ± 0.003	33.15 ± 0.65	4.18 ± 0.15	...	8.61 ± 3.00	1.96	TD ^p
128	0906	169.9	52888.932	0.909 ± 0.003	35.38 ± 0.33	3.30 ± 0.15	...	1.57 ± 0.57	1.77	TD
129	0909	172.4	52891.433	0.897 ± 0.006	36.85 ± 0.75	2.38 ± 0.06	...	0.38 ± 0.06	6.40 ± 0.71	0.24 ± 0.13	88	0.97	TD
130	0912	175.1	52894.054	0.901 ± 0.006	36.14 ± 0.73	2.17 ± 0.09	...	0.21 ± 0.05	7.00 ± 1.19	0.14 ± 0.10	94	1.12	TD
131	0916	179.7	52898.724	0.867 ± 0.008	37.47 ± 0.98	2.41 ± 0.11	...	0.34 ± 0.09	6.40 ± 0.58	0.38 ± 0.14	175	0.88	TD
132	0918	181.9	52900.879	0.866 ± 0.007	37.72 ± 0.91	2.95 ± 0.24	...	0.67 ± 0.39	6.40 ± 0.84	0.25 ± 0.12	121	0.91	TD
133	0921	185.0	52903.988	0.850 ± 0.007	38.22 ± 0.90	2.88 ± 0.22	...	0.68 ± 0.36	6.40 ± 0.85	0.26 ± 0.12	140	0.94	TD
134	0923	187.0	52905.958	0.843 ± 0.009	38.98 ± 1.18	2.17 ± 0.14	...	0.17 ± 0.06	6.40 ± 0.63	0.40 ± 0.14	219	0.81	TD
135	0924	187.1	52906.083	0.845 ± 0.006	37.93 ± 0.88	2.42 ± 0.08	...	0.31 ± 0.06	6.55 ± 0.27	0.25 ± 0.09	165	0.89	TD
136	0926	189.5	52908.515	0.847 ± 0.006	37.29 ± 0.81	2.24 ± 0.07	...	0.18 ± 0.03	6.61 ± 0.24	0.26 ± 0.08	192	0.82	TD
137	0927	190.6	52909.571	0.843 ± 0.005	36.91 ± 0.75	2.13 ± 0.05	...	0.19 ± 0.02	6.81 ± 0.19	0.29 ± 0.06	248	1.15	TD
138	0929	192.5	52911.546	0.828 ± 0.006	38.16 ± 0.92	2.13 ± 0.03	...	0.28 ± 0.02	6.43 ± 0.24	0.44 ± 0.09	265	1.06	TD
139	0930	193.5	52912.531	0.834 ± 0.006	36.69 ± 0.81	2.12 ± 0.03	...	0.35 ± 0.02	6.90 ± 0.20	0.30 ± 0.06	236	1.10	TD
140	1002	195.5	52914.504	0.798 ± 0.006	39.55 ± 0.90	2.19 ± 0.06	...	0.20 ± 0.03	6.40 ± 0.33	0.39 ± 0.07	299	1.02	TD

Table A2—Continued

Obs. No.	UT 2003 (mmdd)	Day ^a	MJD ^b	T_{in} (keV)	R_{in}^* ^c (km)	Γ^{d}	$\Gamma_{\text{HI}}^{\text{e}}$	Power-Law Norm. ^f	$E_{\text{line}}^{\text{g}}$ (keV)	$N_{\text{line}} \times 100^{\text{h}}$	EW ⁱ (eV)	χ_{ν}^{j}	State ^k
141	1004	197.4	52916.408	0.786 ± 0.006	38.77 ± 0.90	2.12 ± 0.03	...	0.25 ± 0.02	6.58 ± 0.13	0.41 ± 0.06	397	0.93	TD
142	1005	198.6	52917.591	0.789 ± 0.006	37.78 ± 0.99	2.13 ± 0.04	...	0.24 ± 0.02	6.46 ± 0.20	0.38 ± 0.07	326	1.04	TD
143	1008	201.1	52920.148	0.771 ± 0.005	37.70 ± 0.82	2.27 ± 0.08	...	0.18 ± 0.03	6.77 ± 0.19	0.22 ± 0.04	370	1.01	TD
144	1009	202.5	52921.474	0.748 ± 0.007	39.26 ± 1.21	2.26 ± 0.08	...	0.18 ± 0.03	6.40 ± 0.35	0.32 ± 0.05	402	0.89	TD
145	1012	205.2	52924.157	0.719 ± 0.006	40.85 ± 1.13	2.18 ± 0.07	...	0.14 ± 0.02	6.40 ± 0.30	0.30 ± 0.04	483	0.72	TD
146	1014	207.2	52926.198	0.703 ± 0.006	40.01 ± 1.16	2.26 ± 0.05	...	0.20 ± 0.03	6.40 ± 0.30	0.20 ± 0.04	403	1.23	TD
147	1015	208.1	52927.118	0.687 ± 0.006	41.44 ± 1.33	2.30 ± 0.06	...	0.19 ± 0.03	6.40 ± 0.34	0.23 ± 0.03	449	0.98	TD
148	1016	209.5	52928.507	0.674 ± 0.007	41.70 ± 1.56	2.24 ± 0.07	...	0.19 ± 0.03	6.40 ± 0.36	0.26 ± 0.04	526	0.96	TD
149	1017	210.4	52929.351	0.662 ± 0.006	40.57 ± 1.30	2.12 ± 0.04	...	0.16 ± 0.02	6.40 ± 0.24	0.30 ± 0.03	592	1.37	TD
150	1017	211.0	52929.967	0.669 ± 0.007	39.96 ± 1.39	2.11 ± 0.04	...	0.18 ± 0.02	6.40 ± 0.28	0.27 ± 0.03	505	0.86	TD
151	1018	212.0	52930.953	0.668 ± 0.009	37.58 ± 1.65	2.21 ± 0.03	...	0.37 ± 0.03	6.40 ± 0.25	0.38 ± 0.04	497	0.78	H:SPL
152	1020	213.1	52932.110	0.686 ± 0.012	29.28 ± 1.72	2.16 ± 0.02	...	0.45 ± 0.03	6.44 ± 0.15	0.49 ± 0.04	531	0.68	H:SPL
153	1021	214.3	52933.294	0.637 ± 0.007	39.81 ± 1.50	2.14 ± 0.04	...	0.20 ± 0.02	6.40 ± 0.25	0.27 ± 0.03	571	0.93	H:SPL
154	1022	215.0	52934.016	0.653 ± 0.011	33.13 ± 1.80	2.18 ± 0.03	...	0.37 ± 0.02	6.40 ± 0.22	0.39 ± 0.04	530	0.90	H:SPL
155	1023	216.1	52935.071	0.620 ± 0.010	37.82 ± 2.04	2.24 ± 0.04	...	0.31 ± 0.03	6.40 ± 0.29	0.25 ± 0.03	448	1.14	H:SPL
156	1024	217.0	52936.046	0.617 ± 0.015	33.64 ± 2.89	2.22 ± 0.03	...	0.38 ± 0.03	6.40 ± 0.30	0.31 ± 0.04	453	0.98	H:SPL
157	1025	218.0	52937.038	0.653 ± 0.018	23.47 ± 2.14	2.12 ± 0.02	...	0.36 ± 0.02	6.40 ± 0.23	0.38 ± 0.04	500	1.15	H:SPL
158	1026	219.0	52938.016	0.595 ± 0.029	24.42 ± 3.98	2.14 ± 0.03	...	0.40 ± 0.03	6.57 ± 0.17	0.25 ± 0.04	337	1.11	H:SPL
159	1027	220.1	52939.132	0.546 ± 0.038	29.04 ± 7.28	2.18 ± 0.03	...	0.39 ± 0.03	6.40 ± 0.42	0.20 ± 0.04	278	1.03	H:SPL
160	1030	223.2	52942.154	0.547 ± 0.060	18.50 ± 7.55	1.92 ± 0.03	...	0.18 ± 0.01	6.40 ± 0.39	0.17 ± 0.03	344	0.90	H
161	1030	223.7	52942.700	0.420 ± 0.061	43.09 ± 29.7	1.97 ± 0.03	...	0.18 ± 0.01	6.40 ± 0.52	0.13 ± 0.04	264	0.96	H
162	1101	225.2	52944.200	0.473 ± 0.047	23.16 ± 10.1	1.91 ± 0.01	...	0.14 ± 0.01	6.40 ± 0.28	0.12 ± 0.16	293	1.24	H
163	1102	226.2	52945.178	0.691 ± 0.065	8.22 ± 2.41	1.75 ± 0.04	...	0.08 ± 0.01	6.40 ± 0.35	0.19 ± 0.27	582	0.81	H
164	1103	227.2	52946.171	< 0.416	(25.0)	1.99 ± 0.01	...	0.13 ± 0.01	6.48 ± 0.43	0.03 ± 0.01	90	2.26	H ^q
165	1104	228.1	52947.053	0.506 ± 0.127	16.49 ± 16.4	1.87 ± 0.06	...	0.09 ± 0.01	6.41 ± 0.53	0.10 ± 0.04	401	0.91	H
166	1105	229.2	52948.234	0.581 ± 0.070	9.85 ± 4.08	1.87 ± 0.03	...	0.07 ± 0.01	6.40 ± 0.25	0.13 ± 0.02	576	1.26	H
167	1106	230.2	52949.195	< 0.443	(25.0)	2.03 ± 0.01	...	0.10 ± 0.01	6.52 ± 0.27	0.03 ± 0.01	156	2.37	H ^q
168	1107	231.5	52950.477	0.467 ± 0.151	15.63 ± 21.7	2.00 ± 0.05	...	0.08 ± 0.01	6.40 ± 0.55	0.06 ± 0.02	331	1.03	H
169	1108	232.4	52951.425	0.646 ± 0.099	6.04 ± 2.77	1.94 ± 0.06	...	0.06 ± 0.01	6.40 ± 0.32	0.10 ± 0.02	645	1.04	H
170	1109	233.3	52952.276	< 0.441	(25.0)	2.14 ± 0.02	...	0.08 ± 0.01	6.50 ± 0.59	0.05 ± 0.01	337	1.35	H:SPL ^q

^aNumber of days since discovery on 2003 March 21 = MJD 52719 (Revnivtsev et al. 2003).^bStart of observation. MJD = JD - 2,400,000.5.^c $R_{\text{in}}^* = R_{\text{in}}(\cos \theta)^{1/2}/(D/10 \text{ kpc})$, where θ is the inclination angle and D is the distance to the source in kpc.

^d3–15 keV index for day number < 102; 3–200 keV photon index for day number > 102.

^e15–200 keV photon index (day number < 102).

^fPhotons s⁻¹ cm⁻² keV⁻¹ at 1 keV.

^gGaussian with fixed FWHM = 1.2 keV.

^hPhotons s⁻¹ cm⁻².

ⁱEquivalent width of the Fe K line in eV.

^jUnless otherwise indicated in these table notes, the number of degrees of freedom (dof) if the fit includes(excludes) a Gaussian emission line is 86(88) for day numbers < 102 and 88(90) for day numbers > 102.

^kSee Table 1 and §3 for definitions of X-ray states.

^lModel components include broken power law and a Gaussian emission line and exclude a thermal component (dof = 88). The break energy is 25.0 keV for Obs. No. 1, and is 15.0 keV otherwise. Upper limits are at the 99% level of confidence and were calculated for an assumed value of $R_{\text{in}} = 25$ km.

^mFitted using data from HEXTE Cluster 0 because data from Cluster 1 saturated the telemetry.

ⁿHEXTE fitting range restricted to $E = 39.1 - 200$ keV (includes HEXTE-A channels 20-56; 81 dof).

^oHEXTE fitting range restricted to $E = 29.1 - 200$ keV (includes HEXTE-A channels 15-56; 86 dof).

^pPPCA fitting range restricted to $E = 2.8 - 22.4$ keV (includes PCU-2 channels 4-49; 86 dof).

^qModel components include a simple power law and a Gaussian emission line and exclude a thermal component (dof = 90). Upper limits are at the 99% level of confidence and were calculated for an assumed value of $R_{\text{in}} = 25$ km.

Table A3. Unabsorbed Flux Data^a and QPO Data for H1743-322

Obs. No.	Day ^b	MJD ^c	Obs. Time (s)	Total 2-20 keV (10 ⁻⁸ cgs)	Disk 2-20 keV (10 ⁻⁸ cgs)	Power Law 2-20 keV (10 ⁻⁸ cgs)	Fe Line (10 ⁻¹⁰ cgs)	2-20 keV Disk/Total	Power Law 20-100 keV (10 ⁻⁹ cgs)	QPO ν^d (Hz)	QPO Amplitude ^e (% rms)	QPO Q^f	Cont. r^g (rms)
1	7.8	52726.850	3472	0.160 ^{+0.001} _{-0.001}	< 0.001	0.160 ^{+0.001} _{-0.001}	0.079 ^{+0.017} _{-0.020}	< 0.006	2.410 ^{+0.022} _{-0.029} ^h	0.063	3.63 ± 0.45	31.5	0.242
2	10.8	52729.809	3488	0.392 ^{+0.001} _{-0.002}	< 0.001	0.392 ^{+0.001} _{-0.001}	0.385 ^{+0.038} _{-0.049}	< 0.003	3.092 ^{+0.030} _{-0.034} ^{h,i}	0.159 ^j	13.72 ± 0.58	3.8	0.262
3	14.8	52733.762	3472	0.832 ^{+0.005} _{-0.005}	0.052 ^{+0.001} _{-0.006}	0.779 ^{+0.001} _{-0.001}	1.408 ^{+0.086} _{-0.088}	0.062 ^{+0.002} _{-0.008}	2.106 ^{+0.034} _{-0.034}	2.23 ^k	12.53 ± 0.23	11.7	0.206
4	16.7	52735.734	3488	1.070 ^{+0.004} _{-0.004}	0.219 ^{+0.003} _{-0.003}	0.851 ^{+0.002} _{-0.002}	...	0.205 ^{+0.004} _{-0.004}	1.848 ^{+0.034} _{-0.034}	3.75 ^k	12.32 ± 0.20	11.4	0.173
5	18.6	52737.580	3568	1.556 ^{+0.003} _{-0.006}	0.055 ^{+0.001} _{-0.002}	1.500 ^{+0.002} _{-0.002}	2.277 ^{+0.105} _{-0.148}	0.035 ^{+0.001} _{-0.002}	3.277 ^{+0.022} _{-0.026}	2.08 ^k	12.23 ± 0.27	11.6	0.197
6	20.7	52739.678	3616	1.745 ^{+0.004} _{-0.007}	0.122 ^{+0.001} _{-0.007}	1.622 ^{+0.002} _{-0.003}	2.281 ^{+0.105} _{-0.179}	0.070 ^{+0.001} _{-0.004}	2.537 ^{+0.027} _{-0.026}	3.23 ^j	12.22 ± 0.18	10.4	0.177
7	22.8	52741.854	3024	1.698 ^{+0.003} _{-0.006}	0.376 ^{+0.002} _{-0.004}	1.320 ^{+0.002} _{-0.003}	0.844 ^{+0.158} _{-0.179}	0.221 ^{+0.002} _{-0.003}	1.823 ^{+0.023} _{-0.029}	7.22	6.10 ± 0.07	6.9	0.122
8	24.2	52743.240	2672	2.786 ^{+0.005} _{-0.011}	0.747 ^{+0.004} _{-0.005}	2.039 ^{+0.005} _{-0.005}	...	0.268 ^{+0.002} _{-0.003}	2.750 ^{+0.027} _{-0.031}	8.53	4.30 ± 0.06	15.5	0.112
9	25.2	52744.220	3024	2.238 ^{+0.004} _{-0.007}	0.351 ^{+0.003} _{-0.004}	1.885 ^{+0.003} _{-0.003}	1.035 ^{+0.179} _{-0.200}	0.157 ^{+0.002} _{-0.003}	2.352 ^{+0.025} _{-0.028}	5.63	9.02 ± 0.09	6.8	0.137
10	27.2	52746.195	2880	0.998 ^{+0.002} _{-0.004}	0.234 ^{+0.002} _{-0.002}	0.763 ^{+0.002} _{-0.002}	0.601 ^{+0.097} _{-0.097}	0.234 ^{+0.003} _{-0.003}	1.262 ^{+0.017} _{-0.021}	4.74 ^j	10.78 ± 0.15	8.8	0.151
11	28.6	52747.633	3232	1.493 ^{+0.003} _{-0.006}	0.314 ^{+0.002} _{-0.002}	1.178 ^{+0.002} _{-0.003}	0.498 ^{+0.142} _{-0.110}	0.210 ^{+0.002} _{-0.003}	1.582 ^{+0.020} _{-0.034}	7.07	6.12 ± 0.07	6.5	0.118
12	31.3	52750.313	5888	3.175 ^{+0.007} _{-0.013}	1.024 ^{+0.005} _{-0.005}	2.151 ^{+0.005} _{-0.006}	...	0.323 ^{+0.002} _{-0.003}	3.404 ^{+0.011} _{-0.034}	13.30	0.83 ± 0.07	5.6	0.050
13	31.8	52750.810	15456	2.900 ^{+0.007} _{-0.010}	0.914 ^{+0.005} _{-0.005}	1.986 ^{+0.004} _{-0.006}	...	0.315 ^{+0.004} _{-0.003}	2.902 ^{+0.009} _{-0.023}	9.78	1.88 ± 0.03	9.3	0.101
14	32.1	52751.089	6832	2.328 ^{+0.005} _{-0.010}	0.858 ^{+0.004} _{-0.004}	1.470 ^{+0.004} _{-0.004}	...	0.369 ^{+0.004} _{-0.003}	2.251 ^{+0.009} _{-0.027}	5.24 ^j	1.75 ± 0.04	8.7	0.101
15	32.3	52751.316	5376	4.825 ^{+0.007} _{-0.016}	1.482 ^{+0.007} _{-0.011}	3.343 ^{+0.006} _{-0.008}	...	0.307 ^{+0.002} _{-0.003}	3.978 ^{+0.017} _{-0.025}	9.71	1.31 ± 0.04	12.1	0.085
16	32.7	52751.714	3280	2.512 ^{+0.006} _{-0.011}	0.979 ^{+0.004} _{-0.004}	1.533 ^{+0.004} _{-0.004}	...	0.390 ^{+0.004} _{-0.006}	2.072 ^{+0.026} _{-0.033} ^m	5.73 ^k	4.32 ± 0.07	3.5	0.104
17	33.0	52751.987	3696	2.412 ^{+0.005} _{-0.008}	1.077 ^{+0.004} _{-0.005}	1.335 ^{+0.004} _{-0.004}	...	0.447 ^{+0.003} _{-0.004}	1.673 ^{+0.019} _{-0.033}	5.97	4.98 ± 0.05	3.0	0.089
18	34.0	52752.972	10752	3.152 ^{+0.006} _{-0.013}	0.988 ^{+0.005} _{-0.006}	2.164 ^{+0.004} _{-0.006}	...	0.313 ^{+0.002} _{-0.003}	3.316 ^{+0.014} _{-0.023}	9.78 ⁿ	1.11 ± 0.04	10.9	0.077
19	34.2	52753.167	2944	3.107 ^{+0.007} _{-0.014}	0.918 ^{+0.005} _{-0.005}	2.189 ^{+0.004} _{-0.004}	...	0.295 ^{+0.002} _{-0.003}	3.486 ^{+0.027} _{-0.035}	11.74	0.74 ± 0.11	47.0	0.048
20	35.6	52754.575	3472	2.468 ^{+0.005} _{-0.008}	0.911 ^{+0.004} _{-0.004}	1.557 ^{+0.005} _{-0.004}	...	0.369 ^{+0.002} _{-0.003}	2.297 ^{+0.026} _{-0.034}	9.90 ^o	2.08 ± 0.05	9.7	0.117
21	37.0	52755.960	3664	3.784 ^{+0.007} _{-0.014}	2.207 ^{+0.009} _{-0.007}	1.577 ^{+0.006} _{-0.005}	...	0.583 ^{+0.004} _{-0.004}	1.267 ^{+0.013} _{-0.019} ^p	7.76 ^q	2.62 ± 0.04	2.5	0.073
22	37.2	52756.219	2224	3.302 ^{+0.006} _{-0.011}	1.895 ^{+0.006} _{-0.008}	1.407 ^{+0.004} _{-0.005}	...	0.574 ^{+0.003} _{-0.005}	1.229 ^{+0.021} _{-0.026}	5.96 ^r	3.61 ± 0.08	1.3	0.069
23	37.7	52756.714	3136	1.775 ^{+0.003} _{-0.008}	0.956 ^{+0.002} _{-0.004}	0.819 ^{+0.002} _{-0.003}	...	0.539 ^{+0.002} _{-0.005}	0.883 ^{+0.045} _{-0.041}	4.96 ^j	2.68 ± 0.07	4.0	0.074
24	38.8	52757.803	6976	1.581 ^{+0.002} _{-0.006}	1.262 ^{+0.003} _{-0.003}	0.319 ^{+0.002} _{-0.002}	...	0.798 ^{+0.003} _{-0.005}	0.735 ^{+0.009} _{-0.039}	0.070
25	40.0	52758.996	3472	2.956 ^{+0.005} _{-0.011}	2.481 ^{+0.007} _{-0.007}	0.475 ^{+0.004} _{-0.004}	...	0.839 ^{+0.004} _{-0.006}	0.203 ^{+0.008} _{-0.014}	0.055
26	41.1	52760.081	3488	1.598 ^{+0.003} _{-0.007}	1.300 ^{+0.003} _{-0.004}	0.298 ^{+0.002} _{-0.001}	...	0.814 ^{+0.004} _{-0.006}	0.850 ^{+0.010} _{-0.053}	0.063
27	41.6	52760.558	3696	1.647 ^{+0.003} _{-0.006}	1.301 ^{+0.003} _{-0.004}	0.345 ^{+0.002} _{-0.002}	0.412 ^{+0.079} _{-0.093}	0.790 ^{+0.004} _{-0.006}	0.801 ^{+0.018} _{-0.041}	0.071
28	41.8	52760.854	16096	2.339 ^{+0.004} _{-0.008}	1.933 ^{+0.004} _{-0.004}	0.406 ^{+0.003} _{-0.004}	...	0.826 ^{+0.003} _{-0.006}	0.991 ^{+0.072} _{-0.019}	0.066
29	42.0	52761.039	4256	2.432 ^{+0.004} _{-0.011}	1.992 ^{+0.005} _{-0.005}	0.440 ^{+0.003} _{-0.004}	...	0.819 ^{+0.004} _{-0.007}	0.623 ^{+0.019} _{-0.039}	0.060
30	42.6	52761.612	5184	2.402 ^{+0.005} _{-0.010}	1.947 ^{+0.004} _{-0.006}	0.455 ^{+0.002} _{-0.003}	...	0.811 ^{+0.004} _{-0.006}	1.143 ^{+0.015} _{-0.035}	0.066
31	43.7	52762.746	6528	2.448 ^{+0.003} _{-0.010}	1.882 ^{+0.004} _{-0.005}	0.566 ^{+0.003} _{-0.004}	...	0.769 ^{+0.003} _{-0.005}	1.784 ^{+0.012} _{-0.038}	0.067
32	44.1	52763.095	3408	2.828 ^{+0.004} _{-0.010}	1.868 ^{+0.005} _{-0.004}	0.960 ^{+0.005} _{-0.004}	...	0.661 ^{+0.003} _{-0.004}	1.434 ^{+0.019} _{-0.031}	7.82 ^s	2.75 ± 0.05	2.5	0.059
33	44.6	52763.617	2736	3.152 ^{+0.005} _{-0.012}	1.658 ^{+0.006} _{-0.005}	1.494 ^{+0.004} _{-0.007}	...	0.526 ^{+0.003} _{-0.004}	1.837 ^{+0.039} _{-0.038}	5.43 ^j	3.78 ± 0.05	2.5	0.061
34	45.9	52764.907	6752	3.188 ^{+0.005} _{-0.013}	1.665 ^{+0.007} _{-0.007}	1.523 ^{+0.004} _{-0.004}	...	0.522 ^{+0.003} _{-0.004}	1.893 ^{+0.014} _{-0.027}	5.46 ^j	3.79 ± 0.03	2.9	0.062
35	46.9	52765.867	3408	5.152 ^{+0.009} _{-0.022}	1.280 ^{+0.008} _{-0.010}	3.872 ^{+0.007} _{-0.010}	...	0.248 ^{+0.002} _{-0.002}	6.854 ^{+0.028} _{-0.040}	11.16	1.21 ± 0.05	4.2	0.047

Table A3—Continued

Obs. No.	Day ^b	MJD ^c	Obs. Time (s)	Total 2-20 keV (10 ⁻⁸ cgs)	Disk 2-20 keV (10 ⁻⁸ cgs)	Power Law 2-20 keV (10 ⁻⁸ cgs)	Fe Line 2-20 keV (10 ⁻¹⁰ cgs)	Disk/Total	Power Law 20-100 keV (10 ⁻⁹ cgs)	QPO ν^d (Hz)	QPO Amplitude ^e (% rms)	QPO Q^f	Cont. r^g (rms)
				2-20 keV (10 ⁻⁸ cgs)	2-20 keV (10 ⁻⁸ cgs)	2-20 keV (10 ⁻⁸ cgs)	(10 ⁻¹⁰ cgs)	Disk/Total	(10 ⁻⁹ cgs)	(Hz)	(% rms)	(rms)	
36	47.6	52766.575	2544	2.299 ^{+0.004} _{-0.007}	0.435 ^{+0.003} _{-0.006}	1.862 ^{+0.003} _{-0.004}	2.146 ^{+0.190} _{-0.158}	0.189 ^{+0.002} _{-0.004}	2.725 ^{+0.041} _{-0.069}	5.62 ^m	9.20 ± 0.11	3.0	0.143
37	48.9	52767.865	6784	1.855 ^{+0.002} _{-0.006}	0.318 ^{+0.003} _{-0.005}	1.536 ^{+0.002} _{-0.002}	2.416 ^{+0.095} _{-0.137}	0.171 ^{+0.002} _{-0.004}	2.346 ^{+0.021} _{-0.018}	4.43 ^j	11.42 ± 0.10	9.0	0.159
38	49.5	52768.547	2160	1.892 ^{+0.003} _{-0.005}	0.362 ^{+0.003} _{-0.004}	1.528 ^{+0.003} _{-0.003}	1.212 ^{+0.158} _{-0.179}	0.191 ^{+0.002} _{-0.003}	2.243 ^{+0.026} _{-0.029}	5.39 ^m	10.07 ± 0.14	7.6	0.149
39	50.7	52769.746	2432	1.773 ^{+0.002} _{-0.007}	0.332 ^{+0.002} _{-0.004}	1.440 ^{+0.002} _{-0.003}	1.617 ^{+0.116} _{-0.137}	0.187 ^{+0.002} _{-0.003}	2.254 ^{+0.019} _{-0.037}	4.91 ^j	10.78 ± 0.14	10.0	0.159
40	51.5	52770.535	3728	2.209 ^{+0.003} _{-0.007}	0.412 ^{+0.003} _{-0.004}	1.796 ^{+0.003} _{-0.003}	1.614 ^{+0.158} _{-0.137}	0.187 ^{+0.002} _{-0.003}	2.509 ^{+0.033} _{-0.043}	6.16	8.34 ± 0.08	7.3	0.140
41	52.9	52771.868	7680	1.500 ^{+0.003} _{-0.008}	0.157 ^{+0.001} _{-0.005}	1.342 ^{+0.002} _{-0.002}	2.286 ^{+0.095} _{-0.095}	0.105 ^{+0.001} _{-0.004}	2.746 ^{+0.017} _{-0.022}	2.76 ^k	12.01 ± 0.14	8.6	0.192
42	53.7	52772.739	6080	1.368 ^{+0.003} _{-0.009}	0.079 ^{+0.001} _{-0.007}	1.288 ^{+0.002} _{-0.002}	2.331 ^{+0.084} _{-0.137}	0.058 ^{+0.001} _{-0.006}	3.397 ^{+0.021} _{-0.022}	1.84 ^k	12.87 ± 0.17	9.2	0.214
43	54.7	52773.725	6768	1.358 ^{+0.004} _{-0.010}	0.069 ^{+0.002} _{-0.009}	1.288 ^{+0.002} _{-0.002}	2.172 ^{+0.116} _{-0.148}	0.051 ^{+0.002} _{-0.018}	3.270 ^{+0.020} _{-0.021}	1.91 ^k	12.71 ± 0.17	9.6	0.212
44	55.6	52774.582	6656	1.447 ^{+0.002} _{-0.005}	0.173 ^{+0.001} _{-0.004}	1.273 ^{+0.002} _{-0.002}	2.172 ^{+0.126} _{-0.116}	0.120 ^{+0.001} _{-0.003}	2.652 ^{+0.015} _{-0.025}	3.16 ^k	12.51 ± 0.14	6.6	0.194
45	56.6	52775.634	6704	1.299 ^{+0.003} _{-0.006}	0.101 ^{+0.001} _{-0.004}	1.197 ^{+0.002} _{-0.002}	2.181 ^{+0.105} _{-0.126}	0.078 ^{+0.001} _{-0.004}	3.017 ^{+0.019} _{-0.021}	2.15 ^k	13.07 ± 0.17	9.8	0.212
46	57.7	52776.684	6592	0.966 ^{+0.003} _{-0.003}	< 0.003	0.965 ^{+0.001} _{-0.002}	0.665 ^{+0.080} _{-0.098}	< 0.004	3.083 ^{+0.014} _{-0.014}	1.72 ^k	13.56 ± 0.18	7.5	0.227
47	58.7	52777.667	6576	1.351 ^{+0.003} _{-0.008}	0.120 ^{+0.001} _{-0.006}	1.230 ^{+0.003} _{-0.002}	2.275 ^{+0.095} _{-0.137}	0.089 ^{+0.001} _{-0.005}	2.863 ^{+0.015} _{-0.021}	2.51 ^k	12.91 ± 0.16	10.5	0.207
48	59.5	52778.526	6544	1.420 ^{+0.002} _{-0.006}	0.173 ^{+0.001} _{-0.004}	1.246 ^{+0.003} _{-0.002}	2.137 ^{+0.116} _{-0.137}	0.122 ^{+0.001} _{-0.004}	2.585 ^{+0.012} _{-0.014}	3.24 ^k	12.94 ± 0.14	8.8	0.192
49	60.6	52779.584	4848	1.513 ^{+0.003} _{-0.006}	0.225 ^{+0.001} _{-0.003}	1.287 ^{+0.002} _{-0.002}	1.935 ^{+0.116} _{-0.126}	0.149 ^{+0.001} _{-0.003}	2.328 ^{+0.018} _{-0.023}	3.82 ^k	12.58 ± 0.15	11.2	0.187
50	61.6	52780.598	3376	1.531 ^{+0.002} _{-0.006}	0.231 ^{+0.001} _{-0.004}	1.299 ^{+0.002} _{-0.003}	2.056 ^{+0.116} _{-0.148}	0.151 ^{+0.001} _{-0.003}	2.434 ^{+0.028} _{-0.027}	3.83 ^k	12.49 ± 0.18	11.3	0.184
51	62.6	52781.616	6816	1.490 ^{+0.002} _{-0.006}	0.207 ^{+0.002} _{-0.004}	1.282 ^{+0.003} _{-0.002}	2.016 ^{+0.137} _{-0.137}	0.139 ^{+0.002} _{-0.004}	2.457 ^{+0.016} _{-0.024}	3.64 ^k	12.88 ± 0.13	9.3	0.191
52	63.7	52782.697	3232	1.557 ^{+0.001} _{-0.005}	0.322 ^{+0.002} _{-0.003}	1.234 ^{+0.002} _{-0.002}	1.546 ^{+0.137} _{-0.084}	0.207 ^{+0.002} _{-0.003}	2.237 ^{+0.021} _{-0.027}	4.70 ^k	11.50 ± 0.15	11.2	0.173
53	64.5	52783.510	6512	2.058 ^{+0.004} _{-0.008}	0.488 ^{+0.003} _{-0.005}	1.568 ^{+0.002} _{-0.003}	1.126 ^{+0.211} _{-0.158}	0.237 ^{+0.002} _{-0.004}	2.513 ^{+0.016} _{-0.025}	7.08	6.37 ± 0.05	6.1	0.129
54	65.6	52784.568	6688	2.951 ^{+0.004} _{-0.011}	1.389 ^{+0.006} _{-0.004}	1.562 ^{+0.004} _{-0.004}	...	0.471 ^{+0.003} _{-0.003}	2.550 ^{+0.014} _{-0.025}	5.72	5.92 ± 0.04	2.1	0.078
55	66.5	52785.483	6720	3.069 ^{+0.005} _{-0.010}	1.383 ^{+0.005} _{-0.007}	1.686 ^{+0.004} _{-0.005}	...	0.451 ^{+0.003} _{-0.004}	2.725 ^{+0.016} _{-0.033}	5.66 ^t	6.07 ± 0.03	1.8	0.083
56	67.3	52786.350	6448	3.544 ^{+0.007} _{-0.012}	1.157 ^{+0.006} _{-0.004}	2.387 ^{+0.005} _{-0.006}	...	0.326 ^{+0.002} _{-0.002}	3.915 ^{+0.014} _{-0.041}	9.42	2.06 ± 0.04	11.5	0.067
57	67.8	52786.846	2224	3.050 ^{+0.005} _{-0.013}	1.263 ^{+0.006} _{-0.007}	1.787 ^{+0.004} _{-0.005}	...	0.414 ^{+0.003} _{-0.004}	2.827 ^{+0.029} _{-0.044}	5.48 ^j	6.01 ± 0.07	1.8	0.089
58	68.0	52787.044	1504	2.866 ^{+0.004} _{-0.013}	1.486 ^{+0.004} _{-0.006}	1.380 ^{+0.004} _{-0.005}	...	0.518 ^{+0.002} _{-0.002}	2.148 ^{+0.027} _{-0.054}	5.54	4.83 ± 0.08	3.3	0.067
59	68.2	52787.237	1456	2.567 ^{+0.003} _{-0.011}	1.486 ^{+0.005} _{-0.005}	1.081 ^{+0.004} _{-0.005}	...	0.579 ^{+0.003} _{-0.005}	1.689 ^{+0.037} _{-0.042}	4.78 ^u	2.90 ± 0.06	6.6	0.055
60	68.5	52787.492	22496	2.922 ^{+0.004} _{-0.009}	1.501 ^{+0.005} _{-0.006}	1.421 ^{+0.004} _{-0.003}	...	0.514 ^{+0.003} _{-0.004}	2.275 ^{+0.009} _{-0.020}	5.68 ^v	5.33 ± 0.02	2.5	0.068
61	69.0	52788.025	1728	3.003 ^{+0.004} _{-0.012}	1.346 ^{+0.005} _{-0.005}	1.657 ^{+0.003} _{-0.005}	...	0.448 ^{+0.003} _{-0.003}	2.750 ^{+0.040} _{-0.047}	5.74	5.67 ± 0.07	2.2	0.078
62	69.5	52788.506	7104	2.318 ^{+0.003} _{-0.008}	1.497 ^{+0.005} _{-0.004}	0.820 ^{+0.002} _{-0.004}	0.568 ^{+0.115} _{-0.105}	0.646 ^{+0.003} _{-0.004}	1.352 ^{+0.011} _{-0.024}	8.74 ^w	2.71 ± 0.04	3.8	0.056
63	69.9	52788.878	2192	2.536 ^{+0.003} _{-0.010}	1.952 ^{+0.006} _{-0.006}	0.582 ^{+0.003} _{-0.004}	1.052 ^{+0.179} _{-0.126}	0.770 ^{+0.004} _{-0.005}	1.940 ^{+0.022} _{-0.108}	0.044
64	70.3	52789.264	3488	2.736 ^{+0.004} _{-0.011}	1.552 ^{+0.006} _{-0.006}	1.184 ^{+0.004} _{-0.004}	...	0.567 ^{+0.003} _{-0.004}	1.899 ^{+0.024} _{-0.027}	5.22 ^x	3.93 ± 0.05	4.4	0.057
65	70.9	52789.930	2112	2.636 ^{+0.005} _{-0.012}	1.432 ^{+0.005} _{-0.005}	1.204 ^{+0.004} _{-0.004}	...	0.543 ^{+0.003} _{-0.004}	1.958 ^{+0.040} _{-0.040}	5.36 ^j	4.32 ± 0.06	3.3	0.057
66	71.1	52790.129	3056	2.494 ^{+0.004} _{-0.010}	1.348 ^{+0.004} _{-0.005}	1.145 ^{+0.004} _{-0.004}	0.623 ^{+0.137} _{-0.179}	0.540 ^{+0.003} _{-0.004}	1.842 ^{+0.019} _{-0.032}	5.52 ^j	4.53 ± 0.06	2.7	0.064
67	71.2	52790.236	3984	2.555 ^{+0.005} _{-0.011}	1.500 ^{+0.004} _{-0.005}	1.055 ^{+0.004} _{-0.004}	...	0.587 ^{+0.003} _{-0.005}	1.755 ^{+0.019} _{-0.032}	5.03 ^x	3.52 ± 0.05	4.3	0.055
68	71.9	52790.916	2192	2.429 ^{+0.003} _{-0.009}	1.762 ^{+0.004} _{-0.005}	0.666 ^{+0.003} _{-0.003}	0.634 ^{+0.105} _{-0.147}	0.725 ^{+0.003} _{-0.005}	1.631 ^{+0.032} _{-0.054}	7.24	1.63 ± 0.14	2.3	0.047
69	72.6	52791.632	5792	2.482 ^{+0.004} _{-0.010}	1.503 ^{+0.005} _{-0.006}	0.978 ^{+0.003} _{-0.004}	0.532 ^{+0.126} _{-0.104}	0.606 ^{+0.003} _{-0.005}	1.649 ^{+0.019} _{-0.041}	4.91 ^x	3.18 ± 0.04	4.9	0.061
70	73.0	52792.036	1936	2.228 ^{+0.003} _{-0.010}	1.523 ^{+0.004} _{-0.006}	0.704 ^{+0.003} _{-0.004}	0.504 ^{+0.105} _{-0.136}	0.684 ^{+0.003} _{-0.006}	1.325 ^{+0.034} _{-0.041}	7.15	2.72 ± 0.09	2.3	0.047

Table A3—Continued

Obs. No.	Day ^b	MJD ^c	Obs. Time (s)	Total 2-20 keV (10 ⁻⁸ cgs)	Disk 2-20 keV (10 ⁻⁸ cgs)	Power Law 2-20 keV (10 ⁻⁸ cgs)	Fe Line (10 ⁻¹⁰ cgs)	2-20 keV Disk/Total	Power Law 20-100 keV (10 ⁻⁹ cgs)	QPO ν^d (Hz)	QPO Amplitude ^e (% rms)	QPO Q^f	Cont. r^g (rms)
71	73.4	52792.390	6752	2.529 ^{+0.004} _{-0.011}	1.399 ^{+0.004} _{-0.005}	1.130 ^{+0.004} _{-0.004}	...	0.553 ^{+0.003} _{-0.004}	1.817 ^{+0.013} _{-0.029}	5.22 ^j	4.08 ± 0.04	3.9	0.056
72	74.0	52793.024	1856	2.161 ^{+0.003} _{-0.011}	1.469 ^{+0.004} _{-0.005}	0.692 ^{+0.003} _{-0.002}	...	0.680 ^{+0.003} _{-0.006}	1.266 ^{+0.029} _{-0.044}	5.22	2.72 ± 0.09	2.8	0.046
73	74.6	52793.607	3136	2.578 ^{+0.003} _{-0.010}	1.525 ^{+0.007} _{-0.005}	1.052 ^{+0.003} _{-0.004}	0.542 ^{+0.147} _{-0.147}	0.592 ^{+0.004} _{-0.004}	1.714 ^{+0.022} _{-0.038}	4.83 ^x	3.69 ± 0.06	4.9	0.052
74	75.6	52794.559	7280	3.564 ^{+0.005} _{-0.015}	1.167 ^{+0.006} _{-0.006}	2.397 ^{+0.004} _{-0.005}	...	0.327 ^{+0.002} _{-0.003}	4.335 ^{+0.017} _{-0.035}	10.28 ^y	1.28 ± 0.05	3.3	0.030
75	76.4	52795.381	3712	2.310 ^{+0.004} _{-0.009}	1.482 ^{+0.005} _{-0.007}	0.827 ^{+0.004} _{-0.003}	0.631 ^{+0.084} _{-0.115}	0.642 ^{+0.004} _{-0.006}	1.439 ^{+0.023} _{-0.039}	8.15 ^y	2.79 ± 0.07	2.6	0.050
76	77.3	52796.265	7024	2.580 ^{+0.004} _{-0.010}	1.403 ^{+0.004} _{-0.005}	1.177 ^{+0.004} _{-0.004}	...	0.544 ^{+0.003} _{-0.004}	1.952 ^{+0.012} _{-0.021}	5.42 ^j	4.89 ± 0.04	2.8	0.060
77	78.6	52797.583	7120	2.604 ^{+0.005} _{-0.010}	1.309 ^{+0.004} _{-0.005}	1.295 ^{+0.003} _{-0.005}	0.785 ^{+0.005} _{-0.004}	0.503 ^{+0.003} _{-0.004}	2.168 ^{+0.022} _{-0.035}	5.58 ^m	5.32 ± 0.03	2.6	0.066
78	79.5	52798.535	3296	3.688 ^{+0.005} _{-0.015}	1.122 ^{+0.006} _{-0.006}	2.566 ^{+0.006} _{-0.006}	...	0.304 ^{+0.002} _{-0.003}	4.866 ^{+0.025} _{-0.042}	9.58	1.22 ± 0.09	5.7	0.029
79	80.5	52799.455	2976	2.279 ^{+0.003} _{-0.008}	1.423 ^{+0.003} _{-0.005}	0.855 ^{+0.003} _{-0.004}	0.610 ^{+0.094} _{-0.126}	0.624 ^{+0.003} _{-0.005}	1.475 ^{+0.019} _{-0.044}	4.60 ^x	2.96 ± 0.05	4.3	0.048
80	81.7	52800.732	11568	2.214 ^{+0.004} _{-0.007}	1.642 ^{+0.003} _{-0.005}	0.571 ^{+0.003} _{-0.002}	0.625 ^{+0.084} _{-0.084}	0.742 ^{+0.003} _{-0.005}	1.640 ^{+0.010} _{-0.035}	8.60 ^y	1.47 ± 0.05	2.8	0.035
81	82.9	52801.915	4832	2.343 ^{+0.004} _{-0.009}	1.403 ^{+0.003} _{-0.006}	0.940 ^{+0.003} _{-0.003}	...	0.599 ^{+0.003} _{-0.005}	1.615 ^{+0.013} _{-0.028}	4.92 ^j	4.07 ± 0.04	4.9	0.055
82	84.0	52802.963	4544	2.338 ^{+0.003} _{-0.009}	1.322 ^{+0.004} _{-0.005}	1.015 ^{+0.004} _{-0.003}	0.731 ^{+0.136} _{-0.126}	0.565 ^{+0.003} _{-0.004}	1.780 ^{+0.016} _{-0.029}	5.29 ^j	4.59 ± 0.05	3.8	0.057
83	84.6	52803.568	6304	2.245 ^{+0.008} _{-0.006}	1.255 ^{+0.003} _{-0.006}	0.989 ^{+0.003} _{-0.004}	0.467 ^{+0.126} _{-0.145}	0.559 ^{+0.003} _{-0.005}	1.818 ^{+0.014} _{-0.028}	5.26 ^j	4.00 ± 0.04	4.5	0.058
84	85.6	52804.623	6768	2.335 ^{+0.002} _{-0.007}	1.132 ^{+0.004} _{-0.004}	1.202 ^{+0.003} _{-0.004}	0.784 ^{+0.137} _{-0.157}	0.485 ^{+0.003} _{-0.003}	2.257 ^{+0.017} _{-0.029}	5.62 ^m	5.54 ± 0.04	1.8	0.069
85	86.5	52805.472	4992	2.305 ^{+0.004} _{-0.008}	1.187 ^{+0.003} _{-0.005}	1.117 ^{+0.003} _{-0.005}	0.912 ^{+0.147} _{-0.094}	0.515 ^{+0.002} _{-0.004}	1.969 ^{+0.021} _{-0.036}	5.53 ^m	5.38 ± 0.04	2.6	0.063
86	87.6	52806.627	3312	1.990 ^{+0.003} _{-0.008}	1.517 ^{+0.004} _{-0.004}	0.472 ^{+0.002} _{-0.003}	0.923 ^{+0.094} _{-0.094}	0.762 ^{+0.003} _{-0.005}	1.643 ^{+0.017} _{-0.042}	0.032
87	88.6	52807.619	2416	1.997 ^{+0.004} _{-0.009}	1.640 ^{+0.004} _{-0.005}	0.356 ^{+0.002} _{-0.002}	0.677 ^{+0.073} _{-0.052}	0.821 ^{+0.004} _{-0.005}	1.459 ^{+0.048} _{-0.081}	0.033
88	89.6	52808.636	5824	1.920 ^{+0.003} _{-0.006}	1.582 ^{+0.004} _{-0.004}	0.337 ^{+0.002} _{-0.002}	0.722 ^{+0.084} _{-0.063}	0.824 ^{+0.004} _{-0.005}	1.388 ^{+0.076} _{-0.042}	0.032
89	90.6	52809.620	5184	1.861 ^{+0.003} _{-0.008}	1.563 ^{+0.004} _{-0.004}	0.297 ^{+0.002} _{-0.002}	0.631 ^{+0.073} _{-0.073}	0.840 ^{+0.004} _{-0.006}	1.139 ^{+0.015} _{-0.037}	0.033
90	91.5	52810.540	5728	1.695 ^{+0.002} _{-0.007}	1.544 ^{+0.003} _{-0.003}	0.150 ^{+0.001} _{-0.003}	0.357 ^{+0.070} _{-0.061}	0.911 ^{+0.003} _{-0.007}	0.545 ^{+0.010} _{-0.050}	0.033
91	92.5	52811.461	4192	1.719 ^{+0.002} _{-0.008}	1.472 ^{+0.003} _{-0.003}	0.246 ^{+0.002} _{-0.002}	0.662 ^{+0.066} _{-0.065}	0.856 ^{+0.003} _{-0.007}	1.110 ^{+0.018} _{-0.042}	0.035
92	93.7	52812.667	4832	1.685 ^{+0.003} _{-0.007}	1.445 ^{+0.003} _{-0.004}	0.239 ^{+0.001} _{-0.002}	0.597 ^{+0.068} _{-0.073}	0.858 ^{+0.004} _{-0.007}	0.939 ^{+0.011} _{-0.040}	0.038
93	94.8	52813.828	13488	1.660 ^{+0.003} _{-0.007}	1.486 ^{+0.003} _{-0.004}	0.174 ^{+0.001} _{-0.002}	0.422 ^{+0.041} _{-0.058}	0.895 ^{+0.004} _{-0.007}	0.732 ^{+0.030} _{-0.029}	14.74	0.87 ± 0.10	7.9	0.030
94	95.5	52814.475	3904	1.667 ^{+0.002} _{-0.007}	1.514 ^{+0.004} _{-0.004}	0.152 ^{+0.001} _{-0.002}	0.532 ^{+0.072} _{-0.058}	0.908 ^{+0.004} _{-0.007}	0.711 ^{+0.016} _{-0.052}	0.027
95	96.8	52815.836	3264	1.527 ^{+0.003} _{-0.004}	1.423 ^{+0.004} _{-0.002}	0.103 ^{+0.001} _{-0.001}	0.442 ^{+0.065} _{-0.063}	0.932 ^{+0.005} _{-0.005}	0.343 ^{+0.012} _{-0.081}	0.030
96	97.6	52816.581	4816	1.476 ^{+0.003} _{-0.005}	1.389 ^{+0.003} _{-0.003}	0.087 ^{+0.001} _{-0.001}	...	0.941 ^{+0.005} _{-0.006}	0.308 ^{+0.013} _{-0.031}	0.030
97	98.5	52817.509	5696	1.526 ^{+0.003} _{-0.005}	1.420 ^{+0.004} _{-0.002}	0.105 ^{+0.001} _{-0.001}	0.305 ^{+0.063} _{-0.057}	0.931 ^{+0.005} _{-0.005}	0.369 ^{+0.013} _{-0.030}	0.029
98	99.5	52818.548	4624	1.505 ^{+0.002} _{-0.006}	1.427 ^{+0.004} _{-0.003}	0.078 ^{+0.001} _{-0.001}	...	0.948 ^{+0.005} _{-0.007}	0.239 ^{+0.012} _{-0.036}	0.028
99	100.3	52819.343	2688	1.479 ^{+0.003} _{-0.005}	1.384 ^{+0.003} _{-0.004}	0.094 ^{+0.001} _{-0.001}	0.346 ^{+0.068} _{-0.061}	0.936 ^{+0.005} _{-0.007}	0.306 ^{+0.016} _{-0.048}	0.029
100	101.4	52820.431	2384	1.440 ^{+0.003} _{-0.006}	1.367 ^{+0.004} _{-0.003}	0.073 ^{+0.001} _{-0.002}	...	0.949 ^{+0.008} _{-0.012}	0.159 ^{+0.022} _{-0.038}	0.029
101	102.4	52821.416	2304	1.441 ^{+0.002} _{-0.009}	1.320 ^{+0.003} _{-0.003}	0.120 ^{+0.002} _{-0.002}	0.300 ^{+0.063} _{-0.055}	0.916 ^{+0.004} _{-0.011}	0.034 ^{+0.002} _{-0.006}	0.028
102	103.5	52822.531	4384	1.439 ^{+0.002} _{-0.008}	1.323 ^{+0.002} _{-0.004}	0.115 ^{+0.001} _{-0.002}	0.172 ^{+0.059} _{-0.052}	0.919 ^{+0.003} _{-0.010}	0.030 ^{+0.002} _{-0.006}	0.025
103	104.5	52823.482	4736	1.361 ^{+0.002} _{-0.009}	1.254 ^{+0.002} _{-0.003}	0.107 ^{+0.001} _{-0.002}	...	0.921 ^{+0.004} _{-0.012}	0.026 ^{+0.001} _{-0.004}	0.024
104	105.5	52824.453	3328	1.391 ^{+0.001} _{-0.007}	1.256 ^{+0.003} _{-0.003}	0.135 ^{+0.002} _{-0.003}	...	0.903 ^{+0.004} _{-0.009}	0.010 ^{+0.001} _{-0.001}	0.027
105	106.4	52825.366	2192	1.381 ^{+0.002} _{-0.008}	1.233 ^{+0.003} _{-0.003}	0.148 ^{+0.002} _{-0.002}	...	0.893 ^{+0.005} _{-0.010}	0.013 ^{+0.001} _{-0.003}	0.031

Table A3—Continued

Obs. No.	Day ^b	MJD ^c	Obs. Time (s)	Total 2-20 keV (10 ⁻⁸ cgs)	Disk 2-20 keV (10 ⁻⁸ cgs)	Power Law 2-20 keV (10 ⁻⁸ cgs)	Fe Line (10 ⁻¹⁰ cgs)	Disk/Total	Power Law 2-20 keV (10 ⁻⁹ cgs)	Power Law 20-100 keV (10 ⁻⁹ cgs)	QPO ν^d (Hz)	QPO Amplitude ^e (% rms)	QPO Q^f	Cont. r^g (rms)
106	107.4	52826.425	3360	1.396 ^{+0.002} _{-0.007}	1.258 ^{+0.002} _{-0.003}	0.138 ^{+0.002} _{-0.002}	...	0.901 ^{+0.003} _{-0.009}	0.020 ^{+0.001} _{-0.003}	0.026
107	108.4	52827.411	3264	1.352 ^{+0.002} _{-0.009}	1.227 ^{+0.003} _{-0.004}	0.125 ^{+0.002} _{-0.002}	...	0.908 ^{+0.005} _{-0.012}	0.018 ^{+0.001} _{-0.003}	0.028
108	109.4	52828.369	6672	1.358 ^{+0.001} _{-0.008}	1.262 ^{+0.002} _{-0.003}	0.096 ^{+0.001} _{-0.002}	...	0.929 ^{+0.003} _{-0.011}	0.029 ^{+0.001} _{-0.004}	0.026
109	110.3	52829.277	4944	1.324 ^{+0.001} _{-0.006}	1.190 ^{+0.003} _{-0.003}	0.134 ^{+0.002} _{-0.002}	...	0.899 ^{+0.004} _{-0.008}	0.024 ^{+0.001} _{-0.003}	0.025
110	111.2	52830.186	928	1.341 ^{+0.001} _{-0.008}	1.237 ^{+0.003} _{-0.004}	0.104 ^{+0.002} _{-0.002}	...	0.922 ^{+0.004} _{-0.011}	0.030 ^{+0.001} _{-0.007}	0.027
111	112.5	52831.483	3376	1.352 ^{+0.001} _{-0.009}	1.232 ^{+0.003} _{-0.004}	0.120 ^{+0.001} _{-0.003}	...	0.911 ^{+0.004} _{-0.012}	0.030 ^{+0.001} _{-0.005}	0.025
112	115.2	52834.213	4400	1.323 ^{+0.001} _{-0.009}	1.194 ^{+0.003} _{-0.003}	0.129 ^{+0.002} _{-0.002}	...	0.902 ^{+0.004} _{-0.012}	0.019 ^{+0.001} _{-0.003}	0.023
113	118.2	52837.201	3488	1.320 ^{+0.002} _{-0.008}	1.207 ^{+0.003} _{-0.002}	0.113 ^{+0.001} _{-0.002}	...	0.914 ^{+0.005} _{-0.010}	0.014 ^{+0.001} _{-0.003}	0.024
114	121.6	52840.561	2144	1.305 ^{+0.001} _{-0.009}	1.246 ^{+0.003} _{-0.003}	0.059 ^{+0.001} _{-0.002}	...	0.955 ^{+0.004} _{-0.012}	0.061 ^{+0.003} _{-0.012}	0.027
115	124.5	52843.513	3184	1.274 ^{+0.002} _{-0.005}	1.201 ^{+0.003} _{-0.003}	0.073 ^{+0.001} _{-0.001}	0.206 ^{+0.029} _{-0.043}	0.943 ^{+0.005} _{-0.008}	0.154 ^{+0.006} _{-0.022}	0.026
116	127.2	52846.166	4912	1.250 ^{+0.002} _{-0.008}	1.172 ^{+0.003} _{-0.003}	0.078 ^{+0.001} _{-0.002}	...	0.938 ^{+0.005} _{-0.012}	0.035 ^{+0.005} _{-0.005}	0.024
117	130.9	52849.911	4688	1.193 ^{+0.001} _{-0.007}	1.104 ^{+0.002} _{-0.003}	0.089 ^{+0.001} _{-0.002}	...	0.925 ^{+0.003} _{-0.011}	0.017 ^{+0.001} _{-0.004}	0.022
118	131.9	52850.926	2080	1.214 ^{+0.001} _{-0.008}	1.085 ^{+0.003} _{-0.002}	0.129 ^{+0.002} _{-0.002}	...	0.894 ^{+0.005} _{-0.011}	0.019 ^{+0.001} _{-0.004}	0.026
119	134.0	52852.991	1760	1.190 ^{+0.001} _{-0.008}	1.130 ^{+0.003} _{-0.002}	0.060 ^{+0.001} _{-0.002}	0.178 ^{+0.028} _{-0.038}	0.950 ^{+0.005} _{-0.012}	0.046 ^{+0.003} _{-0.012}	0.027
120	136.5	52855.543	3696	1.163 ^{+0.001} _{-0.009}	1.061 ^{+0.003} _{-0.002}	0.102 ^{+0.001} _{-0.002}	...	0.912 ^{+0.005} _{-0.013}	0.019 ^{+0.001} _{-0.013}	0.022
121	143.4	52862.382	1744	1.076 ^{+0.002} _{-0.010}	1.011 ^{+0.002} _{-0.003}	0.065 ^{+0.001} _{-0.002}	0.248 ^{+0.022} _{-0.041}	0.940 ^{+0.005} _{-0.017}	0.041 ^{+0.002} _{-0.009}	0.029
122	146.4	52865.407	1952	1.030 ^{+0.001} _{-0.007}	0.925 ^{+0.002} _{-0.002}	0.105 ^{+0.002} _{-0.002}	...	0.898 ^{+0.004} _{-0.012}	0.018 ^{+0.001} _{-0.003}	0.031
123	150.4	52869.351	1456	0.982 ^{+0.001} _{-0.009}	0.892 ^{+0.002} _{-0.002}	0.090 ^{+0.001} _{-0.002}	...	0.908 ^{+0.004} _{-0.016}	0.033 ^{+0.001} _{-0.006}	0.032
124	156.1	52875.121	1648	0.934 ^{+0.001} _{-0.009}	0.872 ^{+0.001} _{-0.002}	0.062 ^{+0.001} _{-0.002}	0.170 ^{+0.018} _{-0.035}	0.934 ^{+0.003} _{-0.017}	0.033 ^{+0.002} _{-0.008}	0.028
125	158.7	52877.700	672	0.919 ^{+0.001} _{-0.010}	0.867 ^{+0.002} _{-0.003}	0.052 ^{+0.001} _{-0.002}	0.171 ^{+0.016} _{-0.031}	0.943 ^{+0.005} _{-0.020}	0.031 ^{+0.003} _{-0.018}	0.028
126	164.3	52883.292	3024	0.849 ^{+0.001} _{-0.007}	0.783 ^{+0.002} _{-0.002}	0.066 ^{+0.001} _{-0.001}	0.133 ^{+0.015} _{-0.024}	0.922 ^{+0.005} _{-0.015}	0.031 ^{+0.002} _{-0.007}	0.029
127	167.6	52886.574	1920	0.860 ^{+0.001} _{-0.008}	0.721 ^{+0.001} _{-0.002}	0.139 ^{+0.001} _{-0.002}	...	0.838 ^{+0.003} _{-0.017}	0.013 ^{+0.001} _{-0.001}	0.030
128	169.9	52888.932	2304	0.829 ^{+0.001} _{-0.006}	0.754 ^{+0.002} _{-0.002}	0.075 ^{+0.001} _{-0.001}	...	0.910 ^{+0.005} _{-0.013}	0.034 ^{+0.002} _{-0.006}	0.023
129	172.4	52891.433	2800	0.835 ^{+0.001} _{-0.004}	0.763 ^{+0.001} _{-0.002}	0.072 ^{+0.001} _{-0.001}	0.246 ^{+0.022} _{-0.035}	0.914 ^{+0.003} _{-0.009}	0.232 ^{+0.017} _{-0.022}	0.025
130	175.1	52894.054	1072	0.809 ^{+0.001} _{-0.005}	0.752 ^{+0.002} _{-0.002}	0.057 ^{+0.001} _{-0.001}	0.162 ^{+0.018} _{-0.022}	0.930 ^{+0.005} _{-0.011}	0.280 ^{+0.023} _{-0.028}	0.028
131	179.7	52898.724	960	0.721 ^{+0.001} _{-0.005}	0.660 ^{+0.002} _{-0.002}	0.061 ^{+0.001} _{-0.001}	0.387 ^{+0.021} _{-0.028}	0.915 ^{+0.016} _{-0.013}	0.189 ^{+0.016} _{-0.013}	0.032
132	181.9	52900.879	928	0.717 ^{+0.001} _{-0.008}	0.665 ^{+0.002} _{-0.002}	0.052 ^{+0.001} _{-0.001}	0.258 ^{+0.022} _{-0.030}	0.927 ^{+0.006} _{-0.020}	0.051 ^{+0.005} _{-0.013}	0.033
133	185.0	52903.988	752	0.676 ^{+0.001} _{-0.009}	0.618 ^{+0.001} _{-0.002}	0.058 ^{+0.001} _{-0.001}	0.271 ^{+0.024} _{-0.028}	0.914 ^{+0.004} _{-0.024}	0.066 ^{+0.005} _{-0.013}	0.033
134	187.0	52905.958	512	0.661 ^{+0.001} _{-0.005}	0.615 ^{+0.001} _{-0.002}	0.046 ^{+0.001} _{-0.001}	0.407 ^{+0.020} _{-0.027}	0.930 ^{+0.004} _{-0.014}	0.229 ^{+0.019} _{-0.038}	0.036
135	187.1	52906.083	2240	0.645 ^{+0.001} _{-0.003}	0.590 ^{+0.002} _{-0.001}	0.055 ^{+0.001} _{-0.001}	0.267 ^{+0.026} _{-0.031}	0.915 ^{+0.007} _{-0.008}	0.162 ^{+0.010} _{-0.013}	0.030
136	189.5	52908.515	2352	0.620 ^{+0.001} _{-0.003}	0.577 ^{+0.002} _{-0.001}	0.043 ^{+0.002} _{-0.001}	0.275 ^{+0.023} _{-0.025}	0.931 ^{+0.007} _{-0.009}	0.188 ^{+0.013} _{-0.044}	0.024
137	190.6	52909.571	2928	0.606 ^{+0.001} _{-0.003}	0.551 ^{+0.001} _{-0.001}	0.055 ^{+0.001} _{-0.001}	0.315 ^{+0.020} _{-0.029}	0.909 ^{+0.004} _{-0.008}	0.296 ^{+0.013} _{-0.019}	0.028
138	192.5	52911.546	3456	0.617 ^{+0.001} _{-0.002}	0.535 ^{+0.001} _{-0.002}	0.082 ^{+0.001} _{-0.001}	0.445 ^{+0.026} _{-0.030}	0.867 ^{+0.004} _{-0.008}	0.444 ^{+0.020} _{-0.012}	0.026
139	193.5	52912.531	3408	0.618 ^{+0.001} _{-0.003}	0.514 ^{+0.001} _{-0.002}	0.104 ^{+0.001} _{-0.001}	0.334 ^{+0.022} _{-0.029}	0.832 ^{+0.004} _{-0.009}	0.572 ^{+0.011} _{-0.025}	0.022
140	195.5	52914.504	2352	0.523 ^{+0.001} _{-0.003}	0.471 ^{+0.001} _{-0.001}	0.052 ^{+0.001} _{-0.001}	0.397 ^{+0.022} _{-0.024}	0.901 ^{+0.005} _{-0.010}	0.256 ^{+0.016} _{-0.007}	0.025

Table A3—Continued

Obs. No.	Day ^b	MJD ^c	Obs. Time (s)	Total 2-20 keV (10 ⁻⁸ cgs)	Disk 2-20 keV (10 ⁻⁸ cgs)	Power Law 2-20 keV (10 ⁻⁸ cgs)	Fe Line (10 ⁻¹⁰ cgs)	2-20 keV Disk/Total	Power Law 20-100 keV (10 ⁻⁹ cgs)	QPO ν^d (Hz)	QPO Amplitude ^e (% rms)	QPO Q^f	Cont. r^g (rms)
141	197.4	52916.408	3328	0.490 ^{+0.001} _{-0.002}	0.416 ^{+0.001} _{-0.001}	0.074 ^{+0.001} _{-0.001}	0.436 ^{+0.024} _{-0.027}	0.849 ^{+0.005} _{-0.007}	0.408 ^{+0.017} _{-0.017}	0.026
142	198.6	52917.591	3360	0.474 ^{+0.001} _{-0.002}	0.404 ^{+0.001} _{-0.001}	0.070 ^{+0.001} _{-0.001}	0.392 ^{+0.021} _{-0.019}	0.852 ^{+0.005} _{-0.007}	0.381 ^{+0.020} _{-0.013}	0.031
143	201.1	52920.148	2448	0.395 ^{+0.001} _{-0.002}	0.354 ^{+0.001} _{-0.001}	0.041 ^{+0.001} _{-0.001}	0.242 ^{+0.026} _{-0.024}	0.896 ^{+0.007} _{-0.010}	0.170 ^{+0.013} _{-0.018}	0.031
144	202.5	52921.474	2192	0.366 ^{+0.001} _{-0.002}	0.324 ^{+0.001} _{-0.001}	0.042 ^{+0.001} _{-0.001}	0.323 ^{+0.023} _{-0.027}	0.885 ^{+0.007} _{-0.011}	0.173 ^{+0.016} _{-0.009}	0.035
145	205.2	52924.157	2624	0.318 ^{+0.001} _{-0.002}	0.281 ^{+0.001} _{-0.001}	0.037 ^{+0.001} _{-0.001}	0.311 ^{+0.025} _{-0.023}	0.884 ^{+0.008} _{-0.012}	0.187 ^{+0.012} _{-0.013}	0.037
146	207.2	52926.198	3392	0.283 ^{+0.001} _{-0.001}	0.237 ^{+0.001} _{-0.001}	0.046 ^{+0.001} _{-0.001}	0.246 ^{+0.030} _{-0.018}	0.837 ^{+0.009} _{-0.009}	0.196 ^{+0.014} _{-0.007}	0.028
147	208.1	52927.118	3328	0.264 ^{+0.001} _{-0.001}	0.223 ^{+0.001} _{-0.001}	0.041 ^{+0.001} _{-0.001}	0.238 ^{+0.028} _{-0.024}	0.845 ^{+0.010} _{-0.010}	0.159 ^{+0.014} _{-0.007}	0.033
148	209.5	52928.507	1792	0.248 ^{+0.001} _{-0.002}	0.202 ^{+0.001} _{-0.001}	0.046 ^{+0.001} _{-0.001}	0.270 ^{+0.024} _{-0.027}	0.815 ^{+0.010} _{-0.014}	0.194 ^{+0.016} _{-0.011}	0.045
149	210.4	52929.351	3392	0.219 ^{+0.001} _{-0.001}	0.172 ^{+0.001} _{-0.001}	0.047 ^{+0.001} _{-0.001}	0.309 ^{+0.031} _{-0.029}	0.785 ^{+0.010} _{-0.010}	0.265 ^{+0.015} _{-0.009}	0.038
150	211.0	52929.967	3456	0.232 ^{+0.001} _{-0.001}	0.178 ^{+0.001} _{-0.001}	0.054 ^{+0.001} _{-0.001}	0.275 ^{+0.026} _{-0.019}	0.767 ^{+0.010} _{-0.010}	0.306 ^{+0.013} _{-0.011}	0.037
151	212.0	52930.953	3424	0.250 ^{+0.001} _{-0.001}	0.156 ^{+0.001} _{-0.001}	0.094 ^{+0.001} _{-0.001}	0.390 ^{+0.029} _{-0.027}	0.624 ^{+0.008} _{-0.008}	0.434 ^{+0.018} _{-0.014}	0.070
152	213.1	52932.110	3248	0.234 ^{+0.001} _{-0.001}	0.110 ^{+0.001} _{-0.001}	0.124 ^{+0.001} _{-0.001}	0.502 ^{+0.032} _{-0.022}	0.470 ^{+0.007} _{-0.007}	0.637 ^{+0.022} _{-0.014}	7.87	3.55 ± 0.21	11.9	0.082
153	214.3	52933.294	3376	0.189 ^{+0.001} _{-0.001}	0.132 ^{+0.001} _{-0.001}	0.057 ^{+0.001} _{-0.001}	0.281 ^{+0.024} _{-0.024}	0.698 ^{+0.011} _{-0.008}	0.308 ^{+0.013} _{-0.012}	0.050
154	215.0	52934.016	3376	0.205 ^{+0.001} _{-0.001}	0.106 ^{+0.001} _{-0.001}	0.099 ^{+0.001} _{-0.001}	0.402 ^{+0.028} _{-0.027}	0.517 ^{+0.010} _{-0.008}	0.484 ^{+0.016} _{-0.010}	7.65	4.05 ± 0.35	4.6	0.078
155	216.1	52935.071	2816	0.175 ^{+0.001} _{-0.001}	0.101 ^{+0.001} _{-0.001}	0.074 ^{+0.001} _{-0.001}	0.258 ^{+0.035} _{-0.028}	0.577 ^{+0.010} _{-0.010}	0.326 ^{+0.015} _{-0.015}	5.97	3.42 ± 0.46	6.9	0.073
156	217.0	52936.046	2224	0.172 ^{+0.001} _{-0.001}	0.078 ^{+0.001} _{-0.001}	0.094 ^{+0.001} _{-0.001}	0.313 ^{+0.030} _{-0.016}	0.453 ^{+0.009} _{-0.009}	0.426 ^{+0.016} _{-0.015}	8.03	3.55 ± 0.46	8.8	0.084
157	218.0	52937.038	3392	0.160 ^{+0.001} _{-0.001}	0.053 ^{+0.001} _{-0.001}	0.107 ^{+0.001} _{-0.001}	0.387 ^{+0.029} _{-0.027}	0.331 ^{+0.009} _{-0.009}	0.592 ^{+0.018} _{-0.013}	7.01	5.14 ± 0.22	10.2	0.111
158	219.0	52938.016	2048	0.147 ^{+0.001} _{-0.001}	0.033 ^{+0.001} _{-0.001}	0.114 ^{+0.001} _{-0.001}	0.258 ^{+0.034} _{-0.031}	0.224 ^{+0.009} _{-0.009}	0.605 ^{+0.018} _{-0.025}	5.91	7.59 ± 0.35	4.3	0.138
159	220.1	52939.132	1984	0.131 ^{+0.001} _{-0.001}	0.027 ^{+0.001} _{-0.001}	0.104 ^{+0.001} _{-0.001}	0.202 ^{+0.037} _{-0.026}	0.206 ^{+0.010} _{-0.010}	0.510 ^{+0.016} _{-0.023}	5.85	7.18 ± 0.31	6.0	0.132
160	223.2	52942.154	1936	0.088 ^{+0.001} _{-0.001}	0.011 ^{+0.001} _{-0.001}	0.077 ^{+0.001} _{-0.001}	0.179 ^{+0.034} _{-0.029}	0.125 ^{+0.013} _{-0.013}	0.629 ^{+0.013} _{-0.025}	3.07	8.26 ± 0.41	2.8	0.170
161	223.7	52942.700	1552	0.080 ^{+0.001} _{-0.002}	0.010 ^{+0.001} _{-0.001}	0.070 ^{+0.001} _{-0.001}	0.130 ^{+0.037} _{-0.033}	0.125 ^{+0.014} _{-0.014}	0.518 ^{+0.009} _{-0.026}	2.81	6.91 ± 0.49	6.2	0.177
162	225.2	52944.200	9872	0.068 ^{+0.001} _{-0.001}	0.007 ^{+0.001} _{-0.001}	0.061 ^{+0.001} _{-0.001}	0.123 ^{+0.022} _{-0.026}	0.103 ^{+0.016} _{-0.016}	0.509 ^{+0.006} _{-0.008}	2.48	7.58 ± 0.30	2.9	0.172
163	226.2	52945.178	1664	0.056 ^{+0.001} _{-0.001}	0.009 ^{+0.001} _{-0.001}	0.047 ^{+0.001} _{-0.001}	0.198 ^{+0.037} _{-0.048}	0.161 ^{+0.019} _{-0.019}	0.535 ^{+0.023} _{-0.024}	0.165
164	227.2	52946.171	10342	0.049 ^{+0.001} _{-0.001}	< 0.001	0.049 ^{+0.001} _{-0.001}	0.031 ^{+0.026} _{-0.037}	< 0.022	0.351 ^{+0.033^{aa}_{-0.006}}	0.155
165	228.1	52947.053	1040	0.047 ^{+0.001} _{-0.001}	0.005 ^{+0.001} _{-0.001}	0.042 ^{+0.001} _{-0.001}	0.107 ^{+0.032} _{-0.059}	0.106 ^{+0.025} _{-0.025}	0.376 ^{+0.019} _{-0.021}	0.151
166	229.2	52948.234	5072	0.038 ^{+0.001} _{-0.001}	0.005 ^{+0.001} _{-0.001}	0.033 ^{+0.001} _{-0.001}	0.135 ^{+0.031} _{-0.036}	0.132 ^{+0.029} _{-0.029}	0.301 ^{+0.013} _{-0.016}	0.139
167	230.2	52949.195	13696	0.035 ^{+0.001} _{-0.001}	< 0.001	0.035 ^{+0.001} _{-0.001}	0.035 ^{+0.011} _{-0.014}	< 0.032	0.231 ^{+0.033^{aa}_{-0.004}}	0.129
168	231.5	52950.477	2816	0.033 ^{+0.001} _{-0.001}	0.003 ^{+0.001} _{-0.001}	0.030 ^{+0.001} _{-0.001}	0.063 ^{+0.034} _{-0.032}	0.091 ^{+0.037} _{-0.037}	0.209 ^{+0.019} _{-0.020}	0.131
169	232.4	52951.425	4128	0.028 ^{+0.001} _{-0.001}	0.003 ^{+0.001} _{-0.001}	0.025 ^{+0.001} _{-0.001}	0.102 ^{+0.023} _{-0.031}	0.107 ^{+0.043} _{-0.043}	0.193 ^{+0.017} _{-0.015}	0.140
170	233.3	52952.276	2016	0.023 ^{+0.001} _{-0.001}	< 0.001	0.023 ^{+0.001} _{-0.001}	0.050 ^{+0.031} _{-0.032}	< 0.050	0.121 ^{+0.005^{aa}_{-0.006}}	0.155

^aFluxes are in cgs units: ergs cm⁻² s⁻¹.^bNumber of days since discovery on 2003 March 21 = MJD 52719 (Revintsev et al. 2003).^cStart time of observation: MJD = JD - 2,400,000.5.

^dCentroid frequency of the primary QPO peak; uncertainties are generally < 5% at the 95% confidence level.

^eThe QPO amplitude is the fractional rms fluctuation, calculated as the square root of the integrated power in the QPO feature and expressed as a fraction of the mean count rate. Errors are 1σ , with a lower limit of 0.1% for systematic uncertainty in the continuum model, except for especially narrow QPOs ($Q > 10$).

^f $Q = \text{QPO Frequency}/\text{FWHM}$.

^gTotal rms power (r) integrated over 0.1-10 Hz in the power density spectrum (2-30 keV).

^hModel components include broken power law and a Gaussian emission line and exclude a thermal component (dof = 88). The break energy is 25.0 keV for observation #1, and is 15.0 keV otherwise. Upper limits are at the 99% level of confidence and were calculated for an assumed value of $R_{\text{in}} = 25$ km.

ⁱFitted using data from HEXTE Cluster 1 because data from Cluster 0 saturated the telemetry.

^jHarmonic present at 2ν .

^kPair of harmonics present at 0.5ν and 2ν .

^mWeak harmonic present at 2ν .

ⁿAdditional weak QPO at 3.9 Hz.

^oBroad harmonic possibly present at 0.5ν .

^qAdditional QPO at 4.54 Hz of similar strength.

^pHEXTE fitting range restricted to $E > 29.1$ keV.

^rAdditional narrow QPO at 5.14 Hz.

^sAdditional weaker QPO at 4.3 Hz.

^tWeak and broad harmonic at frequency 2ν .

^uAdditional QPO at 9.0 Hz of similar strength.

^vWeak and broad harmonic possibly present at 2ν .

^wAdditional QPO at 4.6 Hz of similar strength.

^xStrong harmonic present at 2ν .

^yHarmonic present at 0.5ν .

^zPCA fitting range restricted to $E = 2.8 - 22.4$ keV (includes PHA channels 4-49; 86 dof).

^{aa}Model components include a simple power law and a Gaussian emission line and exclude a thermal component (dof = 90). Upper limits are at the 99% level of confidence and were calculated for an assumed value of $R_{\text{in}} = 25$ km.

Table A4. VLA Radio Flux Densities for H1743-322: $\nu \leq 8.640$ GHz

UT 2003 (mmdd)	MJD ^a	Day ^b	1.425 GHz		4.860 GHz		8.460 GHz		
			S_ν (mJy)	MJD	Day	S_ν (mJy)	MJD	Day	
0330	52728.6016	9.6	3.39 \pm 0.15	52728.5938	9.6	4.57 \pm 0.12
0401	52730.5586	11.6	8.19 \pm 1.53	52730.5547	11.6	5.78 \pm 0.18	52730.5469	11.6	6.45 \pm 0.12
0403	52732.5195	13.5	15.31 \pm 0.20	52732.5469	13.6	16.99 \pm 0.12
0404	52733.5195	14.5	20.08 \pm 0.24	52733.5156	14.5	18.68 \pm 0.31
0404	52733.5469	14.6	21.81 \pm 0.13
0406	52735.4062	16.4	20.27 \pm 0.26	52735.4219	16.4	19.62 \pm 0.16
0406	52735.4375	16.4	20.47 \pm 0.18	52735.4414	16.4	19.58 \pm 0.13
0406	52735.4688	16.5	20.23 \pm 0.22	52735.4648	16.5	19.43 \pm 0.16
0408	52737.4844	18.5	96.07 \pm 0.20	52737.4961	18.5	68.04 \pm 0.16
0409	52738.4453	19.4	27.03 \pm 1.54	52738.4570	19.5	23.10 \pm 0.17	52738.4609	19.5	20.29 \pm 0.08
0410	52739.4609	20.5	14.94 \pm 1.53	52739.4766	20.5	21.37 \pm 0.18	52739.4570	20.5	21.10 \pm 0.13
0410	52739.4961	20.5	20.65 \pm 0.08
0410	52739.5391	20.5	20.28 \pm 0.11
0411	52740.5508	21.6	63.34 \pm 1.74	52740.5547	21.6	24.95 \pm 0.20	52740.5469	21.6	16.07 \pm 0.12
0412	52741.5430	22.5	32.86 \pm 1.49	52741.5625	22.6	12.78 \pm 0.21	52741.5625	22.6	7.71 \pm 0.12
0413	52742.4961	23.5	8.10 \pm 1.23	52742.5195	23.5	4.40 \pm 0.22	52742.5195	23.5	3.87 \pm 0.13
0416	52745.4375	26.4	41.44 \pm 0.24	52745.4336	26.4	37.15 \pm 0.13
0420	52749.6055	30.6	16.48 \pm 0.38	52749.5977	30.6	12.46 \pm 0.20
0421	52750.5977	31.6	23.10 \pm 0.51	52750.5977	31.6	20.94 \pm 0.31
0423	52752.5352	33.5	12.20 \pm 0.26	52752.5352	33.5	11.48 \pm 0.20
0426	52755.5352	36.5	9.73 \pm 1.21	52755.5312	36.5	7.54 \pm 0.17	52755.4961	36.5	5.58 \pm 0.12
0429	52758.4062	39.4	7.48 \pm 1.27	52758.4219	39.4	8.45 \pm 0.16	52758.4141	39.4	6.64 \pm 0.10
0506	52765.4375	46.4	13.78 \pm 0.21	52765.4219	46.4	11.12 \pm 0.13
0508	52767.5195	48.5	25.62 \pm 0.19	52767.5195	48.5	23.02 \pm 0.12
0509	52768.5039	49.5	34.59 \pm 0.24	52768.4922	49.5	30.14 \pm 0.16
0510	52769.5156	50.5	28.04 \pm 0.19	52769.5078	50.5	23.80 \pm 0.14
0514	52773.3633	54.4	35.76 \pm 0.23
0520	52779.4141	60.4	14.15 \pm 0.31	52779.4414	60.4	11.77 \pm 0.16
0520	52779.4141	60.4	14.01 \pm 0.37	52779.4414	60.4	12.21 \pm 0.30
0527	52786.3477	67.3	21.49 \pm 0.12	52786.0000	67.0	15.57 \pm 0.30
0527	52786.0000	67.0	15.87 \pm 0.32
0527	52786.3477	67.3	22.49 \pm 0.41	52786.3555	67.4	15.81 \pm 0.27
0527	52786.3555	67.4	16.06 \pm 0.12
0527	52786.4844	67.5	16.90 \pm 0.38
0527	52786.4844	67.5	16.15 \pm 0.16
0529	52788.3750	69.4	5.59 \pm 0.05
0604	52794.4023	75.4	4.34 \pm 0.04
0609	52799.2539	80.3	0.81 \pm 0.06
0610	52800.2344	81.2	1.43 \pm 0.12	52800.2383	81.2	0.94 \pm 0.09	52800.2539	81.3	0.42 \pm 0.04
0611	52801.2969	82.3	0.34 \pm 0.04
0619	52809.2070	90.2	2.37 \pm 0.13	52809.2148	90.2	1.72 \pm 0.09	52809.2227	90.2	1.42 \pm 0.06
0627	52817.2383	98.2	2.29 \pm 0.09
0628	52818.2383	99.2	3.16 \pm 0.07
0709	52829.3477	110.3	1.28 \pm 0.12	52829.3398	110.3	0.45 \pm 0.05
0713	52833.2148	114.2	1.17 \pm 0.14	52833.2188	114.2	0.46 \pm 0.10	52833.2148	114.2	0.28 \pm 0.06
0716	52836.3320	117.3	0.97 \pm 0.17	52836.3359	117.3	< 0.18

Table A4—Continued

UT 2003 (mmdd)	MJD ^a	Day ^b	1.425 GHz		4.860 GHz		8.460 GHz		
			S_ν (mJy)	MJD	Day	S_ν (mJy)	MJD	Day	
0722	52842.2930	123.3	< 0.65 ^c	52842.2930	123.3	< 0.22
0728	52848.2422	129.2	< 0.55
0729	52849.1953	130.2	< 0.66
0731	52851.3203	132.3	< 0.84
0803	52852.3203	133.3	< 0.71
0806	52857.1055	138.1	< 0.37
0812	52863.0508	144.1	< 0.61	52863.0742	144.1	< 0.03
0817	52868.1250	149.1	< 0.37	52868.1406	149.1	< 0.30
0819	52870.0742	151.1	< 0.21	52870.0938	151.1	< 0.12
0819
0822	52873.1211	154.1	< 0.40
0825	52877.0000	158.0	< 0.99	52877.0195	158.0	< 0.34
0903	52885.1133	166.1	< 0.13
0906	52888.1367	169.1	< 0.68	52888.1250	169.1	< 0.31	52888.1133	169.1	< 0.22
0913	52895.1562	176.2	< 0.35
0914	52896.1367	177.1	< 0.30
0916	52898.1719	179.2	< 0.48	52898.1602	179.2	< 0.22
0920	52903.0312	184.0	< 0.18
0925	52907.1680	188.2	< 0.37
0927	52909.1250	190.1	< 0.34	52909.1055	190.1	< 0.24
1002	52915.0234	196.0	< 0.18	52915.0078	196.0	< 0.23
1012	52924.9336	205.9	< 0.30	52924.9180	205.9	< 0.31
1020	52932.9727	214.0	< 0.36	52932.9609	214.0	< 0.10
1027	52940.0195	221.0	0.21 ± 0.06	52939.9961	221.0	0.14 ± 0.04
1029	52941.9570	223.0	< 0.38	52941.9453	222.9	< 0.38
1104	52948.0391	229.0	< 1.08	52948.0234	229.0	0.14 ± 0.06	52948.0039	229.0	0.22 ± 0.05
1106	52949.9531	231.0	0.18 ± 0.04	52949.9414	230.9	< 0.42

^aModified Julian Day = JD – 2,400,000.5.

^bNumber of days since discovery on 2003 March 21 = MJD 52719 (Revnivtsev et al. 2003).

^cUpper limits correspond to the flux density measured at the nominal position of the center of the beam plus three times the rms noise.

Table A5. VLA Radio Flux Densities for H1743–322: $\nu \geq 14.940$ GHz

UT 2003 (mmdd)	MJD ^a	Day ^b	14.940 GHz		22.460 GHz		43.340 GHz	
			S_ν (mJy)	MJD	Day	S_ν (mJy)	MJD	Day
0401	52730.5430	11.5	6.81 ± 0.51
0403	52732.5391	13.5	19.20 ± 0.33	52732.5352	13.5	21.32 ± 0.23	52732.5234	13.5
0404	52733.5430	14.5	26.57 ± 0.40	52733.5391	14.5	26.36 ± 0.26	52733.5273	14.5
0406	52735.4570	16.5	20.15 ± 0.45	52735.4531	16.5	22.69 ± 0.46	52735.4453	16.4
0408	52737.5000	18.5	42.62 ± 0.44	52737.5078	18.5	51.01 ± 0.25	52737.4961	18.5
0408	52737.5156	18.5	55.21 ± 0.32
0409	52738.4805	19.5	19.58 ± 0.31	52738.4766	19.5	21.13 ± 0.17	52738.4766	19.5
0404	52738.4727	19.5
0409	52738.4883	19.5
0410	52739.5000	20.5	21.49 ± 0.32	52739.4922	20.5	24.03 ± 0.23	52739.4961	20.5
0410	52739.4844	20.5
0410	52739.5078	20.5
0411	52740.5664	21.6	9.27 ± 0.43	52740.5625	21.5	6.53 ± 0.39	52740.5586	21.6
0412	52741.5586	22.6	5.99 ± 0.43	52741.5547	22.6	4.62 ± 0.33	52741.5508	22.6
0413	52742.5156	23.5	2.52 ± 0.36	52742.5078	23.5	2.47 ± 0.26	52742.5039	23.5
0423	52752.5430	33.5	9.46 ± 0.60
0426	52755.5039	36.5	3.70 ± 0.28

^aTruncated Modified Julian Day = MJD - 52000.

^bNumber of days since discovery on 2003 March 21 = MJD 52719 (Revnivtsev et al. 2003).

Table A6. Radio Spectral Index

UT 2003 (mmddd)	MJD ^a	Day ^b	Spectral Index α
0330	52728.598	9.6	0.54 ± 0.09
0401	52730.551	11.6	0.20 ± 0.07
0404	52733.518	14.5	-0.13 ± 0.04
0406	52735.414	16.4	-0.06 ± 0.03
0406	52735.439	16.4	-0.08 ± 0.02
0406	52735.467	16.5	-0.07 ± 0.02
0408	52737.490	18.5	-0.62 ± 0.01
0409	52738.459	19.5	-0.23 ± 0.02
0411	52740.551	21.6	-0.79 ± 0.02
0412	52741.563	22.6	-0.91 ± 0.04
0413	52742.520	23.5	-0.23 ± 0.11
0416	52745.436	26.4	-0.20 ± 0.01
0420	52749.602	30.6	-0.50 ± 0.05
0421	52750.598	31.6	-0.18 ± 0.05
0423	52752.535	33.5	-0.11 ± 0.05
0429	52758.418	39.4	-0.43 ± 0.04
0506	52765.430	46.4	-0.39 ± 0.03
0508	52767.520	48.5	-0.19 ± 0.02
0509	52768.498	49.5	-0.25 ± 0.02
0510	52769.512	50.5	-0.30 ± 0.02
0527	52786.352	67.3	-0.64 ± 0.05
0610	52800.246	81.2	-1.45 ± 0.24
0619	52809.219	90.2	-0.35 ± 0.12
0709	52829.344	110.3	-1.89 ± 0.26
0713	52833.217	114.2	-0.90 ± 0.55

^aModified Julian Day = JD - 2,400,000.5.^bNumber of days since discovery on 2003 March 21 = MJD 52719 (Revnivtsev et al. 2003).

REFERENCES

Abramowicz, M. A., & Kluzniak, W. 2001, A&A, 374, L19

Arnaud, K., & Dorman, B. 2003, XSPEC, An X-ray Spectral Fitting Package, provided by NASA/GSFC, available via HEASARC

Baba, D., & Nagata, T. 2003, IAUC 8112

Balucinski-Church, M., & McCammon, D. 1992, ApJ, 400, 699

Belloni, T., Homan, J., Casella, P., et al. 2005, A&A, 440, 207

Buxton, M. M., & Bailyn, C. D. 2007, AJ, submitted

Capitanio, F., Bazzano, A., Ubertini, P., et al. 2006, ApJ, 643, 376

Capitanio, F., Ubertini, P., Bazzano, A., et al. 2005, ApJ, 622, 503

Charles, P. A., & Coe, M. J. 2005, in Compact Stellar X-ray Sources, eds. W. Lewin & M. van der Klis (Cambridge: Cambridge Univ. Press), p215

Cooke, B. A., Levine, A. M., Lang, F. L., Primini, F. A., & Lewin, W. H. G. 1984, ApJ, 285, 258

Corbel, S., Fender, R. P., Tzioumis, A. K., et al. 2002, Science, 298, 196

Corbel, S., Kaaret, P., Fender, R. P., Tzioumis, A. K., Tomsick, J. A., & Orosz, J. A. 2005, ApJ, 632, 504

Davis, S. W., Blaes, O. M., Hubeny, I., & Turner, N. J. 2005, ApJ, 621, 372

Doxsey, R., Bradt, H., Fabbiano, G., et al. 1977, IAUC 3113

Ebisawa, K., Ogawa, M., Aoki, T., et al. 1994, PASJ, 46, 375

Gursky, H., Bradt, H., Doxsey, R., et al. 1978, ApJ, 223, 973

Hannikainen, D., Campbell-Wilson, D., Hunstead, R. et al. 2001, Ap&SSS, 276, 45

Homan, J., Miller, J. M., Wijnands, R., van der Klis, M., Belloni, T., Steeghs, D., & Lewin, W. H. G. 2005, ApJ, 623, 383

Homan, J., Wijnands, R., van der Klis, M., Belloni, T., et al. 2001, ApJS, 132, 377

Joinet, A., Jourdain, E., Malzac, J., Roques, J. P., Schönfelder, V., Ubertini, P., & Capitanio, F. 2005, *ApJ*, 629, 1008

Kaaret, P., Corbel, S., Tomsick, J. A., Fender, R., Miller, J. M., Orosz, J. A., Tzioumis, A. K., & Wijnands, R. 2003, *ApJ*, 582, 945

Kalemci, E., Tomsick, J. A., Rothschild, R. E., Pottschmidt, K., Corbel, S., & Kaaret, P. 2006, *ApJ*, 639, 340

Kaluzienski, L. J., & Holt, S. S. 1977, *IAUC* 3099

Kubota, A., & Done, C. 2004, *MNRAS*, 353, 980

Kubota, A., & Makishima, K. 2004, *ApJ*, 601, 428

Kubota, A., Makishima, K., & Ebisawa, K. 2001, *ApJ*, 560, L147

Lutovinov, A., Revnivtsev, M., Molkov, S., & Sunyaev, R. 2005, *A&A*, 430, 997

Makishima, K., Maejima, Y., Mitsuda, K., et al. 1986, *ApJ*, 308, 635

Markwardt, C. B., & Swank, J. H. 2003a, *ATEL* 133

Markwardt, C. B., & Swank, J. H. 2003b, *ATEL* 136

Markwardt, C. B., & Swank, J. H., & Taam, R. E. 1999, *ApJ*, 513, L37

Martini, P., Persson, S. E., Murphy, D. C., Birk, C., Shectman, S. A., Gunnels, S. M., & Koch, E. 2004, *Proc. SPIE*, 5492, 1653

McClintock, J. E., & Remillard, R. A. 2006, in *Compact Stellar X-ray Sources*, eds. W. Lewin & M. van der Klis (Cambridge: Cambridge Univ. Press), p157

Miller, J. M., Raymond, J., Homan, J., et al. 2006, *ApJ*, 646, 394

Mitsuda, K., Inoue, H., Koyama, K., et al. 1984, *PASJ*, 36, 741

Muno, M. P., Morgan, E. H., & Remillard, R. A. 1999, *ApJ*, 527, 321

Narayan, R., & McClintock, J. E. 2005, *ApJ*, 623, 1017

Orosz, J. A. 2003, *A Massive Star Odyssey: From Main Sequence to Supernova*, eds. K. A. van der Hucht, A. Herrero, & C. Esteban, (San Francisco: Astron.Soc.Pac.), p365

Orosz, J. A., Groot, P. J., van der Klis, M., et al. 2002, *ApJ*, 568, 2002

Park, S. Q., Miller, J. M., McClintock, J. E., et al. 2004, *ApJ*, 610, 378

Parmar, A. N., Kuulkers, E., Oosterbroek, P., et al. 2003, *A&A*, 411, L421

Persson, S. E., Murphy, D. C.; Krzeminski, W., Roth, M., Rieke, M. J. 1998, *AJ*, 116, 2475

Predehl, P., & Schmitt, J. H. M. M. 1995, *A&A*, 293, 889

Remillard, R. A. 2005, to appear in *Interacting Binaries: Accretion, Evolution and Outcomes*, eds. L. A. Antonelli et al., *Procs. Interacting Binaries Meeting*, AIP, in press

Remillard, R. A., & McClintock, J. E. 2006, *ARAA*, 44, 49

Remillard, R. A., McClintock, J. E., Orosz, J. A., & Levine A. M. 2006, *ApJ*, 637, 1002

Remillard, R. A., Muno, M. P., McClintock, J. E., & Orosz, J. A. 2002a, *ApJ*, 580, 1030

Remillard, R. A., Sobczak, G. J., Muno, M. P., & McClintock, J. E. 2002b, *ApJ*, 564, 962

Revnivtsev, M., Chernyakova, M., Westergaard, N. J., Shoenfelder, V., Gehrels, N., & Winckler, C. 2003, *ATEL* 132

Revnivtsev, M. G., Trudolyubov, S. P., & Borozdin, K. N. 2000, *MNRAS*, 312, 151

Rothschild, R. E., Blanco, P. R., Gruber, D. E., et al. 1998, *ApJ*, 496, 538

Rupen, M. P., Mioduszewski, A. J., & Dhawan 2003, *ATEL* #137 & #139

Schlegel 1998, *ApJ*, 500, 525

Shakura, N. I., & Sunyaev, R. A. 1973, *A&A*, 24, 337

Shimura, T., & Takahara, F. 1995, *ApJ*, 445, 780

Sobczak, G. J., McClintock, J. E., Remillard, R. A., & Bailyn, C. D. 1999, *ApJ*, 520, 776

Sobczak, G. J., McClintock, J. E., Remillard, R. A., Cui, W., Levine, A. M., & Morgan, E. H. 2000a, *ApJ*, 531, 537

Sobczak, G. J., McClintock, J. E., Remillard, R. A., et al. 2000b, *ApJ*, 544, 993

Steeghs, D., Miller, J. M., Kaplan, D., & Rupen, M. 2003, *ATELs* #141 & #146

Stetson, P. B. 1987, *PASP*, 99, 191

Swank, J. 1998, in The Active X-ray Sky: Results from *BeppoSAX* and *Rossi-XTE*, eds. L. Scarsi et al., Nuclear Phys. B Proc. Supp.

Tanaka, Y., & Lewin, W. H. G. 1995, in X-ray Binaries, eds. W. Lewin, J. van Paradijs, & E. van den Heuvel (Cambridge: Cambridge Univ. Press), p126

Titarchuk, L., & Fiorito, R. 2004, ApJ, 612, 988

Titarchuk, L., & Shaposhnikov, N. 2005, ApJ, 626, 298

Tomsick, J. A., Corbel, S., Fender, R., Miller, J. M., Orosz, J. A., Tzioumis, T., Wijnands, R., & Kaaret, P. 2003, ApJ, 582, 933

Tomsick, J. A., Corbel, S., Goldwurm, A., & Kaaret, P. 2005, ApJ, 630, 413

van Paradijs, J., & McClintock, J. E. 1994, A&A, 290, 133

Wagoner, R. V. 1999, Physics Reports, 311, 259

White, N. E., & Marshall, F. E. 1984, ApJ, 281, 354

Yan, M., Sadeghpour, H. R., & Dalgarno, A. 1998, ApJ, 496, 1044

Yuan, F., Cui, W., & Narayan, R. 2005, ApJ, 620, 905

Fig. 1.— *RXTE* ASM light curve (1.5–12 keV) and hardness ratio (HR2; 5–12 keV/3–5 keV) covering the entire 2003 outburst of H1743–322. The small vertical lines in the top panel indicate the times of the 170 pointed observations discussed in the text. The day number is the time in days since the discovery of the outburst on 2003 March 21 (= MJD 52719).

Fig. 2.— The high-energy photon index ($E > 15$ keV) was fitted independently for the PCU-2 (15–25 keV) and the HEXTE-A (24–200 keV) detectors, and the results are compared here. For each observation, a Gaussian weighted average of the two indices was computed to give the single photon index, Γ_{HI} (see Fig. 3 and Table A2). The errors are generally much smaller for the HEXTE-A detector because of its greater bandwidth. Consequently, the values of Γ_{HI} reported in §3 are generally close to the values determined by HEXTE-A alone.

Fig. 3.— The evolution of H1743-322 during its 2003 outburst. (a) The ASM light curve (see Fig. 1). (b) The unabsorbed model flux (2–20 keV) computed using the 170 sets of parameters given in Table A2. The symbol type denotes the X-ray state (see text): thermal (red cross); hard (blue square); steep power-law (green triangle); and any type of intermediate state (magenta circle).

Fig. 4.— Spectral parameters and fluxes for 170 observations of H1743–322 spanning 225 days. The broken (simple) power-law model was used to the left (right) of the vertical line drawn at day 102. All the data presented here are contained in Tables A2 & A3. The spectral parameters shown plotted are (a) the X-ray state (see Fig. 3 for key to plotting symbols); (b) the color temperature of the accretion disk T_{in} in keV; (c) the inner disk radius $R^*(\text{km}) = R_{\text{in}}(\cos i)^{1/2}/(D/10 \text{ kpc})$, where i is the inclination angle and D is the distance to the source in kpc; and (d) the power-law photon indices, where the magenta data points are for Γ ($E < 15$ keV) and the red points are for Γ_{HI} ($E > 15$ keV). The unabsorbed fluxes shown in units of $10^{-8} \text{ ergs cm}^{-2} \text{ s}^{-1}$ are for (e) the Fe-K line; (f) the disk (2–20 keV); (g) the power law (2–20 keV); (h) the total (2–20 keV); and (i) the high-energy power law (20–100 keV). The low disk fluxes plotted in red are discussed in §3.4.1. All the data are plotted with error bars, although they are usually too small to be apparent. The downward arrows in (b) and (f) indicate upper limits at the 99% level of confidence. For day numbers $\gtrsim 100$, the fluxes in (g)–(i) are quite low; consequently, in order to better display these quantities they have been multiplied by the factor indicated in each panel and replotted as small, green symbols.

Fig. 5.— Timing data based on a power density spectrum analysis. The state classification is shown in (a), and the 0.1–10 Hz continuum power in the PDS is shown in (b). For the dominant low frequency QPO, the following three quantities are plotted: (c) central QPO frequency; (d) amplitude (% rms); and (e) quality factor Q . The gaps in these plots

correspond to the non-detection of QPOs, which occurred primarily in the TD state. For reference, the Fe K-line and accretion-disk fluxes (f & g , respectively), are shown replotted from Figure 4.

Fig. 6.— Fe, disk and power-law fluxes and the QPO amplitude during the first 94 days of the outburst. These blow-up plots are identical to those shown in Figures 4e-g and Figure 5d, respectively, but here the states are identified by their plotting symbols (see key in Fig. 3). For the error estimates, which are not shown and are generally smaller than the plotting symbols, see Figures 4 & 5 and Tables A2 & A3.

Fig. 7.— Sample energy spectra identified by day number and typed by X-ray state. For each panel, the solid line, which is largely obscured by the data, is the best-fit model spectrum. The power-law, disk and Fe-line components are shown as dotted, dashed and dot-dashed lines, respectively. Day 18.6: spectrum from the rising phase dominated by the power-law; note break near 15 keV. Day 41.8: an interlude of thermal behavior during the flaring state. Day 46.9: spectrum of the strongest power-law flare; the power-law is dominant, but note the hot ($kT = 1.63$ keV) and luminous disk component. Day 57.7: one of six observations that show an absence of a thermal disk component. Day 110.3: representative spectrum during the first 12 twelve of thermal-state decay of the disk (days 102–187); note the faint, steep power-law component and how this typical thermal-state spectrum differs from those shown here for days 41.8 and 193.5. Day 193.5: representative spectrum during the final 5.5 weeks of thermal-state decay of the disk (days 172–211); note the hard, prominent power-law component during this period. Day 228.0: the final spectrum with $\Gamma = 2.14 \pm 0.02$ (Table A2) is essentially a hard-state spectrum but has been classified as Hard:SPL because its photon index is marginally too soft (Table A2).

Fig. 8.— Bolometric luminosities versus disk temperature for observations made in the thermal state. For H1743–322 the eight data points at the highest temperatures ($T_{\text{in}} \approx 1.2$ keV) were made early in the outburst cycle, near day 42, when the flaring temporarily subsided; note that most of these thermal-state data fall well below an extrapolation of the lower-temperature data. For reference, the dotted line indicates the slope for $L_{\text{disk}} \propto T_{\text{in}}^4$. The luminosities are isotropic average values for our adopted distances (§4.3) and assume $i = 70^\circ$ for both sources.

Fig. 9.— QPO frequency versus disk luminosity for H1743–322 and XTE J1550–56. For the key to the plotting symbols, see Figure 3. The collection of data points that comprise the “strongly correlated data” discussed in the text are marked by the small black dots; each dot is plotted 0.6 Hz below the data point in question. The luminosities are for the 2–20 keV band and are isotropic averages (see Fig. 8 for details). The error bars, which are

smaller than or comparable to the size of the plotting symbols, are omitted for the sake of clarity. One extreme data point for XTE J1550–564 for MJD51239.08 is omitted to maintain reasonable scales on the axes. (The flux errors for XTE J1550–564 were overestimated by Sobczak et al. 2000b by a factor of ≈ 5 .)

Fig. 10.— A blowup of Figure 9 showing just the strongly correlated data that are defined in the text. For the key to the plotting symbols, see Figure 3. Note that some hard- and intermediate-state data plotted at low disk luminosity in Figure 9, which were obtained near the end of the outburst cycle, are not included here.

Fig. 11.— QPO frequency versus the low-energy (3–15 keV) photon index for H1743–322 and XTE J1550–564. For the key to the plotting symbols, see Figures 3 & 9.

Fig. 12.— QPO frequency versus the continuum power density (0.1–10 Hz) for H1743–322 and XTE J1550–564. For definitions of the plotting symbols, see Figures 3 & 9.

Fig. 13.— QPO frequency versus QPO amplitude. The exceptional point located near zero frequency with low amplitude corresponds to the first observation of H1743–322, which was made on day 7.8 (Table A3). For the key to the plotting symbols, see Figures 3 & 9.

Fig. 14.— Detailed look at the strongest power-law flares observed for H1743–322 (left panel) and XTE J1550–564 (right panel). From top to bottom are plotted the power-law flux, disk temperature, inner disk radius, disk flux, and Fe K line flux (the fluxes are in units of $\text{ergs cm}^{-2} \text{ s}^{-1}$). To facilitate the comparison, the fluxes and radii for XTE J1550–564 have been scaled down by the factors $(5.5/10)^2$ and $(5.5/10)$, respectively, from the values given by Sobczak et al. (2000b) to correct for the lesser estimated distance of this source (§4.3).

Fig. 15.— VLA radio data. The low-frequency data (b) extend over the entire outburst cycle (see Table A4), and the high-frequency data (c) are limited to the first 40 days (see Table A5). The 2–20 keV power-law flux is shown in (d) for comparison. The X-ray state is indicated in panel a (see Fig. 3 for key to plotting symbols).

Fig. 16.— Superposition of radio and X-ray data are shown for the first 120 days of the outburst cycle. The same 8.460 GHz radio data are arbitrarily scaled and plotted (red triangles) in each of the three panels. The X-ray data shown are (b) the 2–20 keV power-law flux, (c) the *difference* in the power-law indices, and the Fe K line flux (see Figs. 4g, 4d & 4e, respectively). The radio spectral index α ($S_\nu \propto \nu^\alpha$), which is based on the 4.860 GHz and 8.460 GHz data is shown in panel e, and the X-ray state is indicated in panel a (see Fig. 3 for key to plotting symbols).

Fig. 17.— (a) Quiescent i' -band image obtained on 2006 June 23 UT. The image is a median

of five 300 s exposure obtained under $0.43''$ seeing. (b) I -band image obtained near the start of the 2003 outburst on day 15.4 (2003 April 5.4 UT). Tick marks point the location of the optical counterpart. The exposure time was 330 s and the seeing was $0.48''$. North is up and East is left with a $20''$ field of view.

Fig. 18.— K -band images. (a) Quiescent image obtained on 2006 May 7.4 UT; the seeing is $0.43''$ and the exposure time is 375 s. Tick marks indicate the location of the near-infrared counterpart. (b) Image obtained near the end of the outburst on day 175.1 (2005 September 12.1 UT); the exposure time was 150 s and the seeing was $0.55''$. The error ellipse marks the position of the radio counterpart to H1743–322. North is up and East is left.

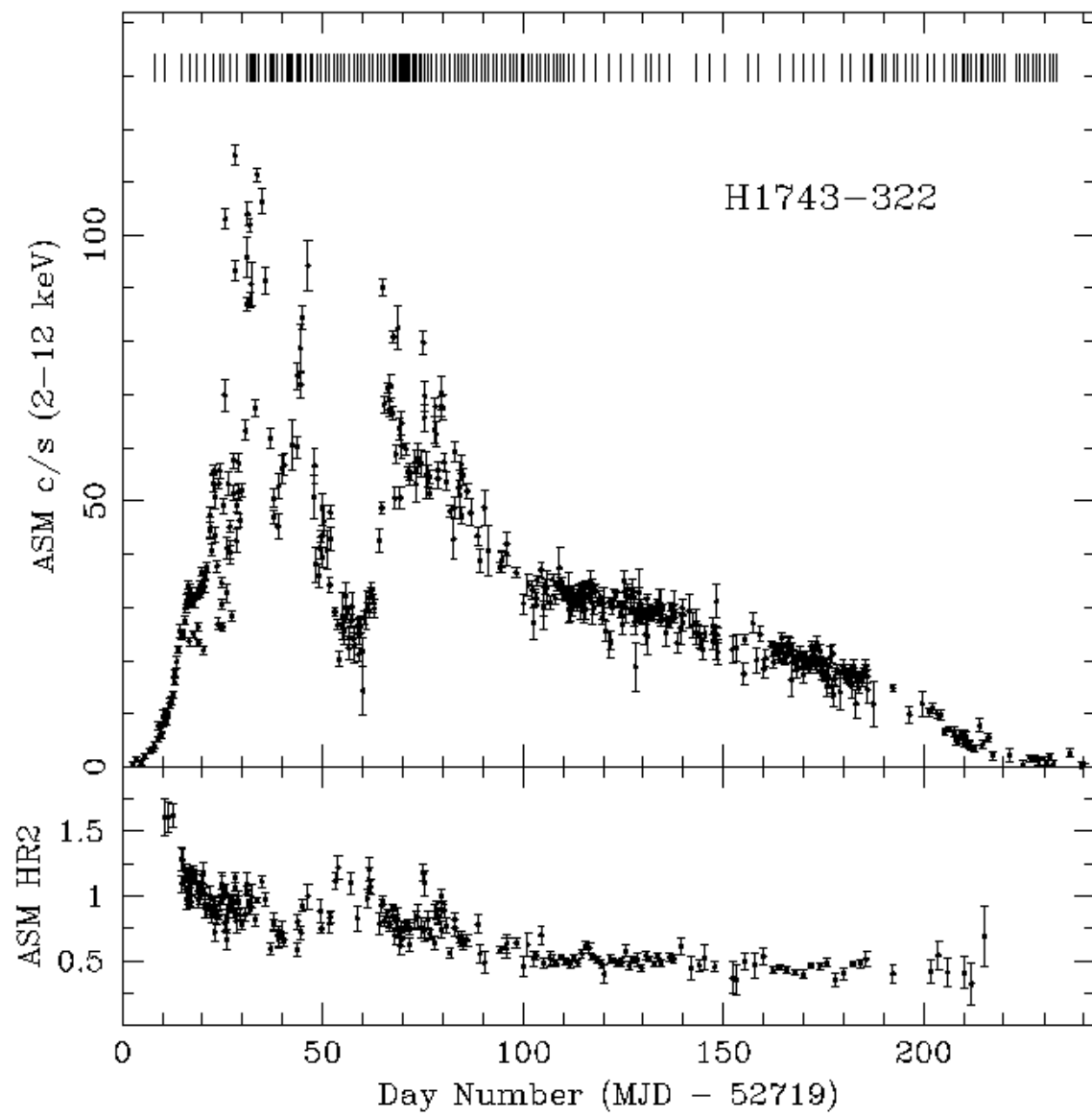


Fig. 1.—

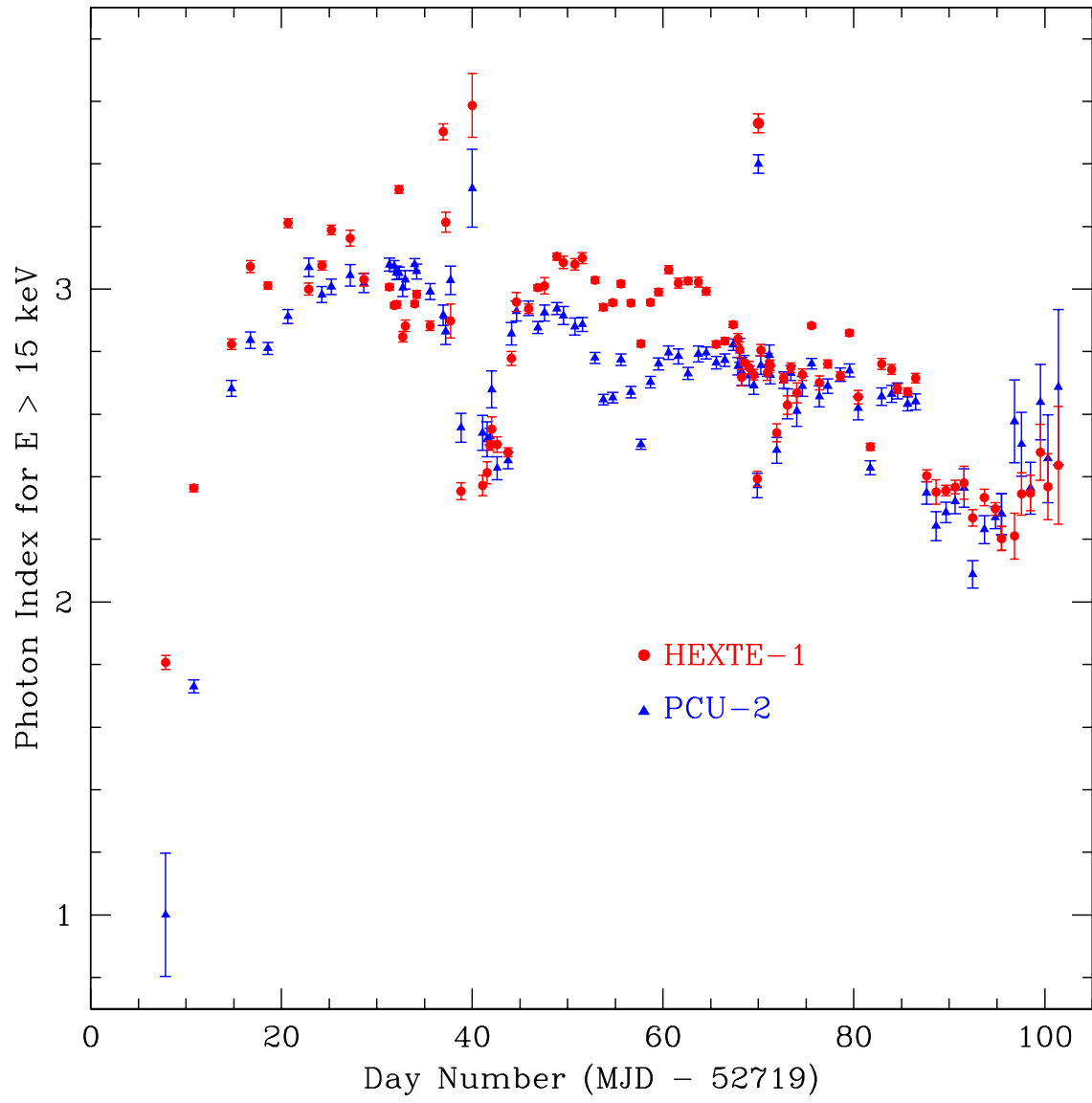


Fig. 2.—

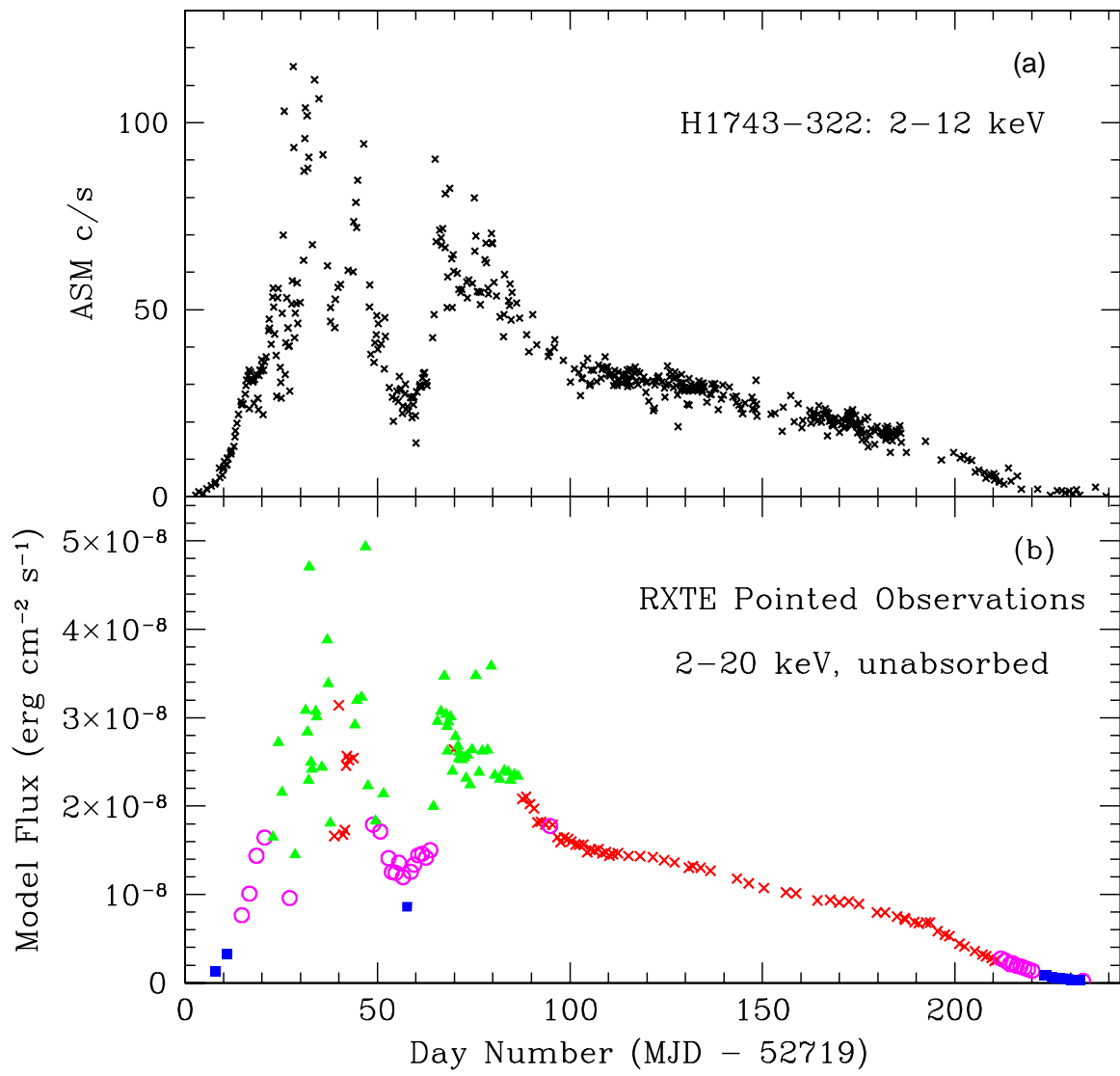


Fig. 3.—

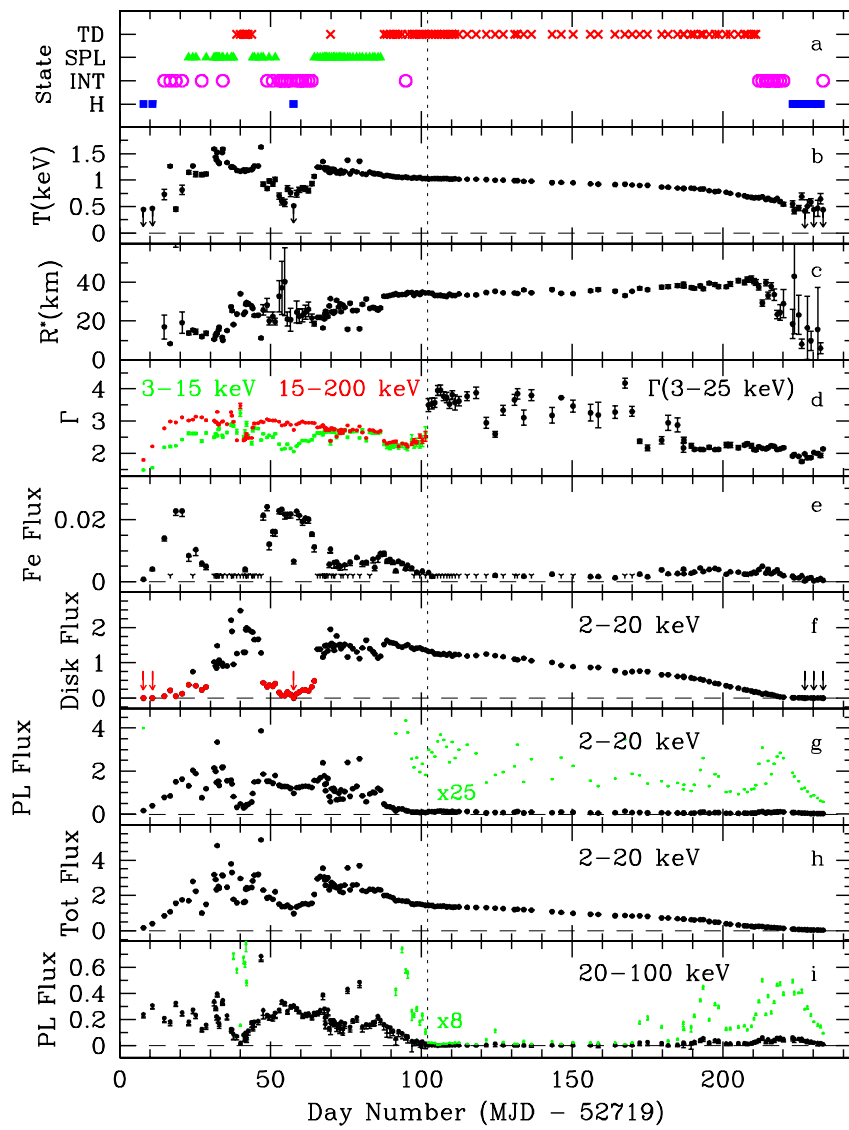


Fig. 4.—

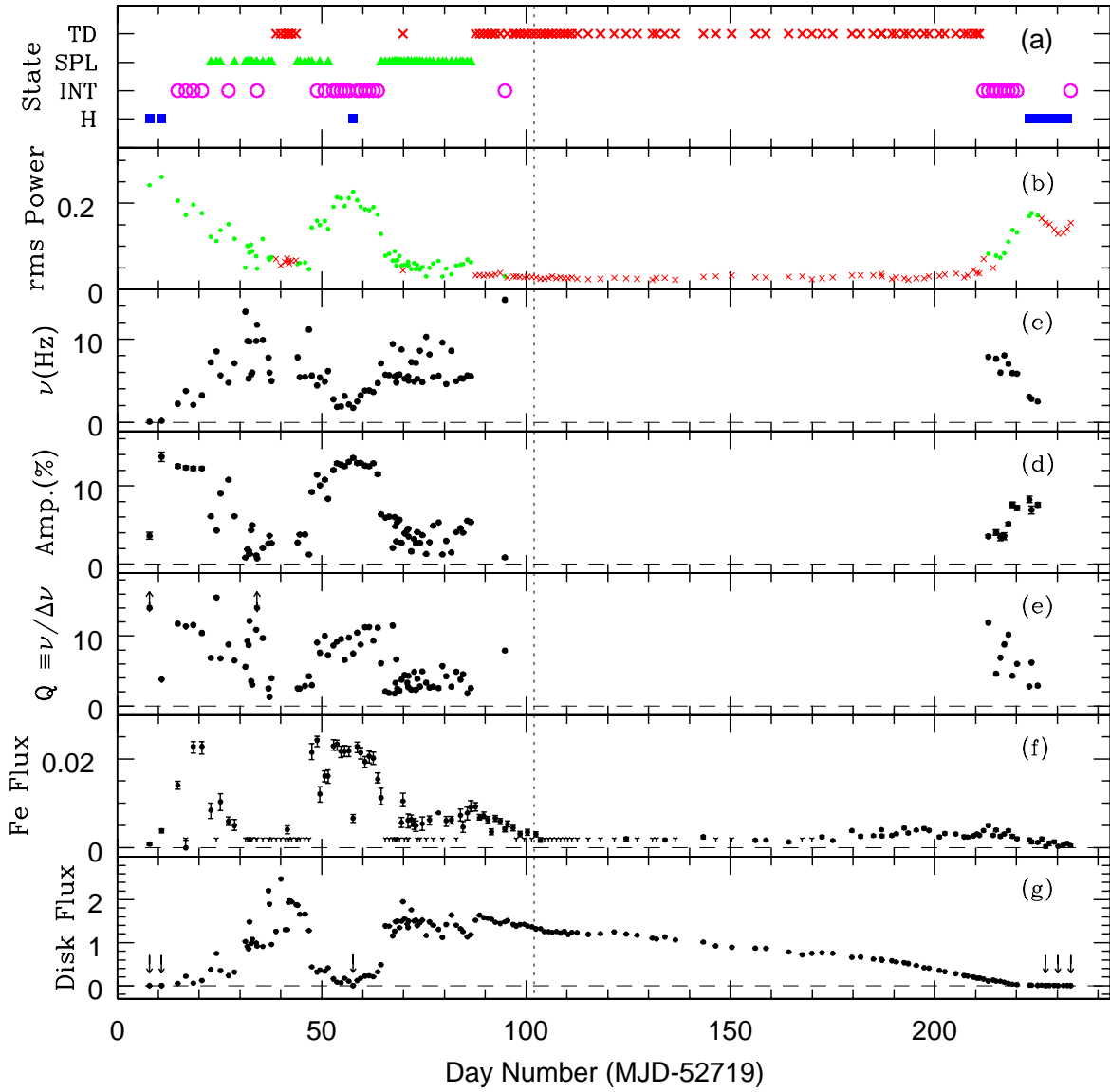


Fig. 5.—

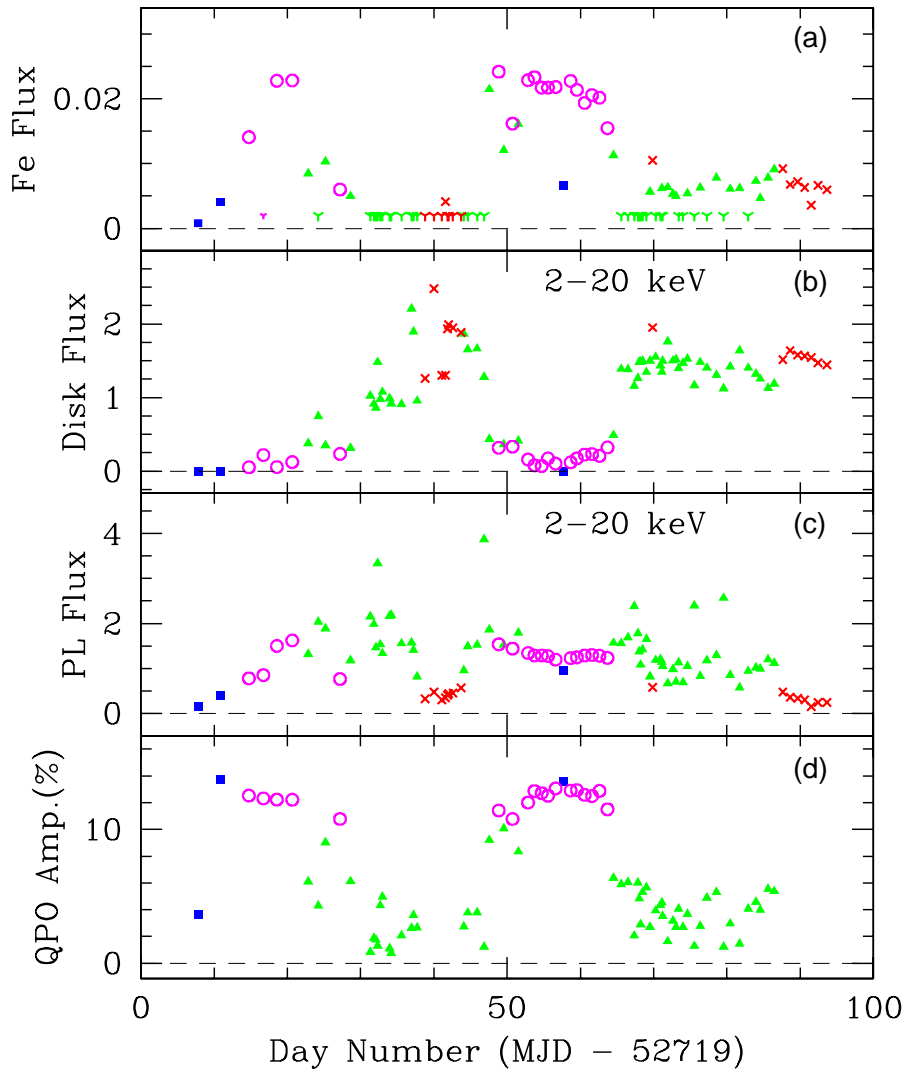


Fig. 6.—

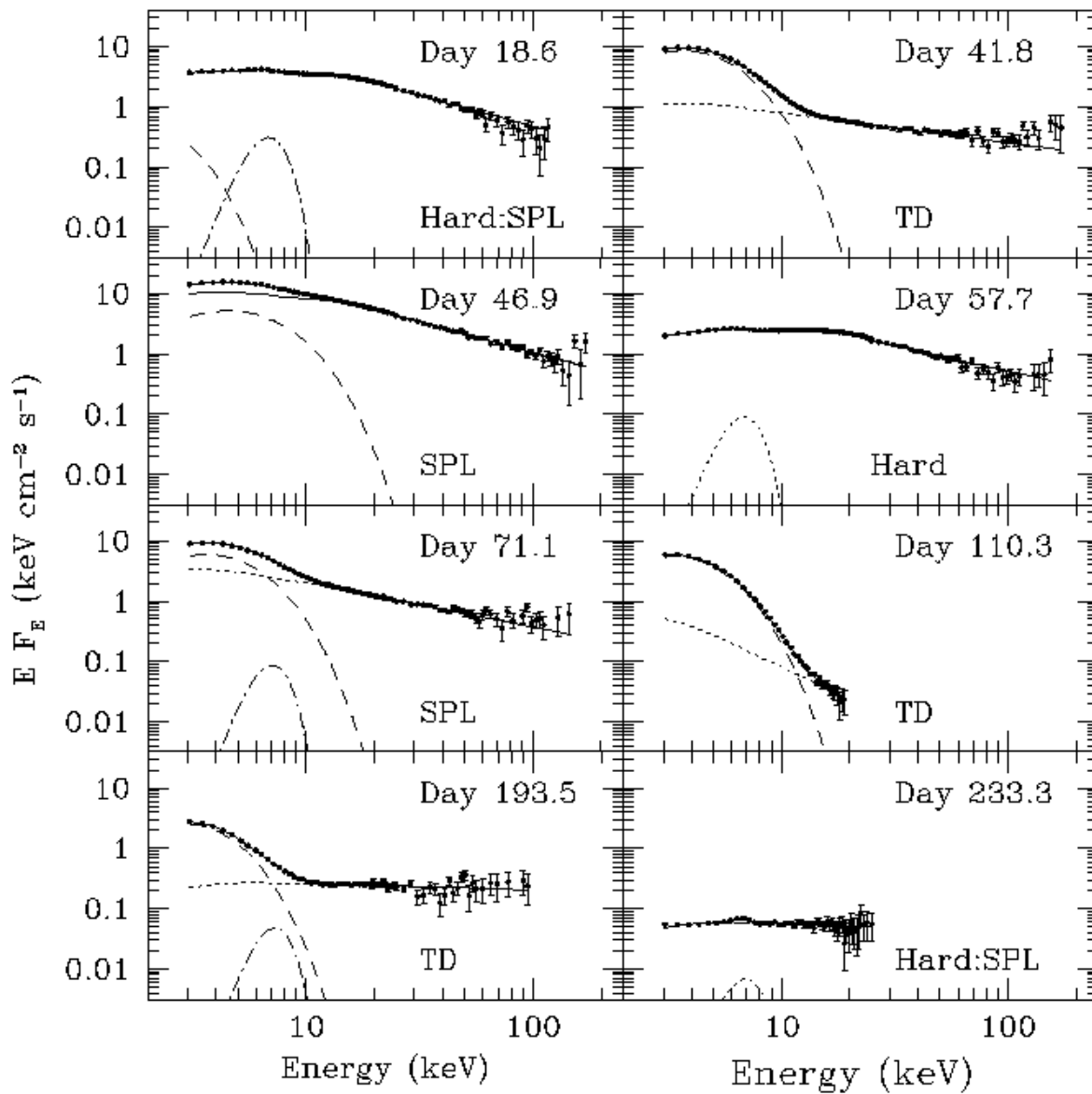


Fig. 7.—

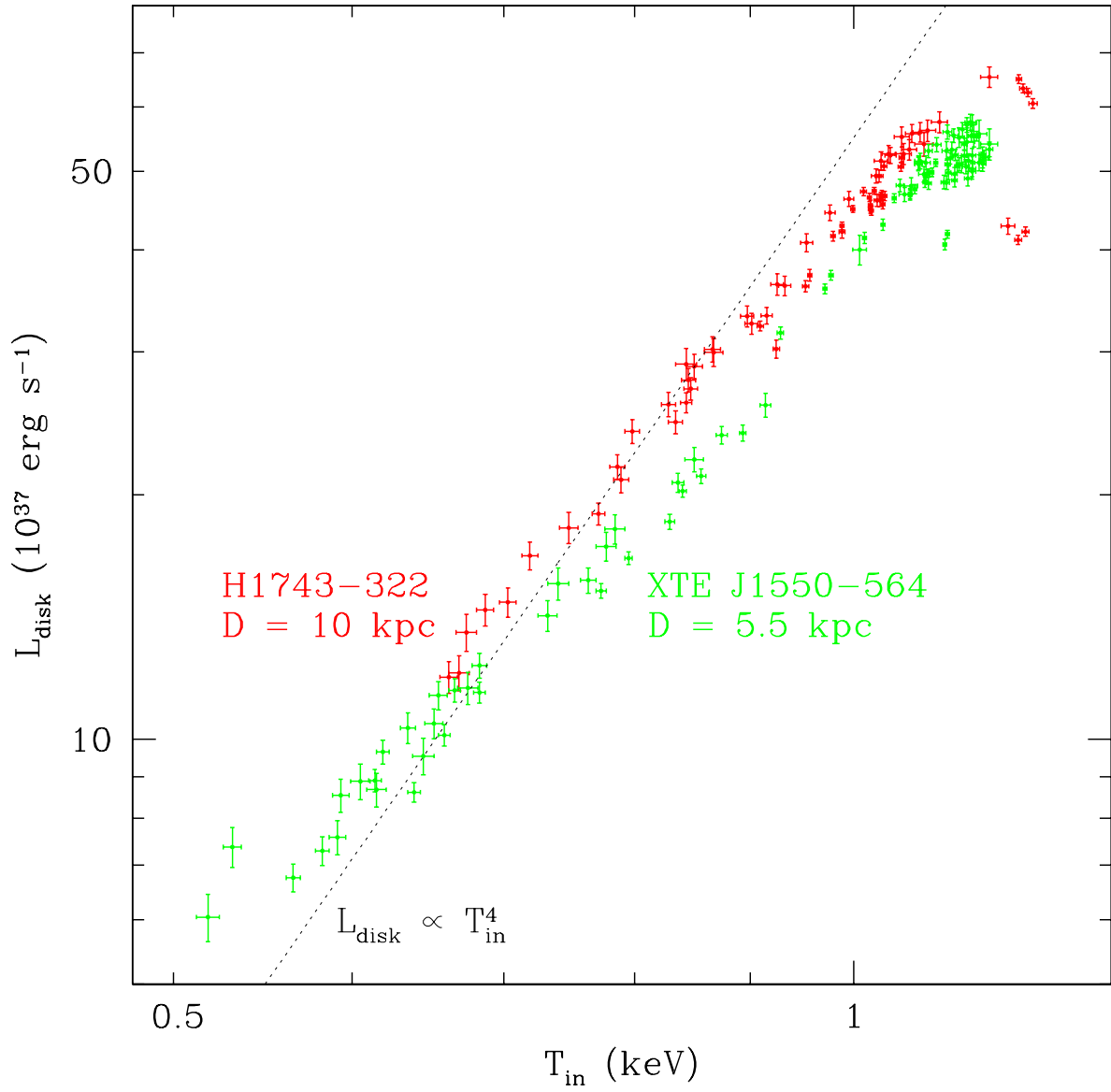


Fig. 8.—

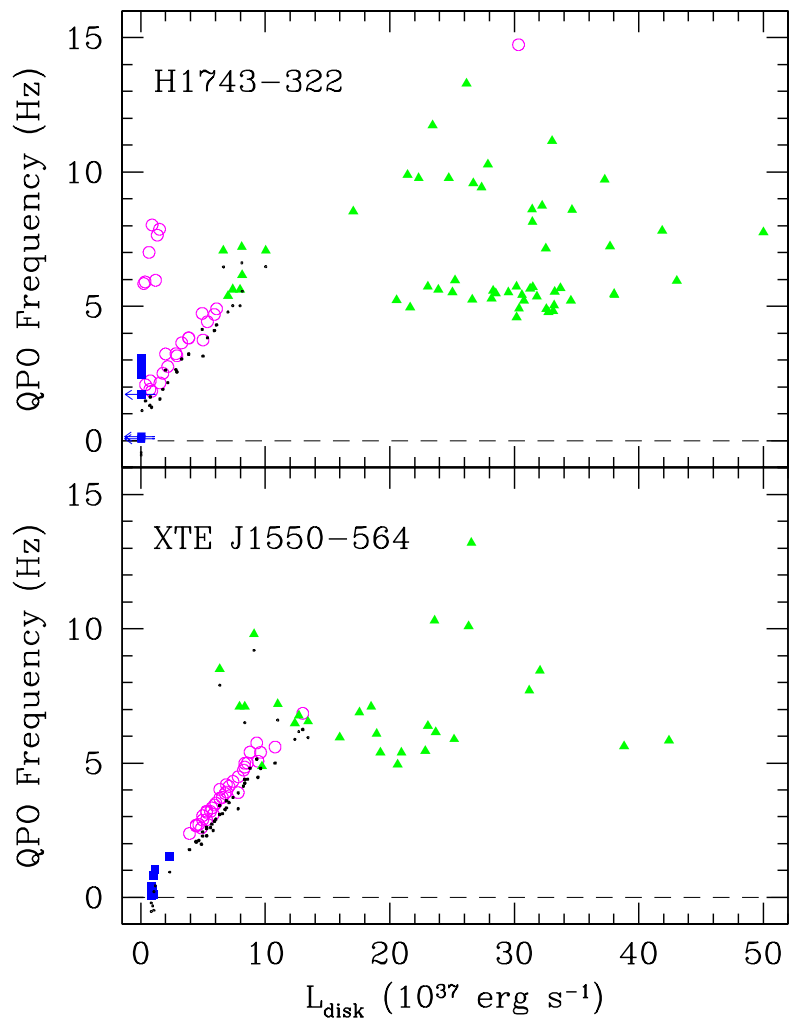


Fig. 9.—

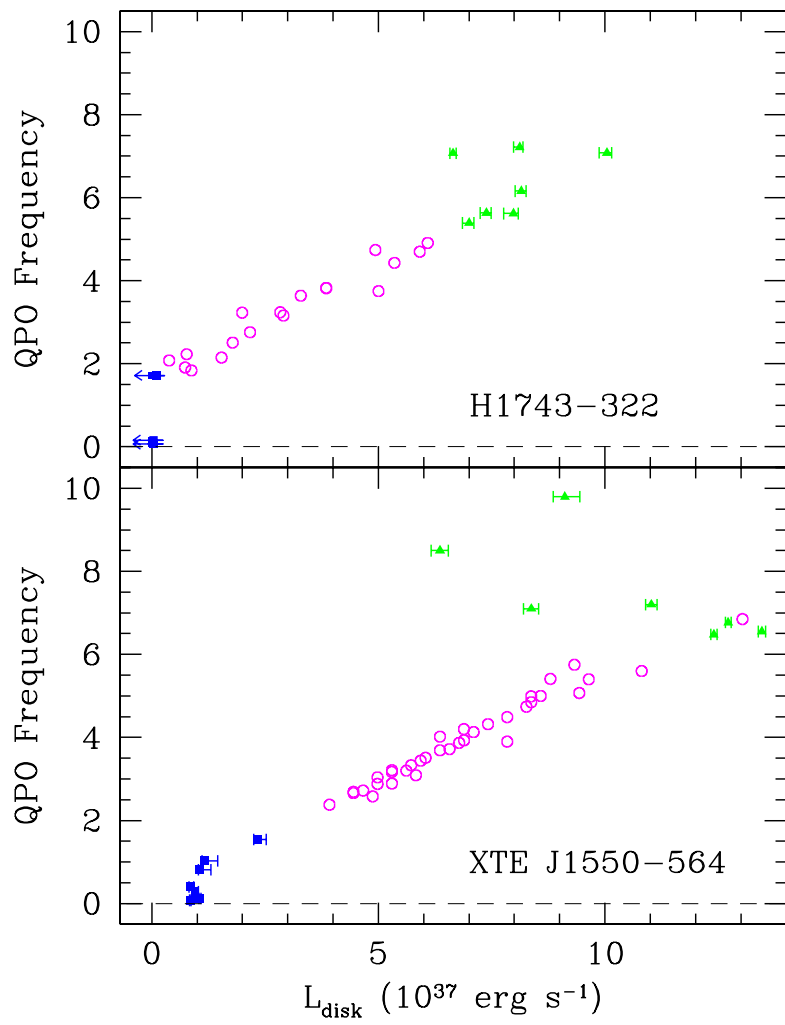


Fig. 10.—

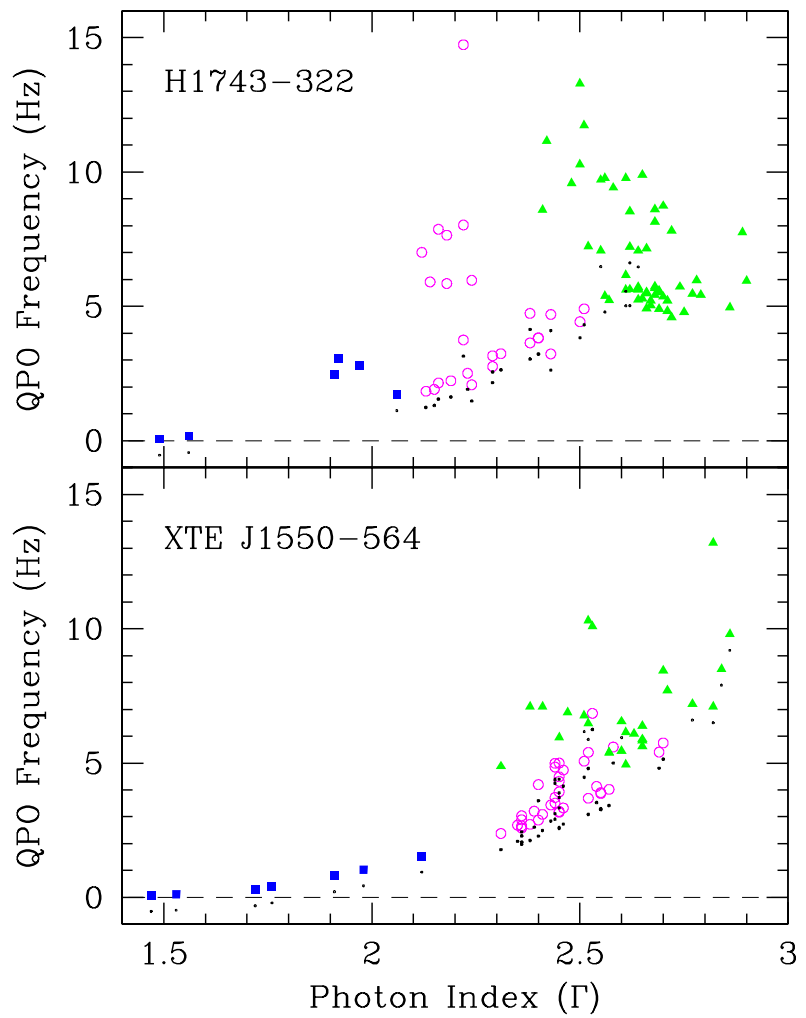


Fig. 11.—

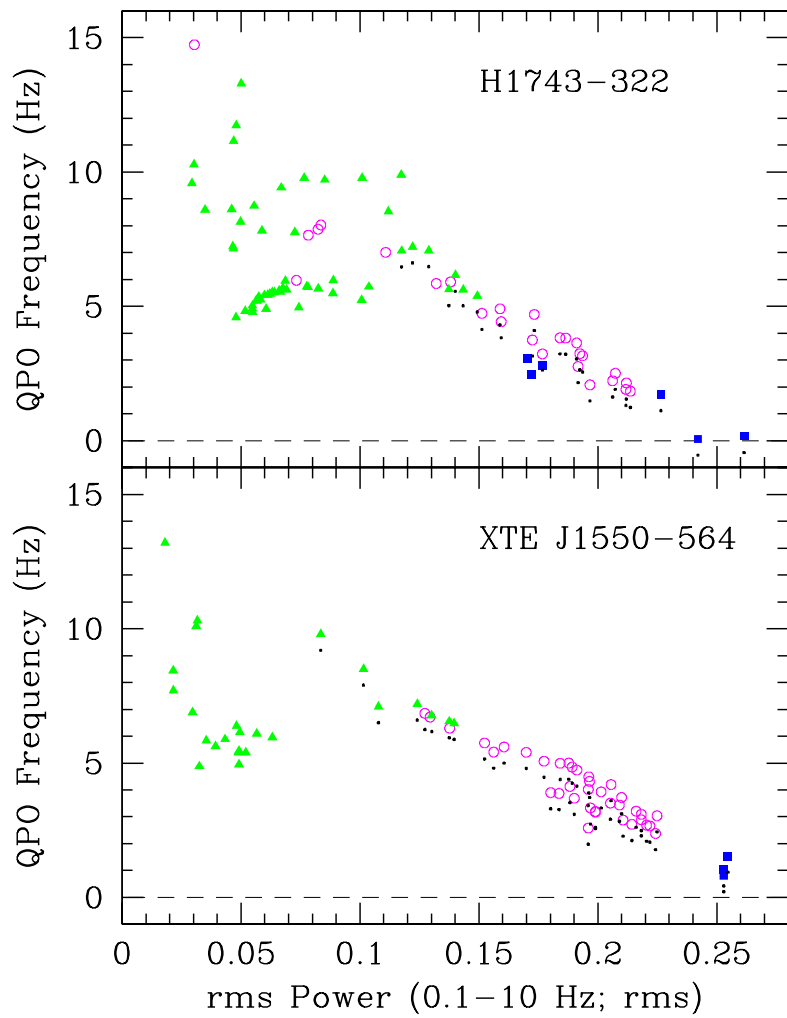


Fig. 12.—

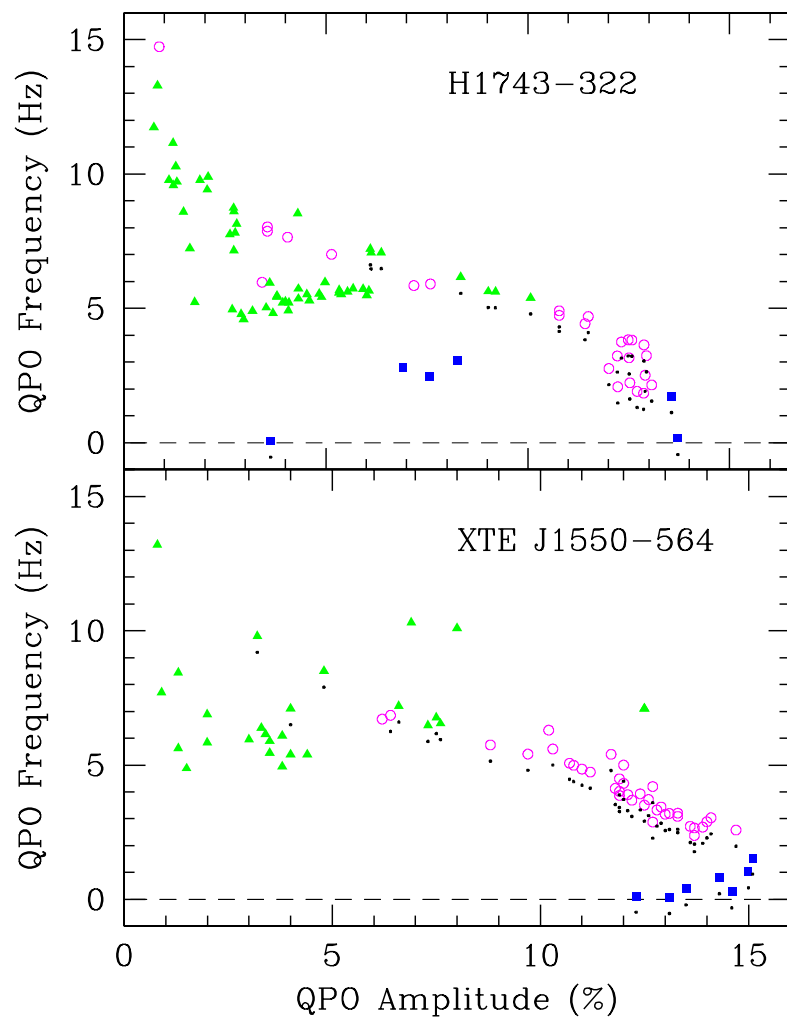


Fig. 13.—

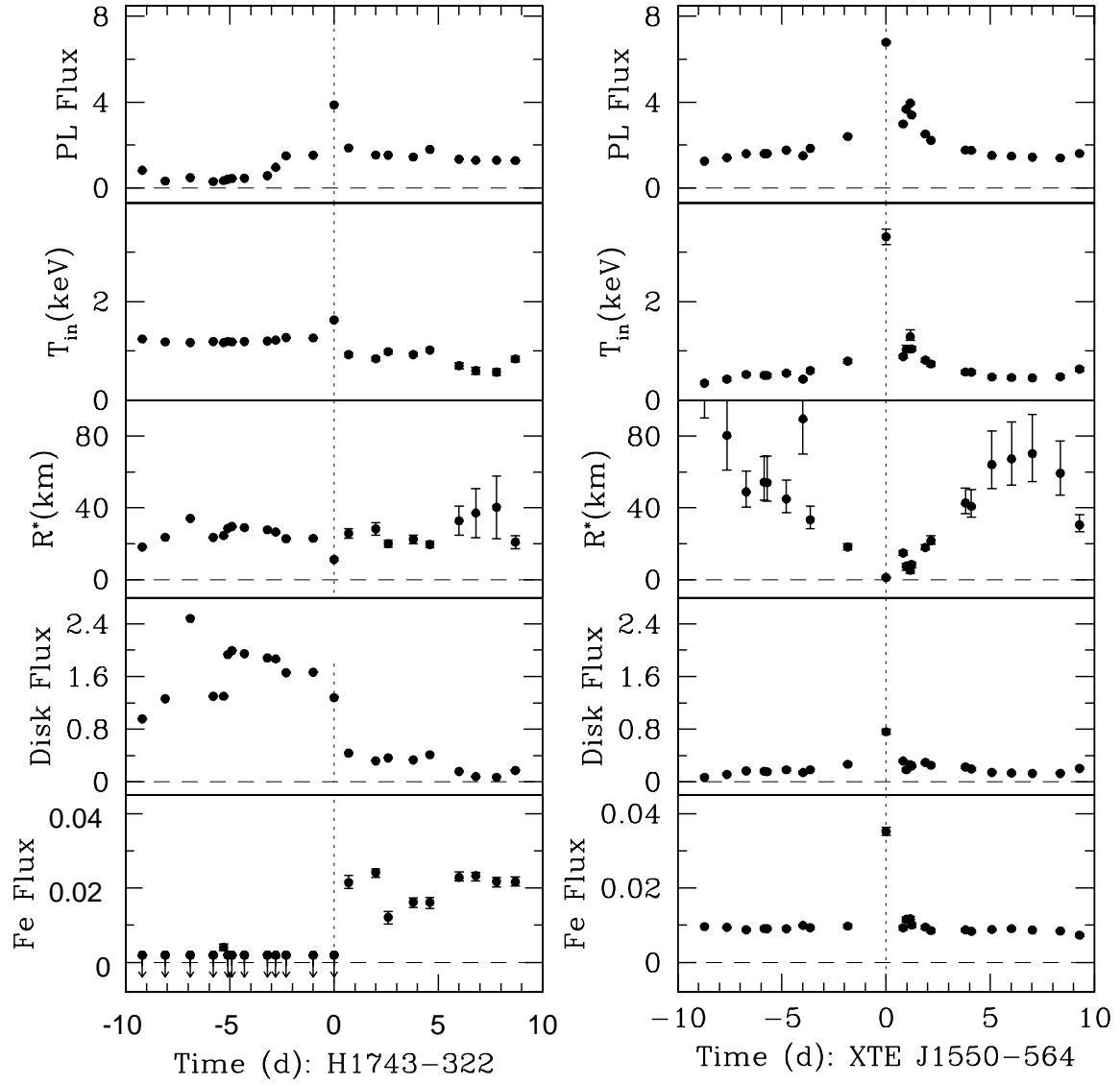


Fig. 14.—

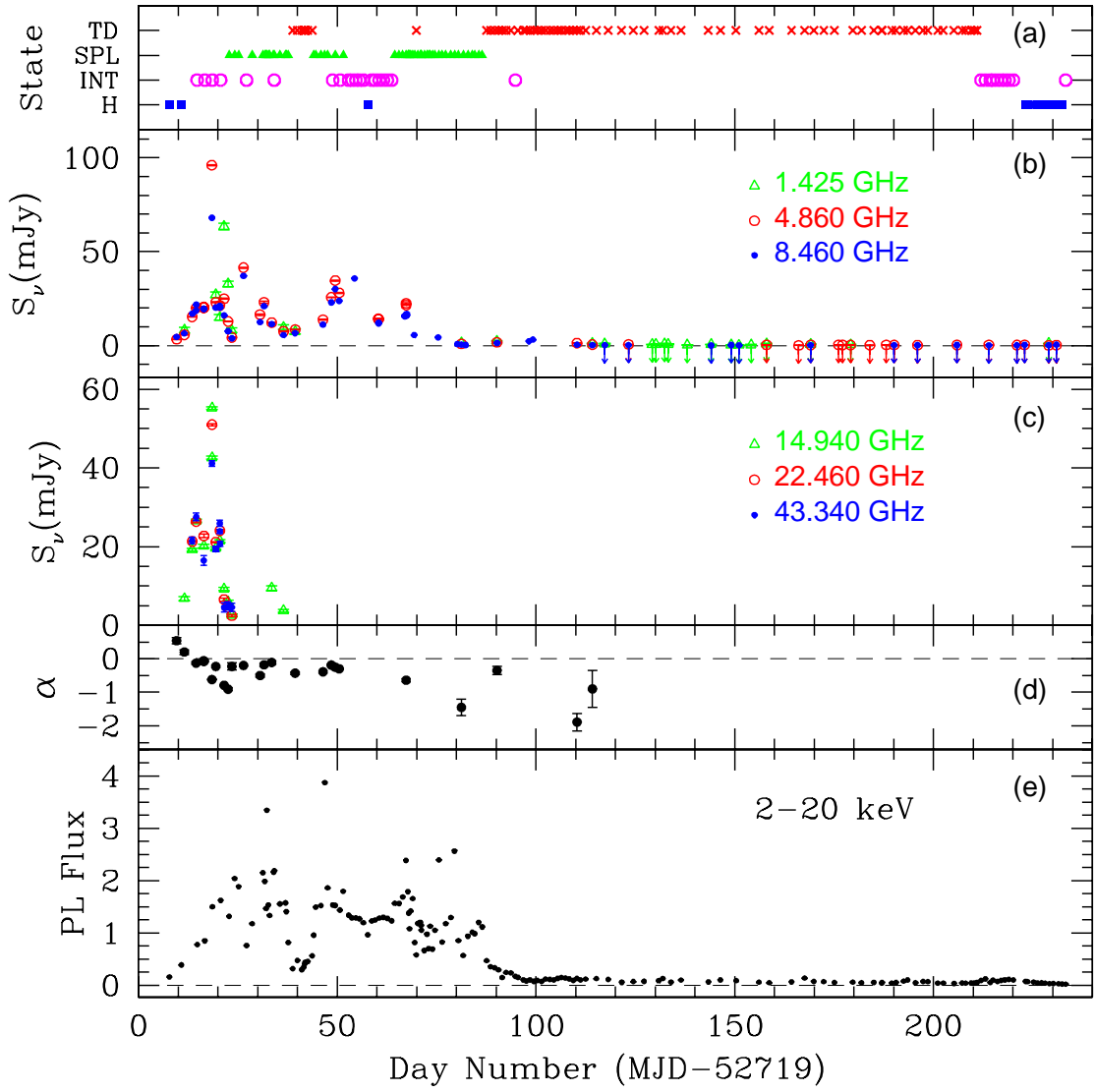


Fig. 15.—

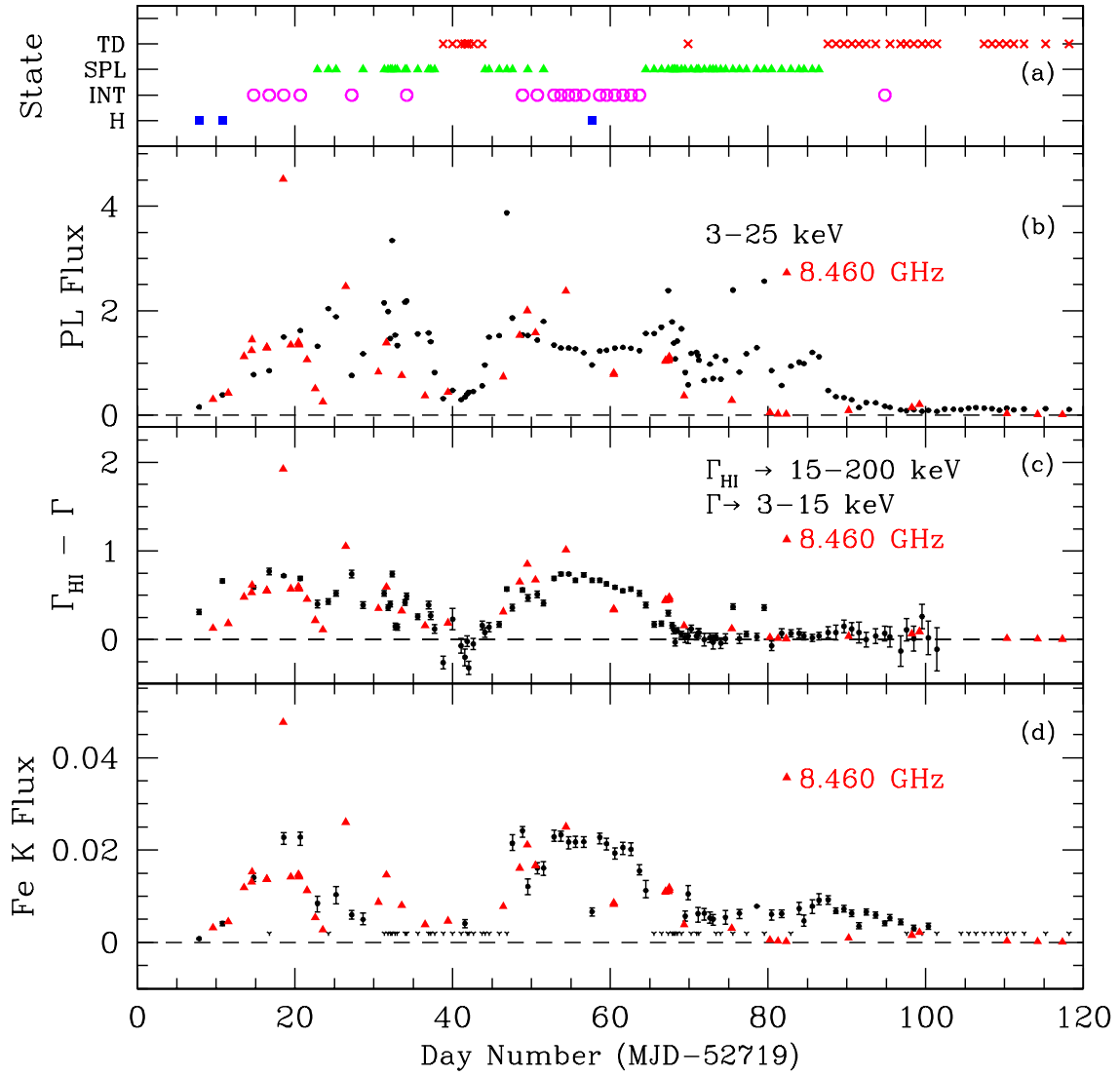


Fig. 16.—

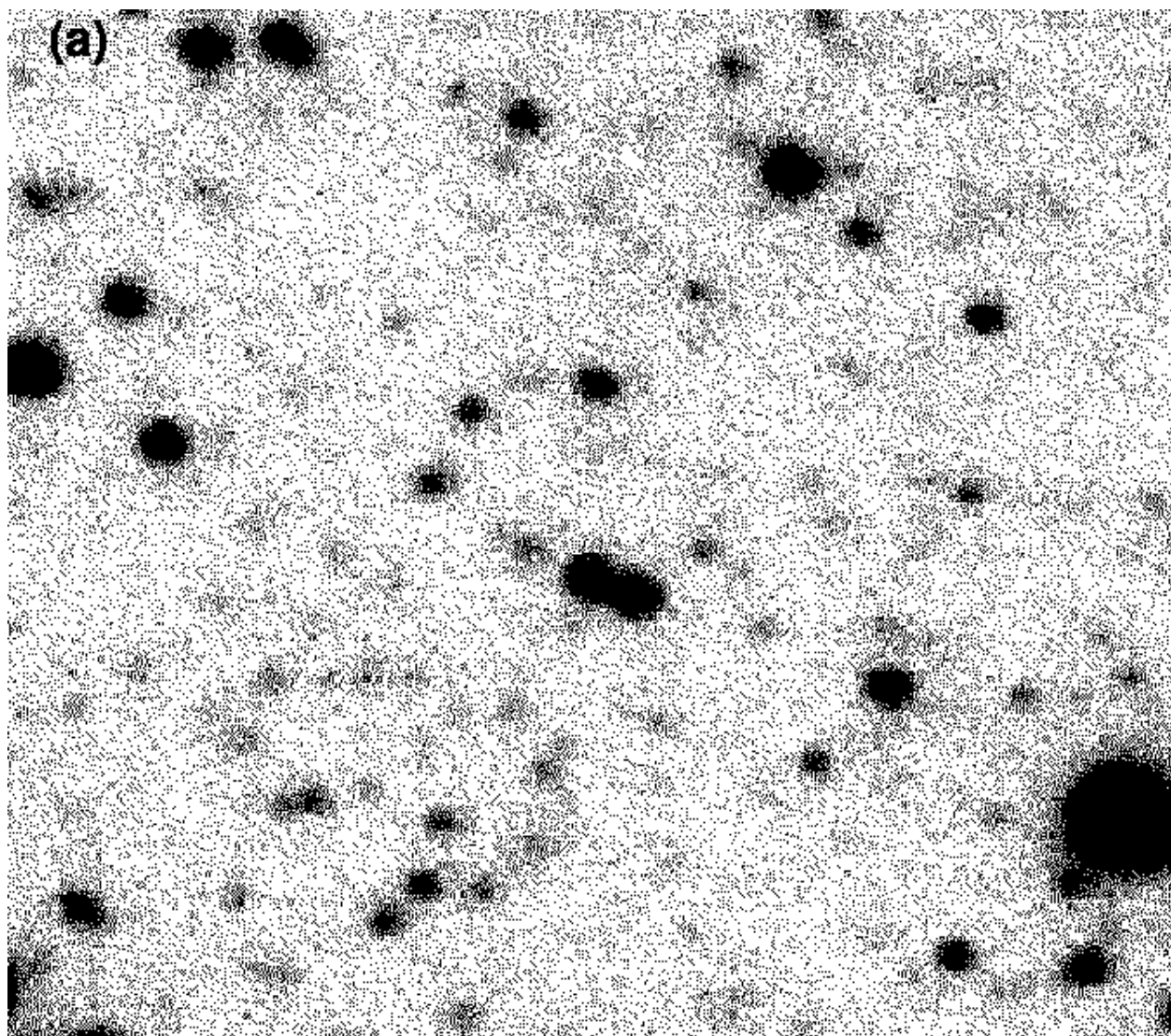


Fig. 17.—

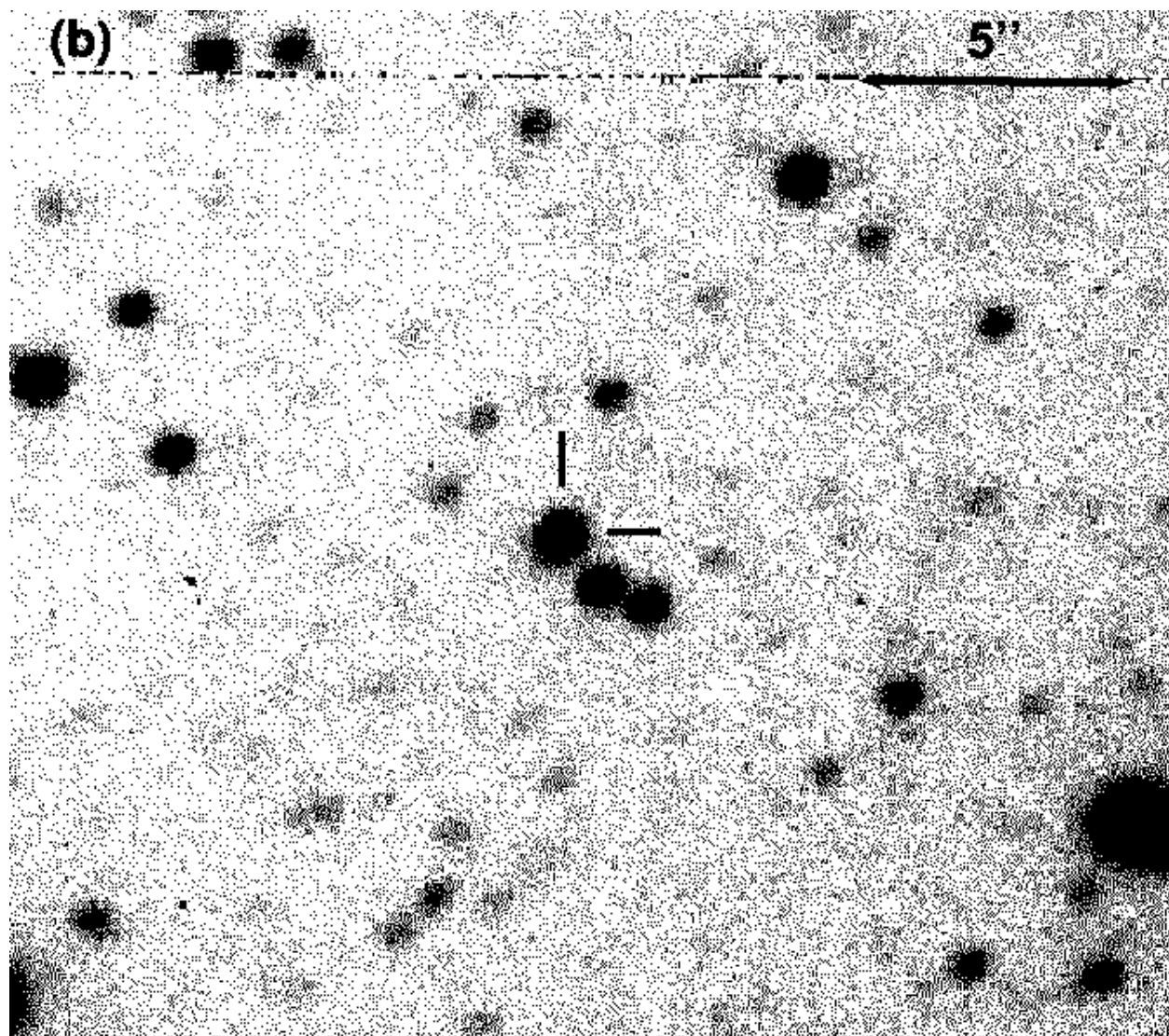


Fig. 17.—

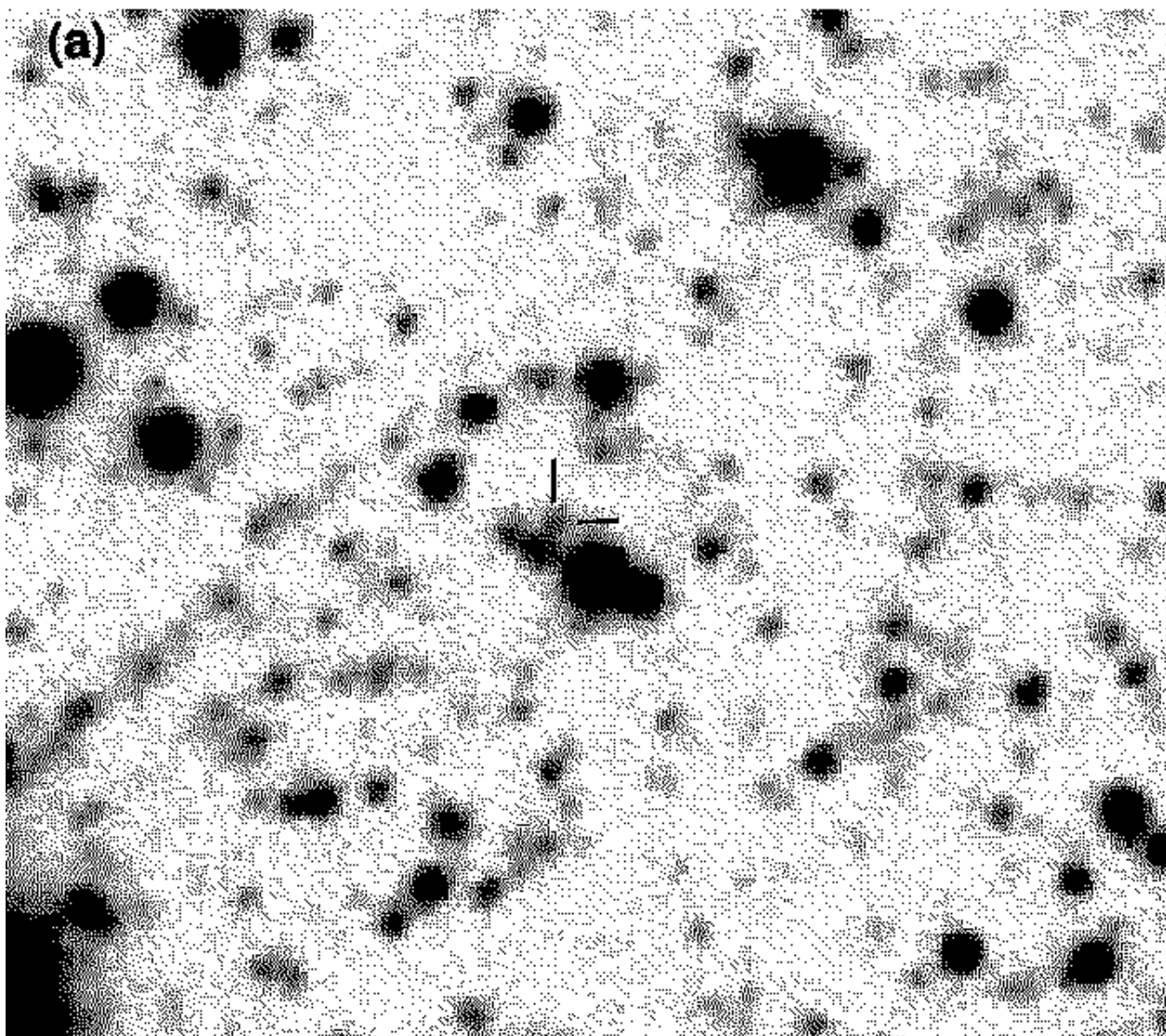


Fig. 18.—

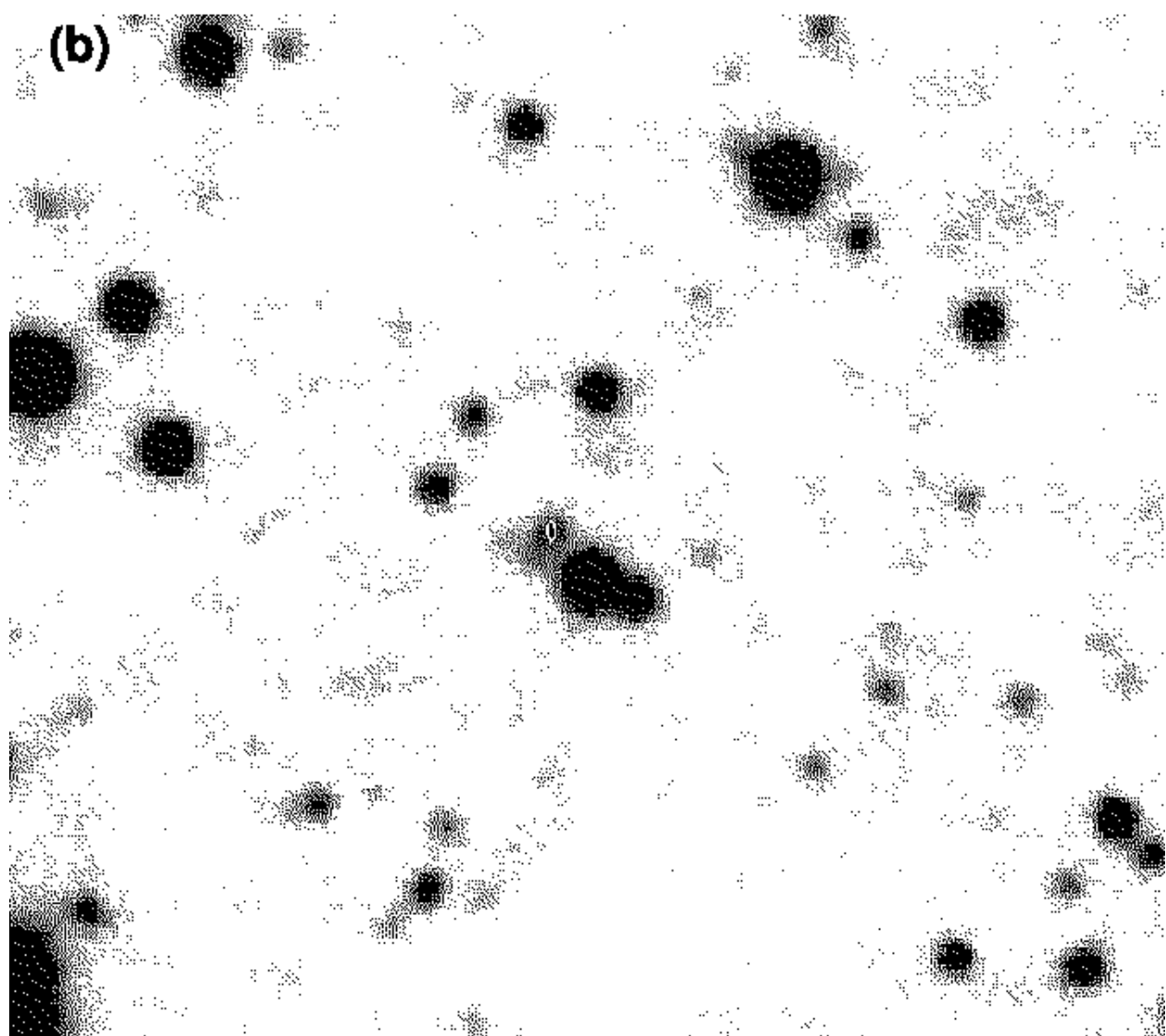


Fig. 18.—